Abschlussarbeit im Masterstudiengang Physik

$\mathrm{d}E/\mathrm{d}x$ Resolution Studies of a Pre-Production Read-Out Chamber with GEMs for the ALICE TPC

Untersuchung der $\mathrm{d}E/\mathrm{d}x$ Auflösung einer Auslesekammer mit GEMs aus der Vorproduktion für die ALICE TPC

Thomas Klemenz

8. März 2019

Erstgutachter (Themensteller): Prof. L. Fabbietti
Zweitgutachter: Prof. B. Märkisch
Betreuer: A. Mathis

Abstract

A large Time Projection Chamber (TPC) is the main device for tracking and particle identification in the ALICE detector at CERN. After the second long shutdown of the LHC between 2019-2020 the interaction rate of the LHC will be increased to 50 kHz in Pb–Pb collisions. Currently, the ALICE TPC is operated with gated Multi-Wire Proportional Chambers limiting the readout rate to about 3.5 kHz. For the operation in the LHC RUN 3, however, a event pile-up of 5 events on average is expected in the active volume of the TPC demanding for continuous readout in order to fully exploit the LHC capabilities. This implies a major upgrade to the readout chambers, which are replaced by Gas Electron Multiplier (GEM)-based readout chambers. To keep distortions from back drifting ions in the TPC at a tolerable level, an ion back flow below 1 % is required. After a thorough R&D phase, the solution for the upgrade has been found to be a quadruple stack of GEMs. In addition, the computing system and the corresponding software framework need to be upgraded. The new system, O^2, can pre-process the data online and reduce the amount of data that needs to be stored for post-processing significantly. O^2 also incorporates the simulation and analysis framework.

To test the performance of the GEM-based readout chambers and the new readout scheme an Inner Readout Chamber from the pre-production phase was equipped with the new front-end cards and irradiated with a secondary beam of pions and electrons at the CERN Proton Synchrotron. In the course of this work, which is the first analysis done with O^2, the gain uniformity of the GEM stack, the resolution of the mean energy loss $\langle \mathrm{d}E/\mathrm{d}x \rangle$ and the separation power of the two particle species are extracted from the data. The obtained energy resolutions at a beam momentum of 1 GeV c^{-1} are 11.9 % and 10.7 % for pions and electrons, respectively, resulting in a separation power of $3.65\,\sigma$. Compared to a previous test beam campaign the performance is worse. The main difference between the two test beam campaigns is the reduction of the sampling rate from 20 to 5 MHz to reduce the amount of data during continuous operation. In combination with a drift length of ≈ 5 cm on average this leads to a significantly decreased energy resolution. To verify this hypothesis, a toy Monte Carlo simulation is conducted, which is consistent with the observations in the measurements. Finally, the test beam data is compared to simulations in order to tune and validate the implemented signal creation process.

Contents

1 Introduction **1**
1.1 The LHC . . . 1
1.2 The ALICE detector . . . 2
1.3 Challenges and opportunities in RUN 3 . . . 5

2 The ALICE TPC **7**
2.1 Time Projection Chambers . . . 7
2.2 Particle identification . . . 8
2.3 Drift and diffusion . . . 12
2.4 Amplification . . . 13
2.5 Ion back flow . . . 14
2.6 Overview on the ALICE TPC . . . 15
2.7 Operation with MWPCs . . . 16
2.7.1 Working principle . . . 16
2.7.2 Performance . . . 18

3 The TPC Upgrade **21**
3.1 Gas Electron Multipliers . . . 21
3.1.1 Electron amplification . . . 21
3.1.2 Characterization . . . 24
3.2 Technical implementation . . . 26
3.2.1 GEM production . . . 33
3.2.2 Read Out Chamber assembly . . . 34

4 Test beam at the CERN Proton Synchrotron **35**
4.1 Experimental setup . . . 37
4.2 Data acquisition . . . 40
4.3 Track reconstruction . . . 42

5 TPC simulation in O^2 **43**

6 Results **47**
6.1 Test beam data analysis . . . 47
6.1.1 Gain uniformity studies . . . 51
6.1.2 Separation power and $\mathrm{d}E/\mathrm{d}x$ resolution . . . 54
6.2 Study of the influence of the sampling frequency on the detector response . 58
6.3 Simulation benchmarking . . . 63

7 Summary and Conclusion **67**

Bibliography **69**

Danksagung **75**

1 Introduction

1.1 The LHC

The Large Hadron Collider (LHC) [1] is the largest, most powerful particle collider to date. It consists of two beam pipes guiding the beams in opposite directions with a circumference of 27 km. It is located at CERN near Geneva in Switzerland. The accelerator was built inside the tunnel that was employed for the Large Electron-Positron Collider (LEP) from 1984 to 1989 and lies between 45 m and 170 m below the surface. The four main experiments, ATLAS, ALICE, CMS, and LHCb, are located at the interaction points 1, 2, 5, and 8 as visible in Fig. 1.1.

The beams are guided by super-conducting magnets that are operated at $\sim$2 K to create magnetic fields above 8 T. Such low temperatures can only be reached with a liquid helium cooling system. In total 1232 dipole magnets, each 15 m long, are used to bend the beam and 392 quadrupole magnets, each 5 m to 7 m long, to focus the beam [2].

The LHC collides particles at an unprecedented center of mass energy ($\sqrt{s}$) of up to 13 TeV in three operation modes: pp, p–Pb and Pb–Pb. During a short period in 2018, also Xe–Xe collisions were conducted. While most of the time the LHC is operated with proton beams, usually one month per year either p–Pb or Pb–Pb collisions are performed. The first data were taken in RUN 1 in 2010 at $\sqrt{s}$ =7 TeV. This run lasted until early 2013 when the first long shutdown took place to upgrade the LHC in order to increase the collision energy. RUN 2 started with $\sqrt{s}$ =13 TeV in June 2015 and was concluded in the end of 2018. In 2019, the second long shutdown started, featuring major upgrades to the LHC to increase its luminosity. Furthermore, the experiments are upgraded to conform with the performance of the upgraded LHC.

The unprecedented center of mass energy provided by the LHC allowed for the first observation of the Higgs boson [3, 4] and thus provided significant input to the verification of the Standard Model. Additionally, searches for supersymmetric particles are conducted [5], and in heavy-ion reactions the resulting hot and dense phase of strongly interacting matter is studied in detail [6]. In particular with the upcoming upgrades, going into full effect in 2026 [7], when the LHC will be significantly upgraded, the luminosity of the machine will be further increased by a factor of ten. These upgrades include the usage of 12 T superconducting magnets, sustaining and extending its discovery potential. Before that, however, already for the upcoming RUN 3 of the LHC (2021 - 2023) the interaction rates will be increased by a factor of 5 in Pb–Pb.

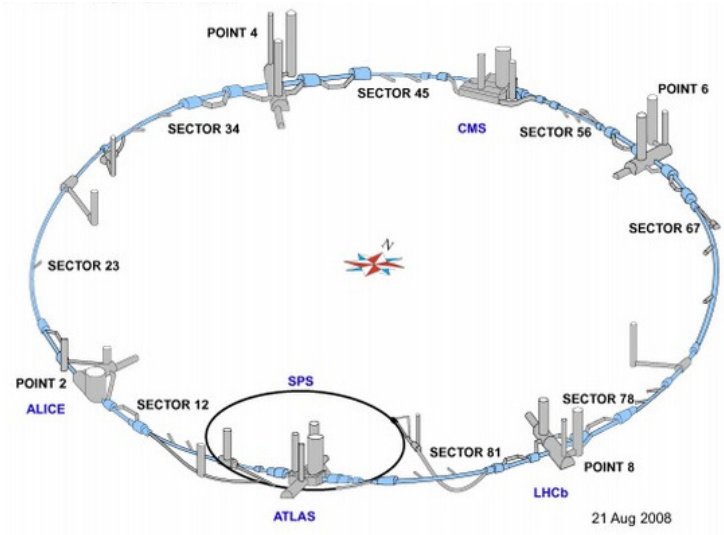

Figure 1.1: Schematic view of the LHC with the four major experiments [2].

1.2 The ALICE detector

ALICE (A Large Ion Collider Experiment) [8] is one of the four main detectors at the LHC. It is dedicated to heavy-ion physics focusing on studies of Quantum Chromodynamics (QCD), which describes the strong interaction in the Standard Model. In contrast to the other fundamental forces, the strong interaction has a running coupling constant α_s, which depends on the momentum transfer Q in a collision of quarks and/or gluons. Figure 1.2 shows α_s as a function of Q. For large momentum transfers, corresponding to small distances between the particles, the interaction strength decreases, leading to a very weak interaction between quarks and gluons. This phenomenon is called asymptotic freedom, because in this case the quarks can be assumed to be quasi-free. For low momentum transfers on the other hand, the interaction strength increases. As a result, quarks and gluons do not occur as isolated particles but they are confined in composite hadrons. However, at exteme values of temperature and/or energy density, a deconfined state of matter, the Quark-Gluon Plasma (QGP), has been predicted [9, 10].

The goal of the ALICE detector is to study the physics of strongly interacting matter in ultra-relativistic heavy-ion collisions, where the QGP is expected. To allow for a thorough study of this medium and the resulting final state products, hadrons, electrons, muons, and photons can be measured up to the highest multiplicities expected in Pb–Pb collisions. By studying proton-proton or proton-nucleus collisions, the energy density and the interaction volume can be varied. Data taking during proton-proton runs at the top LHC energy provides reference data for strong interaction studies and complementary data to the other LHC experiments.

The overall dimensions of the detector are $16 \times 16 \times 26\,\mathrm{m}^3$ with a total weight of $\approx 10.000\,\mathrm{t}$. The main part of the detector is the so-called central barrel for measuring hadrons, electrons and photons. The central barrel is embedded in a solenoid magnet that is reused from

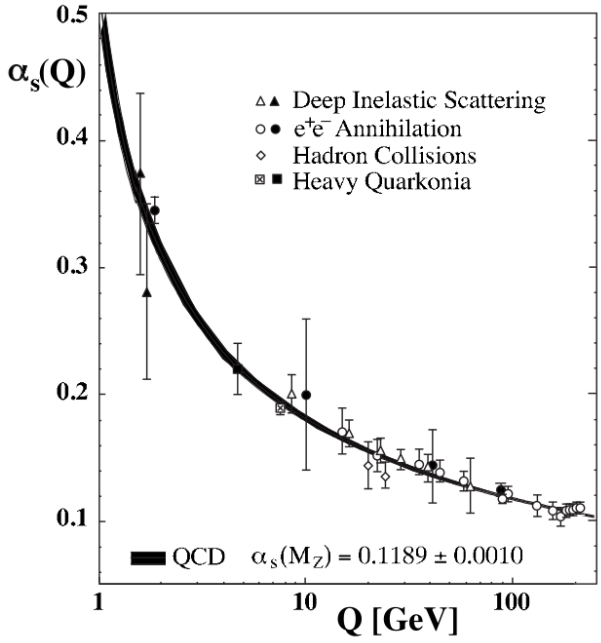

Figure 1.2: Running coupling constant α_s of the strong interaction as a function of the momentum transfer Q in a collision of quarks and/or gluons [11].

the L3 experiment at LEP [12]. A schematic view of the detector is shown in Fig. 1.3. From the inside out, the barrel contains the Inner Tracking System (ITS), which consists of high-resolution silicon pixel (SPD), drift (SDD), and strip (SSD) detectors, the Time Projection Chamber (TPC), three particle identification arrays of Time-Of-Flight (TOF), Ring Imaging Cherenkov (HMPID) and Transition Radiation (TRD) detectors, and two electromagnetic calorimeters (PHOS and EMCal). Except for PHOS, EMCal, and HMPID all central barrel detectors cover the full azimuth angle. The pseudo-rapidity interval covered by the detectors ranges from $|\eta| < 0.6$ to $|\eta| < 2$. A detailed overview on the detector coverage is given in [8]. Additionally, one arm of the spectrometer located at $-4 < \eta < -2.5$ is dedicated to study muons. The experiment is complemented by forward detectors (ZDC, PMD, FMD, T0, V0) for event characterization and triggering located at high $|\eta|$ regions. An array of scintillators (ACORDE) outside the L3 magnet is used to trigger on cosmic rays.

This variety of detector types provides different approaches for particle detection of different types of particles. The typical onion-structured layout of collider detectors is shown in Fig. 1.4. In the tracking system, charged particles can be detected via their energy loss in the detector. Together with a magnetic field, the sign of the charge and the particle momentum can be determined. Calorimeters measure the energy of particles and, depending on the type, determine whether they undergo electromagnetic or hadronic interaction. Except for muons and neutrinos, all particle species are typically stopped in the calorimeter while producing electromagnetic or hadronic showers. The energy of the incident particle is given by the sum of the energy contained in the particle shower. Photons, electrons, and positrons are stopped in the electromagnetic calorimeters. Hadrons, however, lose only a fraction

of their energy in the electromagnetic calorimeter and then are stopped in the hadronic calorimeter. Therefore, the two types of calorimeters can distinguish between leptons and hadrons. Finally, muons are easy to identify since they do not produce showers in the calorimeters and, therefore, are the only particles leaving a signature in the muon system.

The typical approach to conduct particle identification (PID) is done by mass determination [13]. In order to obtain the mass m one has to measure the momentum p and the velocity v of the particle since

$$m = \frac{p}{c\beta\gamma}, \tag{1.1}$$

where $\beta = v/c$ and $\gamma = 1/\sqrt{1-\beta^2}$. The velocity can be measured in different ways. The most commonly used and easiest ones are the TOF detector and the HMPID, which measures the Cherenkov radiation. In the first case, the time of flight τ is directly measured and $\tau \propto 1/\beta$. In the second case, the Cherenkov angle Θ_C is measured. Because $\Theta_C \propto 1/\beta$ also here the velocity can directly be determined. With the velocity, $\beta\gamma$ can be calculated. The particle momentum is obtained from the curvature ρ of the particle trajectory. In a magnetic field B, $p \propto q\rho B$, where q is the charge of the particle. Inserting these results to Eq. 1.1, the mass of the particle can be obtained. Another method for PID is the measurement of the mean energy loss per unit path length $\mathrm{d}E/\mathrm{d}x$ of a particle. The energy loss in a given medium is a function of $\beta\gamma$ and, therefore, varies for different particles.

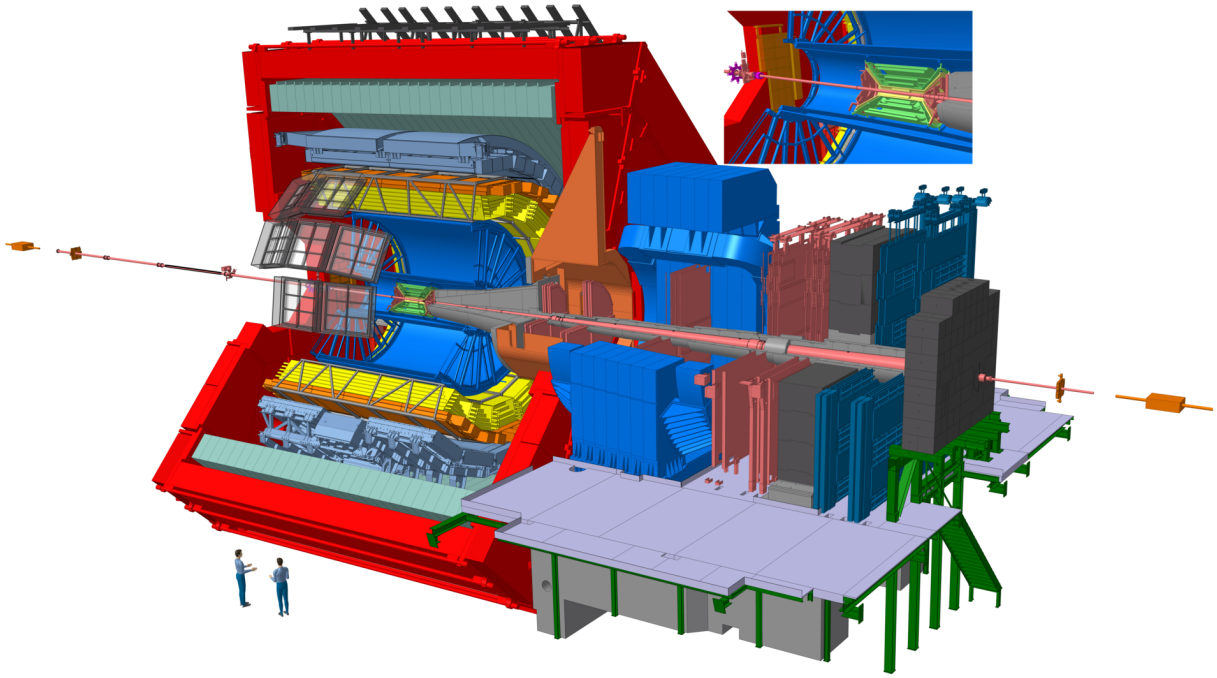

Figure 1.3: Schematic view of the ALICE detector [14].

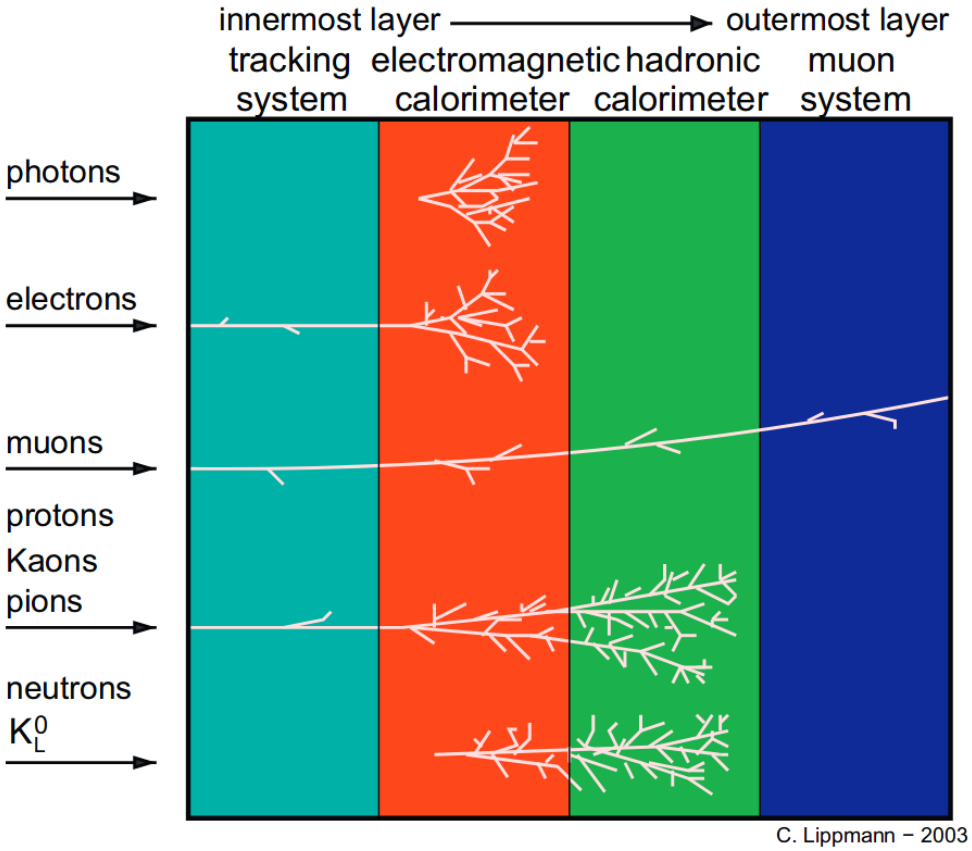

Figure 1.4: Particle signatures in the components of a generic collider experiment [13].

1.3 Challenges and opportunities in RUN 3

In RUN 3, which will take place from 2021 - 2023, an increase in luminosity is foreseen leading to interaction rates of about 50 kHz in Pb–Pb. This requires significant upgrades of the detector systems in order to be able to cope with the resulting data rates [15]. In particular, the current operational scenario of the ALICE TPC with gated Multi-Wire Proportional Chambers (MWPC) [16] is limited to a readout rate of maximally ≈ 3.5 kHz. Since the maximal drift time of electrons in the TPC is 100 µs, an average pile-up of ≈ 5 events is expected at interaction rates of 50 kHz. This demands for continuous readout, implying a major upgrade to the readout chambers. Indeed, the currently operated readout chambers will be fully replaced.

The data rates from the detectors increases from 51 GB/s to more than 3 TB/s [15, 17]. Therefore, not only the detector needs to be upgraded but also the computing system and the corresponding software framework. The new O^2 computing scheme [18, 19] brings a change of paradigm: Instead of a fast but limited online (High-Level Trigger (HLT) [20]) and, separately, a slow but precise offline infrastructure (AliRoot [21]) a common software framework needs to be put in place. To reduce the enormous amount of data recorded with the detector it needs to be pre-processed online during data taking (synchronous processing) instead of rejecting complete events as does the HLT. The new system will perform a partial

calibration and reconstruction online and compress the data, which is then stored to a disk buffer. During phases of no beam, the available computing resources are used for post-processing (asynchronous processing) where full calibration and reconstruction are conducted. Afterwards the data is stored to permanent storage at a heavily reduced rate of $< 100\,\mathrm{GB/s}$.

2 The ALICE TPC

2.1 Time Projection Chambers

Time Projection Chambers [22] typically consist of a gas filled vessel embedded between two electrodes. Figure 2.1 shows a schematic view of a TPC. Ionizing particles (purple) pass through the gas volume (green) of the TPC and generate electron-ion pairs (red, blue) upon impact ionization. The drift field E_{drift} that is applied between the cathode and the anode prevents those pairs from recombining and makes them drift towards the anode and cathode, respectively. Upon reaching the anode, the electrons induce a signal. Since on average only few electron-ion pairs are produced in each collision with the gas, the amplitude of the induced signal at the anode is not high enough to be observed by the readout electronics. Hence, the electrons have to be multiplied, which can be conducted using a variety of technical implementations. After amplification the signals are read out at the segmented readout anode. These signals are proportional to the energy loss of the particle allowing for particle identification via the specific energy loss $\mathrm{d}E/\mathrm{d}x$. The segmentation of the anode allows for a precise localization of the electrons on the readout anode. Combining this position information with the electron drift time, where the start time of the drift is given by the time stamp of the event, one can reconstruct the full three-dimensional spatial information. Thus, full 3D-tracking of ionizing particles can be realized with the TPC. The magnetic field forcing particles on helical trajectories allows for momentum measurements. Their radius is proportional to the magnetic rigidity.

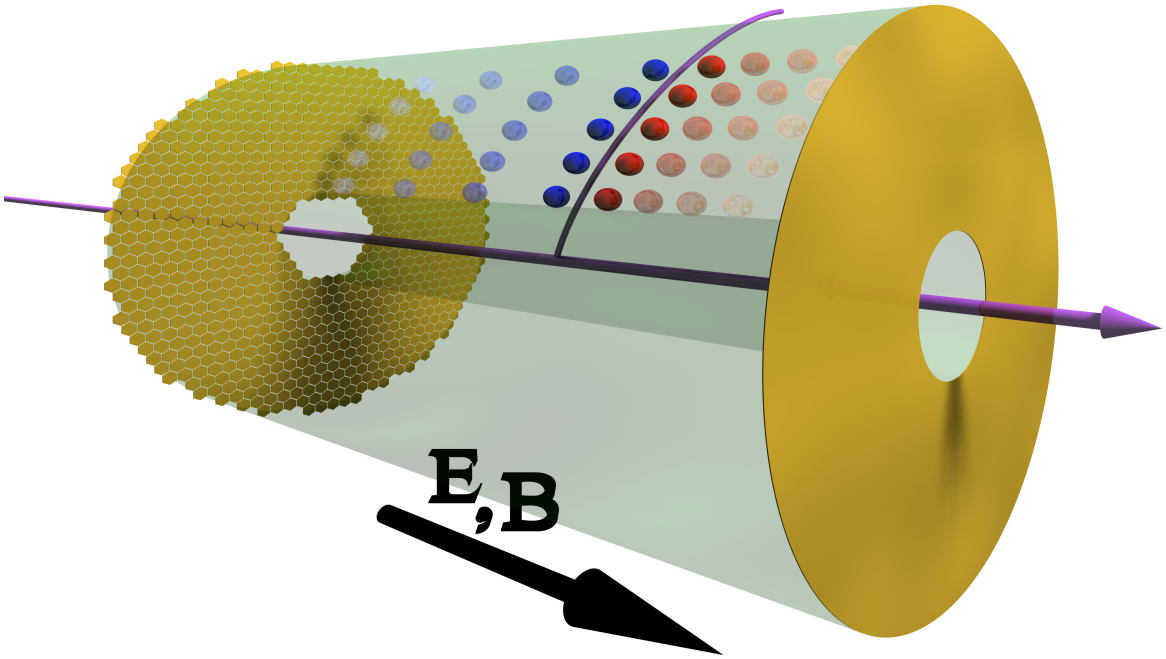

Figure 2.1: Scheme of a generic TPC in a magnetic field [23]. The purple arrows represent particles, the blue and red dots are electrons and ions. The fading colors indicate the drift of the electrons and ions. The segmented anode is on the left and the cathode on the right side. The active volume is colored green.

2.2 Particle identification

One method to identify particles is the simultaneous measurement of energy deposit and momentum. As discussed above, a traversing charged particle undergoes inelastic collisions with the gas atoms in the active volume of the detector. The particle loses a small fraction of its kinetic energy, leaving the gas atoms or molecules in ionized or excited states. The average energy loss of the particle per unit path length $\langle \mathrm{d}E/\mathrm{d}x \rangle$ is converted into an average number of electron-ion pairs $\langle N_I \rangle$ produced along the length x along the particle trajectory [25].

$$x\langle \frac{\mathrm{d}E}{\mathrm{d}x} \rangle = \langle N_I \rangle W \tag{2.1}$$

where W is the average amount of energy that was spent to produce an electron-ion pair. For Ne-CO_2-N_2 (90-10-5), the gas in the ALICE TPC, $W = 37.3\,\mathrm{eV}$. The electrons created in the collisions between the charged particle and the atomic electrons are called primary electrons. In subsequent collisions those electrons ionize or excite further gas atoms and

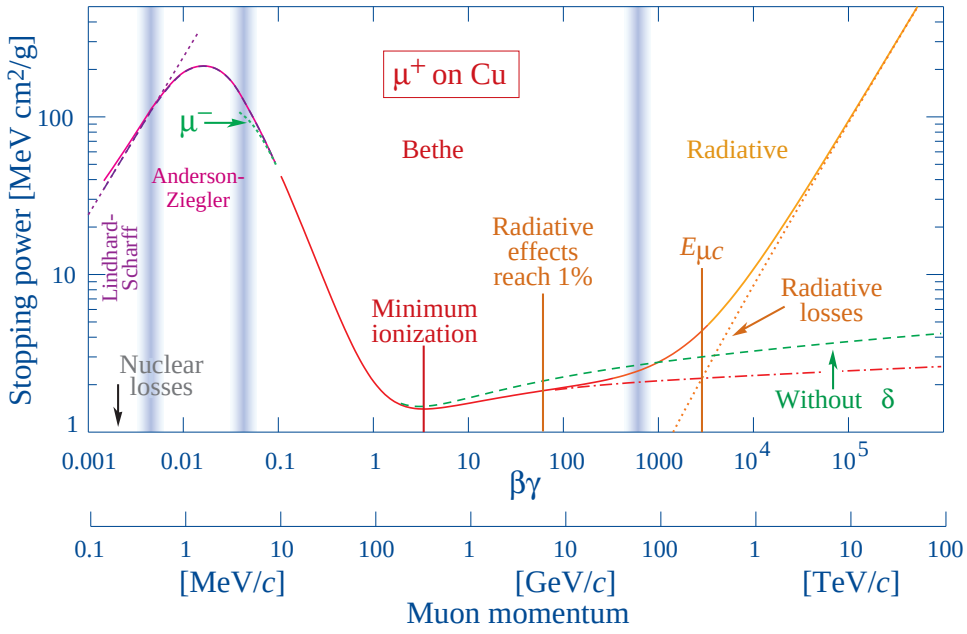

Figure 2.2: Exemplary Bethe-Bloch curve for muons traversing copper. [24]

lose all their kinetic energy. The electrons created in these secondary interactions are called secondary electrons. The primary ionization $\langle N_I \rangle = 14\,\text{electrons/cm}$ and the total ionization including secondary electrons $\langle N_t \rangle = 36.1\,\text{electrons/cm}$ for a so-called minimum ionizing particle (MIP) in this gas mixture. Particles are considered to be MIPs if their $\beta\gamma$ is in the range of the dip in the Bethe-Bloch curve, which is at $\beta\gamma \approx 3-4$ (see Fig. 2.2). In collisions with an especially large energy transfer, so-called δ-electrons with energies of up to several tens of keV are produced. Those high-energy electrons do not only produce secondary electrons, but may even leave the active detector volume.

In 1930 Hans Bethe was first to calculate the average energy loss per unit track length based on the scattering theory [26]. A modified Bethe-Bloch formula, neglecting higher-energy δ-electrons, valid for electrons and heavier particles can be written as [25]

$$\langle \frac{\mathrm{d}E}{\mathrm{d}x} \rangle \propto \frac{z^2}{\beta^2} \left(\log \frac{\sqrt{2m_e c^2 E_{cut} \beta\gamma}}{I} - \frac{\beta^2}{2} - \frac{\delta}{2} \right). \tag{2.2}$$

In this equation, I is the effective ionization energy of the material in eV and ze is the charge of the incident particle. δ is a correction to a density effect, calculated by Fermi [27]. E_{cut} introduces an upper limit for the energy transfer in a single collision, removing the higher-energy δ-electrons. Depending on the magnetic field typical values for E_{cut} lie in the range of 10 - 100 keV. Figure 2.2 shows an energy loss curve for μ^+ traversing copper and the typical shape of the energy loss. The red part is described by Eq. 2.2. In the region below $\beta\gamma = 0.5$ the energy loss decreases like $1/\beta^2$. At $\beta\gamma \approx 3-4$ a broad plateau close to the point of minimum ionization is reached. The energy loss increases with $\log \beta\gamma$ towards higher $\beta\gamma$ and approaches a constant value (Fermi Plateau). Above $\beta\gamma \approx 1000$ radiative losses dominate the energy loss. In that region the Bethe-Bloch formula no longer describes

the energy loss.

For a given particle, the number of collisions is distributed according to a Poisson distribution and the energy transferred in a collision according to a power law $\sim 1/E^2$. Hence, the actual value of energy loss ΔE per path length x is governed by statistical fluctuations. The resulting energy loss distribution $F(x,\Delta)$ is called straggling function. Assuming that the energy loss is completely deposited in the sensitive detector material, the distribution of the number of electron-ion pairs N_I along the particle path length x can be obtained from $F(x,\Delta)$. In the case of gaseous detectors, the theory of so-called thin absorbers has to be considered, where only a fraction of the kinetic energy is lost in the ionization processes. The possibility of large energy transfers in single collisions add a long tail in the high energy region, shifting the mean value of the distribution to much higher energies than its most probable value (MPV). Figure 2.3 shows an exemplary straggling function for 500 MeV pions in silicon. The tail towards higher energy loss clearly skews the distribution and arises rather independently of the traversed medium.

The specific energy loss can be used to identify particles (see Eq. 2.2). The signal amplitude in gaseous detectors is proportional to the number of ionization electrons liberated along the track length Δx. In order to mitigate the influence of statistical fluctuations in the energy loss distribution, a large number of samples along the particle track is measured (up to 158 in the ALICE TPC). For a sufficient number of measurements N_R, the pulse height distribution approaches the straggling function. To obtain a good estimator of the mean value of the pulse height measurements R_i, a truncated mean $\langle R \rangle_{\text{trunc}}$ is used instead of the mean value, which is sensitive to the long high energy tail. The truncated mean is defined as

$$\langle R \rangle_{\text{trunc}} = \frac{1}{a \cdot N_R} \sum_{i=1}^{a \cdot N_R} R_i, \tag{2.3}$$

where $R_i \leq R_{i+1}$ for $i = 1,...,n-1$ and a, typically between 0.5 and 0.85, is the lower fraction of measurements to be considered for the calculation of the truncated mean value. By removing signals from the high energy tail, the straggling function approaches a Gaussian distribution, which significantly facilitates the extraction of the mean value. On the other hand, it is also possible to obtain a good estimate of the mean value from the full information available. However, a maximum likelihood fit to all N_R ionization measurements would be needed, which is much more complicated than the truncated mean and does not yield significantly better results [25, 28].

To distinguish between particles, only relative values of the deposited energy $\Delta = \Delta(m,\beta)$ are needed. Figure 2.4 shows specific ionization curves for different particles. The measured ionization is parametrized with five parameters as outlined in [25]. As stated in Eq. 1.1 $\beta\gamma$ is a function of momentum/mass ratio. Therefore, the simultaneous measurement of p and Δ are sufficient to identify the particle of interest since a unique energy loss curve for different particles species ensues.

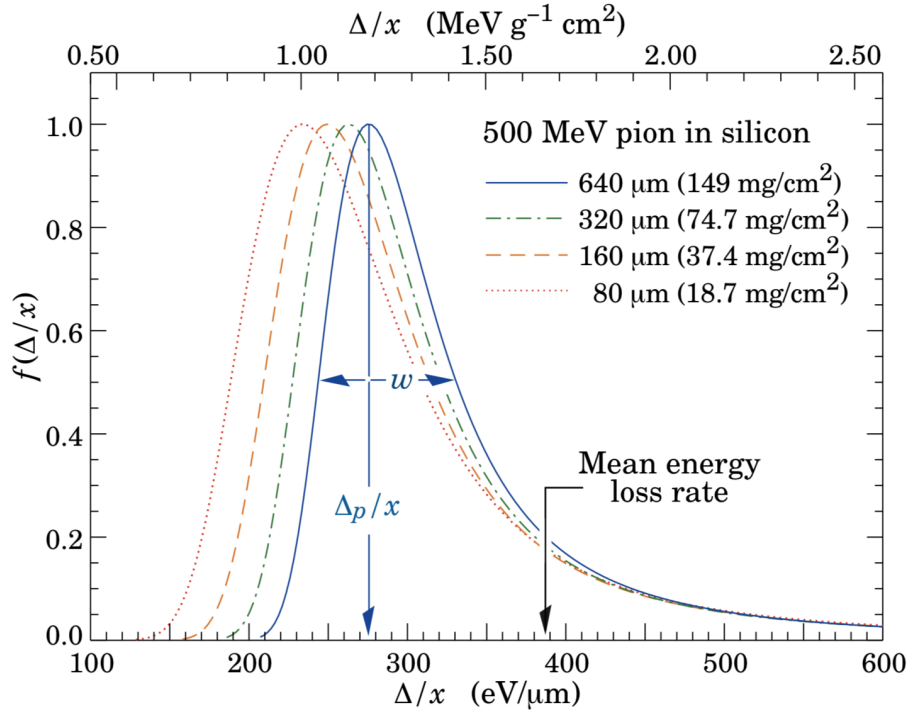

Figure 2.3: Exemplary straggling function for 500 MeV pions normalized to unity at the most probable value [24]. The width ω is the full width at half maximum.

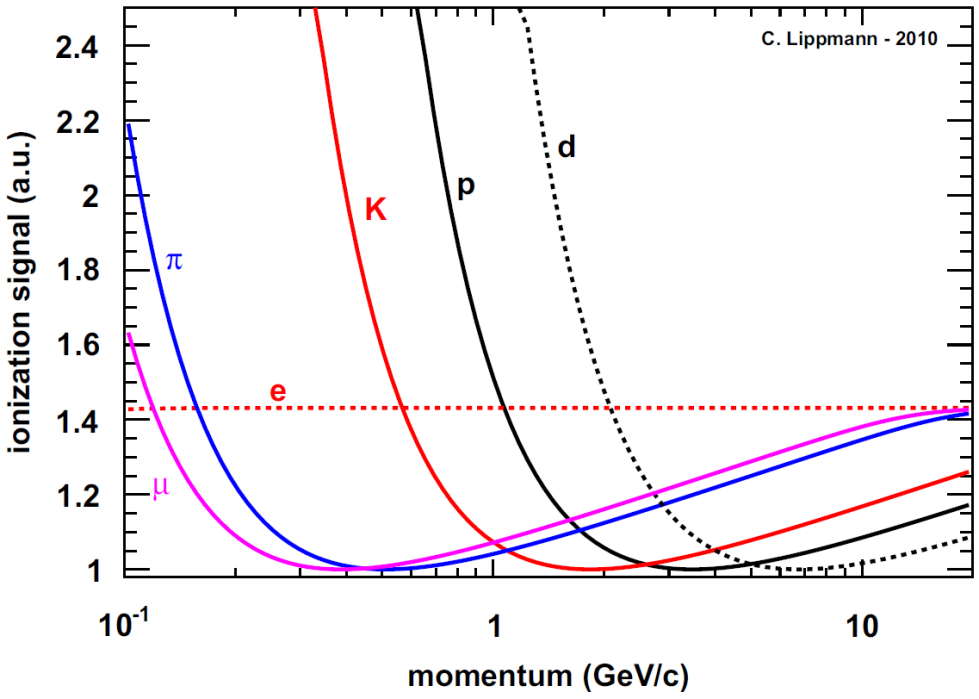

Figure 2.4: Exemplary ionization curves for different particles as a function of the particle momentum [13].

The energy resolution in the ionization measurement given by the variance of the Gaussian distribution of the truncated mean values can be defined as

$$\mathrm{d}E/\mathrm{d}x \text{ resolution} = \frac{\sigma_{\langle \mathrm{d}E/\mathrm{d}x\rangle_{\mathrm{trunc}}}}{\mu_{\langle \mathrm{d}E/\mathrm{d}x\rangle_{\mathrm{trunc}}}}, \tag{2.4}$$

where $\mu_{\langle \mathrm{d}E/\mathrm{d}x\rangle_{\mathrm{trunc}}}$ is the mean value and $\sigma_{\langle \mathrm{d}E/\mathrm{d}x\rangle_{\mathrm{trunc}}}$ is the width of the Gaussian fit to the $\langle \mathrm{d}E/\mathrm{d}x\rangle_{\mathrm{trunc}}$ distribution. A measure of how well two different particle types can be differentiated using the $\mathrm{d}E/\mathrm{d}x$ information is the separation power. It is defined as the distance between the mean values of the energy loss distributions of the two particle species in terms of the geometrical mean value of the corresponding widths. The separation power can be obtained from the $\langle \mathrm{d}E/\mathrm{d}x\rangle$ distributions and is defined as

$$\text{Separation power} = \frac{2 \cdot |\mu_{\langle \mathrm{d}E/\mathrm{d}x\rangle_{\mathrm{trunc}},\pi^-} - \mu_{\langle \mathrm{d}E/\mathrm{d}x\rangle_{\mathrm{trunc}},e^-}|}{\sigma_{\langle \mathrm{d}E/\mathrm{d}x\rangle_{\mathrm{trunc}},\pi^-} + \sigma_{\langle \mathrm{d}E/\mathrm{d}x\rangle_{\mathrm{trunc}},e^-}}, \tag{2.5}$$

for the exemplary case of electrons and pions.

2.3 Drift and diffusion

The drift field between the cathode and the readout chamber separates the ionization electrons and ions and accelerates them towards the anode and cathode, respectively. However, the charges encounter collisions with the atoms or molecules of the detector gas randomize the drift path on a microscopic scale. These collisions also decelerate the electrons. Together with the acceleration of the external electric field, this results in a constant drift velocity v_{drift} for $t \gg \tau$, where τ is the characteristic time between two collisions. The drift velocity can be described as [25]

$$v_{\mathrm{drift}} = \frac{eE_{\mathrm{drift}}}{m} \cdot \tau = \mu E_{\mathrm{drift}}, \tag{2.6}$$

where μ is the mobility of the electron. In Ne-CO_2-N_2 (90-10-5), the gas of the ALICE TPC in RUN 3, $v_{\mathrm{drift}} = 2.58\,\mathrm{cm\,\mu s^{-1}}$.

Due to the random collisions with the detector gas, the electron paths are also randomized to a certain degree in a process called diffusion. In the absence of an electromagnetic field, elastic collisions and the Coulomb field of a point-like electron cloud will lead to its isotropic spread. After the time t a Gaussian distribution with a width of $\sigma = \sqrt{2Dt}$, where D is the diffusion coefficient, will ensue. D depends on the detector gas. Introducing an electric field E_{drift} leads to a preferred direction of the diffusion. The diffusion coefficient has to be considered separately for the direction longitudinal (D_{L}) and transversal (D_{T}) to the field.

Overall, the spread can be written as

$$\sigma_{\mathrm{L,T}} = \sqrt{\frac{2D_{\mathrm{L,T}}l}{\mu E_{\mathrm{drift}}}} \tag{2.7}$$

where l is the travelled distance. On one hand, a certain amount of diffusion in transverse direction increases the spatial resolution depending on the size of the readout pads. In case the charge is arriving on a single pad, the spatial resolution is simply given by $d/\sqrt{12}$, where d corresponds to the width of the pad. When the charge is spread over more pads, a center of gravity method can be used to localize the center of the electron cloud, resulting in a smaller uncertainty. The same holds for the z direction. Longitudinal drift spreads the read out signal in time direction and enables proper sampling, which increases the energy resolution. On the other hand, too much diffusion in both directions has the opposite effect. The integrated charge remains the same but is spread over more pads and time bins leading to a decrease of the signal to background ratio, which ultimately results in a worse energy resolution. Therefore, diffusion can be a limiting factor for the detector performance.

2.4 Amplification

The working principle of electron amplification in different gas detectors is conceptually very similar. An electric field configuration is applied in a way that fields of the order of $10\,\mathrm{kV\,cm^{-1}}$ occur in certain regions of the detector. The ionization electrons gain sufficient energy in these electric fields to further ionize gas atoms. This process repeated many times results in an electron avalanche. The number of electrons in the avalanche grows exponentially with the traveled distance x according to the Townsend coefficient α as [25]

$$n = n_0 \cdot e^{\alpha x}, \tag{2.8}$$

where $\mathrm{n_0}$ is the number of initial electrons. the Townsend coefficient depends on the electric field and the gas density. Figure 2.5 shows α as a function of the electric field strength for different gas mixtures. Not only does the behaviour of α differ but also the onset of the gain heavily depends on the gas mixture. Ar-based mixtures need significantly larger electric fields for electron amplification than Ne-based gases.

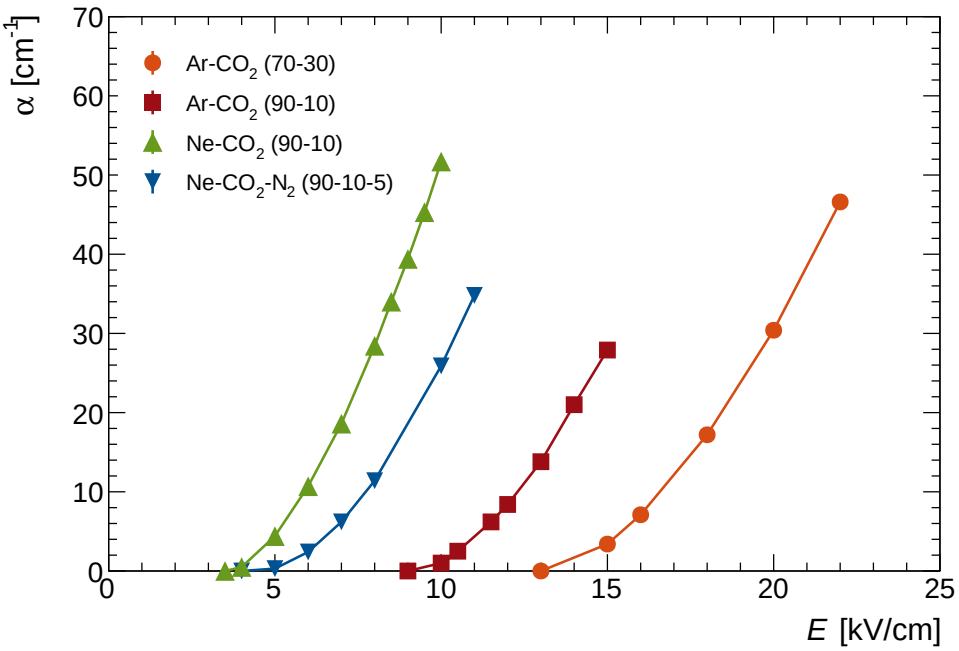

Figure 2.5: Effective Townsend coefficient as a function of the electric field strength for different gas mixtures [29–31].

2.5 Ion back flow

While the electrons created during the amplification process drift towards the anode, the ions, which are created in an equal number to the electrons, may escape the amplification region and drift towards the cathode in the center of the detector. The resulting ion back flow IB can be defined as

$$IB = \frac{I_{\mathrm{C}}}{I_{\mathrm{A}}}, \tag{2.9}$$

where I_{C} is the current measured at the cathode and I_{A} is the current at the anode. This entity corresponds to the number of ions drifting to the cathode per electron reaching the readout anode. On the way to the cathode, the ions traverse the drift volume of the TPC. Due to their slow drift velocity, this results in the built-up of space charge. In ALICE, it takes the ions $\approx 160\,\mathrm{ms}$ to travel the 250 cm from the readout chamber to the cathode resulting in remnant ions throughout following events. At a readout rate of 3.5 kHz the space charges from an event remain in the drift volume over the course of the next ≈ 560 events on average. In a homogeneous drift field, the ionization electrons drift along a straight line to the anode giving the location of the impact ionization in x- and y-direction. However, space charges lead to local modifications of the drift field and, therefore, change the drift direction and also the drift time of the electrons. This alters the tracking information in all directions resulting in a diminishing spatial- and $\mathrm{d}E/\mathrm{d}x$ resolution. Therefore, the homogeneity of the drift field is a crucial parameter for particle identification and tracking.

To ensure an optimal performance of the detector, the IBF has to be mitigated to an extent, where it can still be corrected for.

2.6 Overview on the ALICE TPC

The ALICE TPC [32] is the largest sub-detector of the ALICE experiment and the main device for tracking and particle identification. It consists of a gas filled, hollow cylindrical volume with an inner (outer) radius of 85 cm (247 cm), and a length of 500 cm along the beam axis covering the full azimuth angle and a $|\eta| < 0.9$ pseudo-rapidity interval. The Ne-CO_2 (90-10) filled gas volume is divided into two halves by the cathode in the middle, which together with a high-precision field cage defines the homogeneous electric drift field. The cathode voltage of $U_{cat} = 100\,kV$ defines the drift field of $400\,V\,cm^{-1}$. The magnetic field in the L3 magnet ranges from 0.2 to 0.5 T.

A schematic view of the TPC is shown in Fig. 2.6 showing the central cathode and the readout chambers. The segmented readout anode is sub-structured into 18 so-called sectors on every end-plate. Each sector covers 20° in azimuthal direction. The sectors consist of an Inner ReadOut Chamber (IROC) and an Outer ReadOut Chamber (OROC). In total this results in 72 readout chambers, which are currently equipped with Multi-Wire Proportional Chambers [16] that are operated at a gain between 7000 and 8000. The readout anodes in the ROCs are divided into 557,568 pads in total covering an area of $32.5\,m^2$. The TPC is capable of detecting particles in a transverse momentum range of $0.1 < p_T < 100\,GeV\,c^{-1}$.

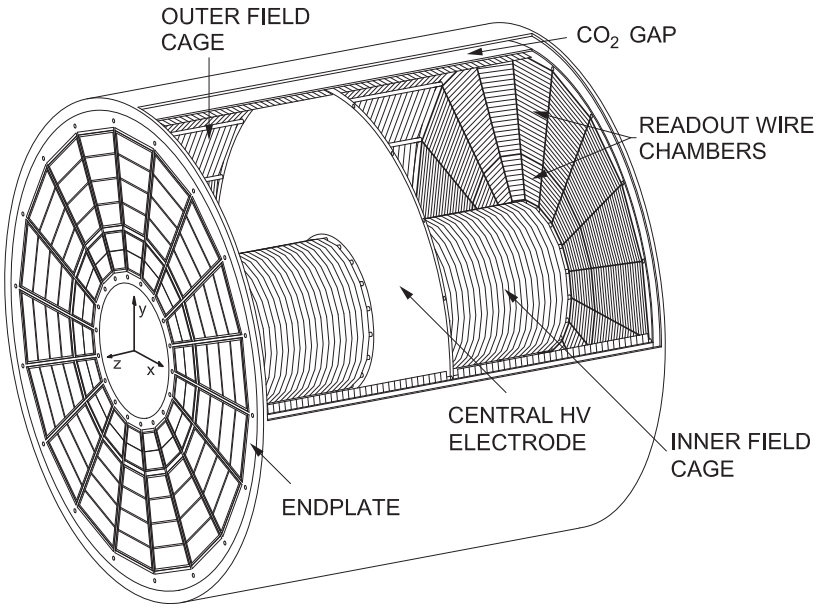

Figure 2.6: Scheme of the ALICE TPC showing the central cathode, the end-plates, the two types of readout chambers, and the field cage [32]. The coordinate system with the z-axis pointing along the beam axis is also displayed.

2.7 Operation with MWPCs

The readout chambers in the ALICE TPC were based on gated MWPCs [16] until the conclusion of RUN 2 at the end of 2018.

2.7.1 Working principle

The MWPCs typically consist of three layers of wires parallel to the pad plane (see Fig. 2.7). The layer closest to the anode is the anode wire grid followed by the cathode wire grid and the gating grid (not shown). Potentials are applied to the grids in a way that fields in the order of $10\,\mathrm{kV\,cm^{-1}}$ are reached in the vicinity of the anode wires so that electron avalanches are initiated by arriving ionization electrons. While the electrons created in this process are neutralized at the anode wires and do not contribute to the signal, the ions drift towards the cathode wires and, hence, induce mirror charges on the readout plane. These mirror charges create a signal that can be read out. Due to their low mobility, the ions follow the field lines rather closely. As depicted in Fig. 2.7 not all field lines lead towards the cathode wires, leading to significant charge leakage to the active drift volume. To reduce the amount of ion back flow, a third layer of wires, the gating grid, is placed above the cathode wires. The gating grid can be enabled by applying an alternating potential in a way that all field lines end on its wires. Figure 2.8 shows a simulation of the ion drift with an enabled gating grid. After all ions produced during the amplification process have been neutralized, the gating grid is disabled. In this state, the grid is transparent for electrons but when it is enabled, no electrons can reach the amplification region, hence, the detector is blind during this time. With the gating grid, the ion back flow can be reduced to $\mathcal{O}(10^{-}5)$.

In one readout cycle the gating grid is disabled for $\approx 100\,\mu\mathrm{s}$, which corresponds to a full TPC drift time, to make sure the ionization electrons reach the anode. Then the gate is enabled for $\approx 200\,\mu\mathrm{s}$ to neutralize the ions from the amplification. Figure 2.9 shows the fraction of collected ions as a function of the gating grid closure time. The onset of the collection curve marks the time that the ions need to reach the cathode wires. The second step results from ions reaching the closer gating grid wire, which is the left one in Fig. 2.8, and the last plateau is reached when the ions arrive at the wire further away. Due to this cycle the detection rate is limited to $\approx 3.5\,\mathrm{kHz}$ for pp collisions. However, in RUN 3 the interaction rate will be increased to $\approx 50\,\mathrm{kHz}$ in pp collisions. Considering the $100\,\mu\mathrm{s}$ electron drift time, there will be a pile up of ≈ 5 events on average [33]. This demands for continuous readout which cannot be conducted with gated MWPCs.

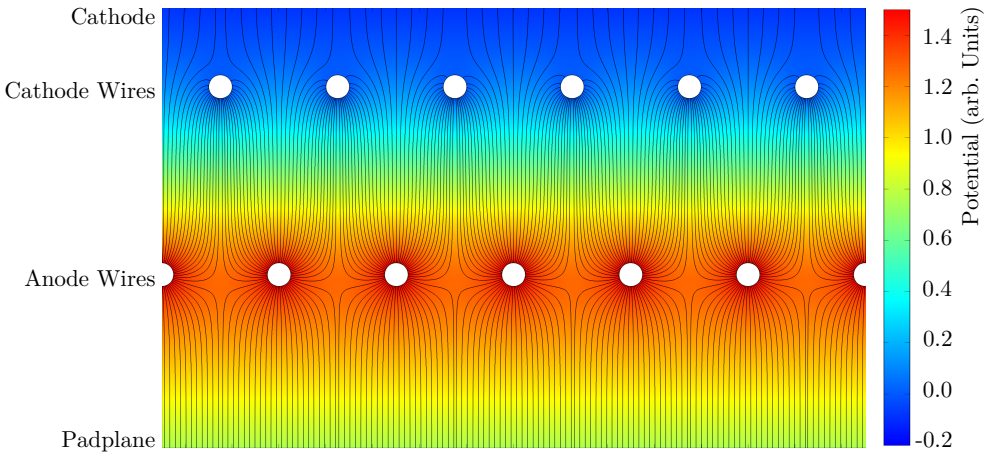

Figure 2.7: Exemplary field configuration in a MWPC. The field lines are depicted in black, the cross section of the wires is white and the potential is colored [23]

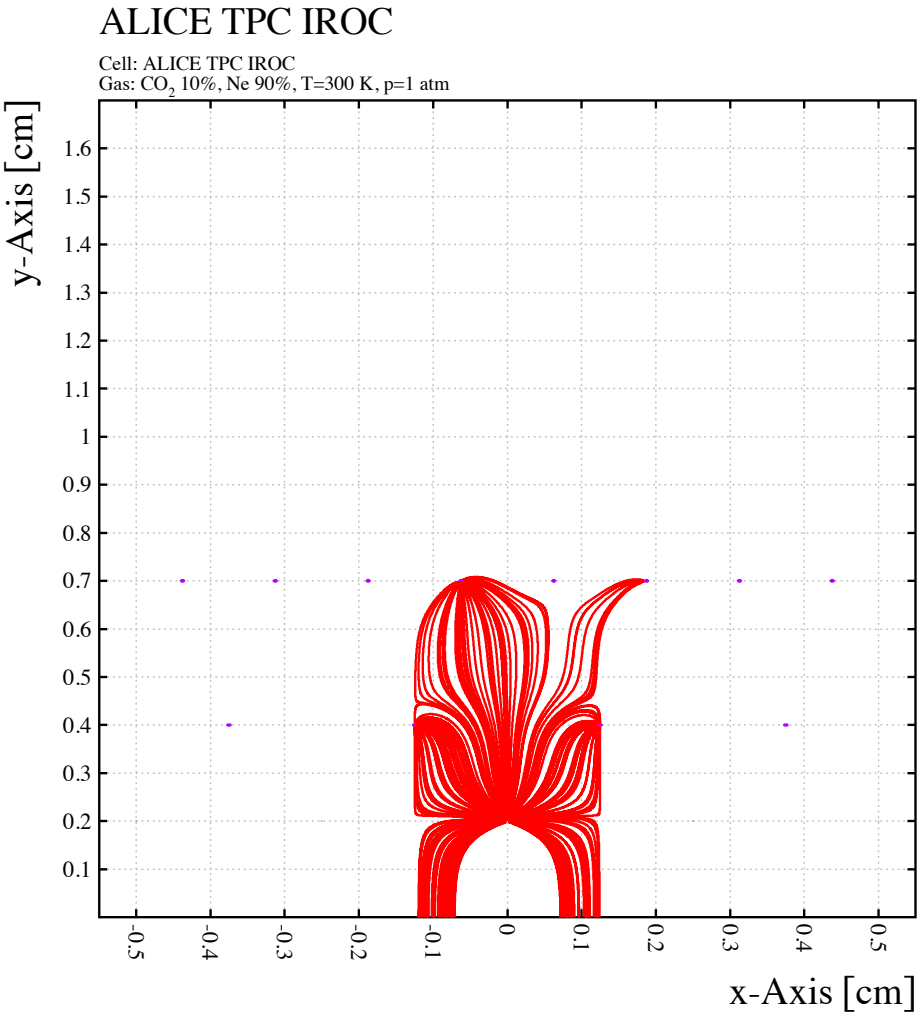

Figure 2.8: Simulation of the ion drift in a gated MWPC. The gating grid is enabled [34]. The cathode wires and the gating grid are located at $y = 0.4$ and $y = 0.7$.

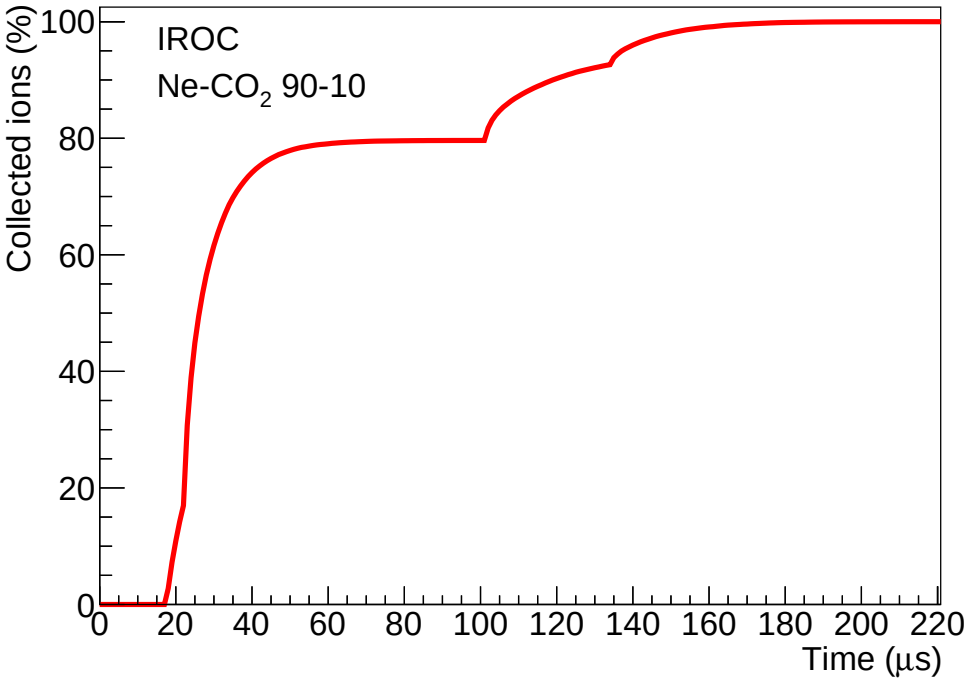

Figure 2.9: Ion collection as a function of gating grid closure time [34].

2.7.2 Performance

Figure 2.10 shows the energy loss as a function of momentum for various particles as measured with the ALICE TPC at a center of mass energy of 13 TeV in pp-collisions at $B = 0.2\,\mathrm{T}$ [14]. Depending on the particle momentum, the different types of particles can easily be identified. For tracks with the maximum number of signals (159), the energy resolution is 5 % in pp events [13]. The spatial resolution of the detector is shown in Fig. 2.11. Depending on the drift length and the inclination angle of the track the resolution in y-direction ranges from 0.4 to 2 mm at a pad size of 4 and 6 mm in y-direction. The resolution improves with increasing drift length because the diffusion spreads the signal across multiple pads. The y-position is calculated with a weighted mean using the signal amplitude as weights. Therefore, the resolution is much better than the pad size [32].

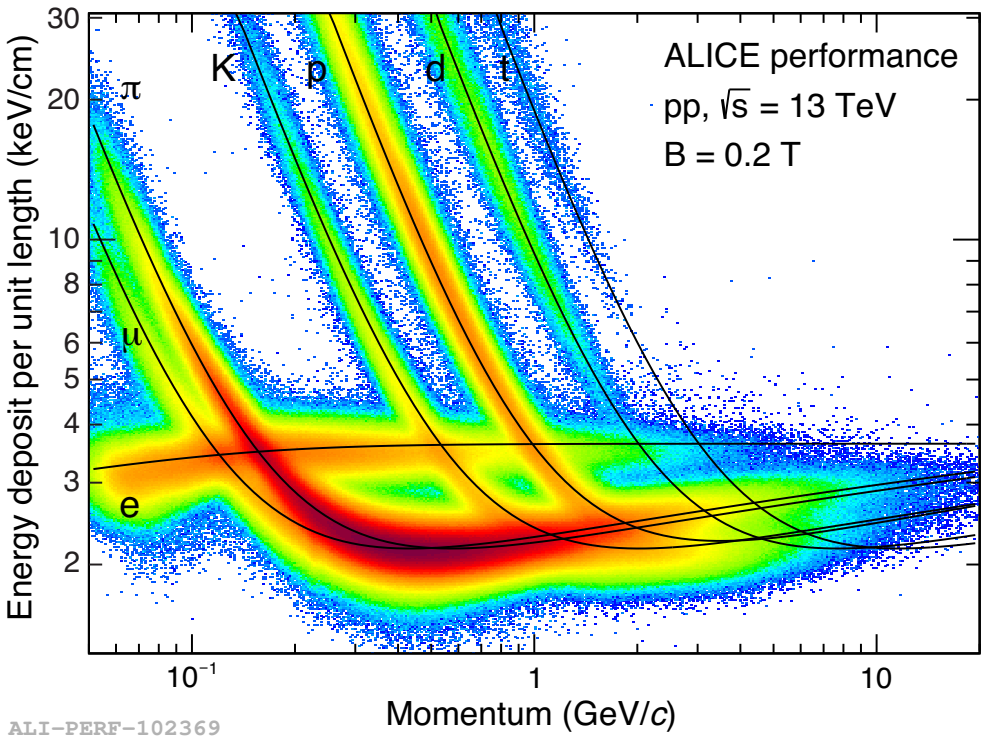

Figure 2.10: Energy loss as a function of particle momentum, showing the particle identification performance of the TPC for different particles.

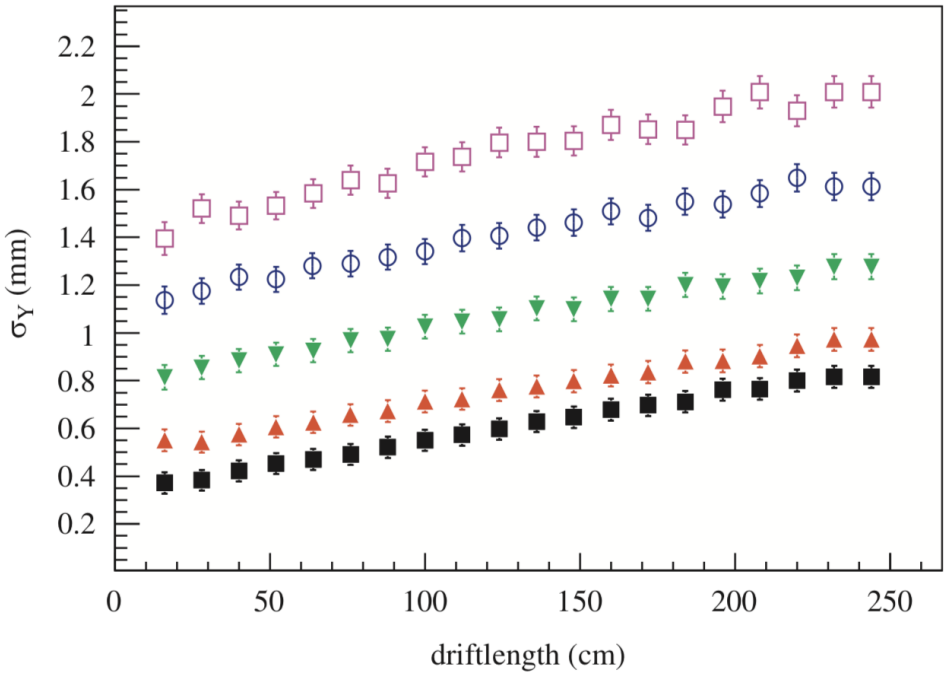

Figure 2.11: Space-point resolution in y-direction as a function of drift length [32]. The different symbols correspond to inclination angles from $\tan\alpha = 0$ (full squares) to 0.92 (open squares).

3 The TPC Upgrade

Due to the requirement of continuous readout planned for the RUN 3 data taking at the LHC, the ROCs of the ALICE TPC need to be completely re-designed [33, 35]. The MWPC-based ROCs will be removed and replaced by the GEM-based ROCs. Therefore, the TPC has been brought up to the surface and transported into a clean room at Point 2. The replacement of the readout chambers, installation of the new readout electronics, and commissioning will be finished in the fourth quarter of 2020.

3.1 Gas Electron Multipliers

The Gas Electron Multiplier (GEM) [36] was first introduced by F. Sauli in 1997 for particle physics experiments and can be allocated to the Multi-Pattern Gaseous Detector (MPGD) family [37]. Nowadays, a variety of experiments e.g. COMPASS [38], PHENIX [39], LHCb [40] and TOTEM [41] are using GEMs. GEM-based detectors will also be implemented in the detector upgrade of the ALICE [33, 35] and CMS [42] experiments.

Standard GEMs consist of a 50 µm thick insulator material (polyimide) that is covered with a 5 µm thin layer of copper on both sides. A micro-pattern of hexagonally arranged double conical holes with an inner and outer diameter of 50 µm and 70 µm is introduced. Depending on the hole pitch the GEMs are marked as standard (140 µm, SP) or large pitch (280 µm, LP) foils. Figure 3.1 shows a microscope picture of a standard GEM foil. In the cross section one can see the copper-polyimide-copper layer. Also the hexagonal hole pattern and the doubly conical shape of the holes is visible.

3.1.1 Electron amplification

By applying a potential difference ΔU_{GEM} in the range of 300 to 400 V between the top and bottom side of the GEM, electric fields of the order of several 10 kV cm^{-1} arise within the GEM holes. In such fields, avalanche amplification can occur as shown in Fig 3.2, where the amplification of two electrons entering a GEM hole is simulated with Garfield/Magboltz. When a GEM is operated within an external electric field, as shown in Fig. 3.3, an asymmetric field configuration can be set where the field below the GEM is stronger than above. In such a case, the probability of extracting an electron from the bottom side is increased. Additionally, many field lines end on the top side of the GEM resulting in the neutralization of back drifting ions, which follow the field lines rather closely

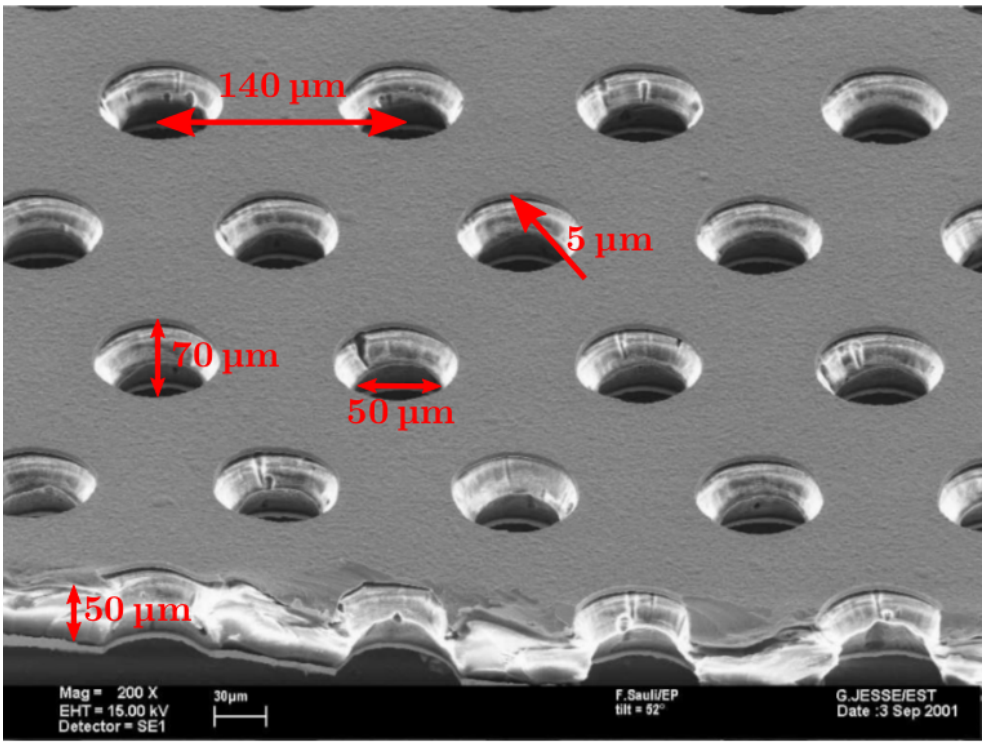

Figure 3.1: Dimensions of a standard GEM foil [38]

due to their low mobility. This is also observed in the Garfield/Magboltz simulation, where a significant amount of ions (red) move towards the top side of the GEM. The amount of IBF reduction is dependent on the High-Voltage (HV) configuration (see Sec.3.2). In contrast to the MWPC, a GEM does not need a further structure to support the IBF reduction but it provides the ion collection intrinsically. Therefore, a GEM enables continuous readout. The amplification in a GEM is subject to fluctuations and can be described by a Polya-distribution [43]. Figure 3.4 shows the multiplication in a GEM for a single incoming electron as a function for various effective gains and gas mixtures. In comparison to a MWPC, where these fluctuations are purely exponential, the losses in the collection and extraction processes are clearly visible.

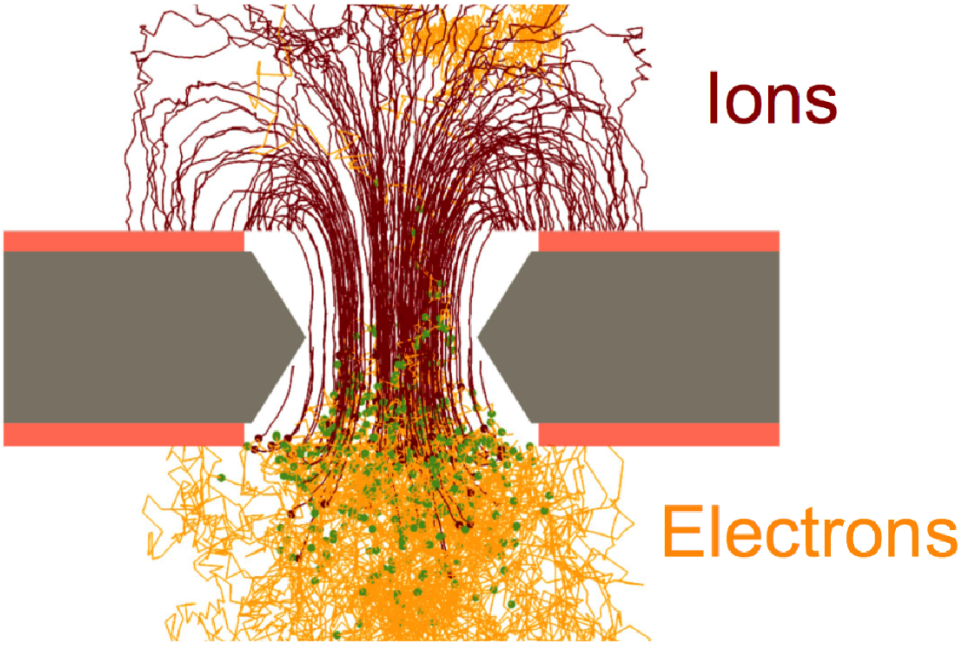

Figure 3.2: Garfield/Magboltz simulation of electrons entering a GEM hole [44]. Electrons drift paths are shown in yellow, ion drift paths are shown in red. Green dots indicate the locations of ionization processes.

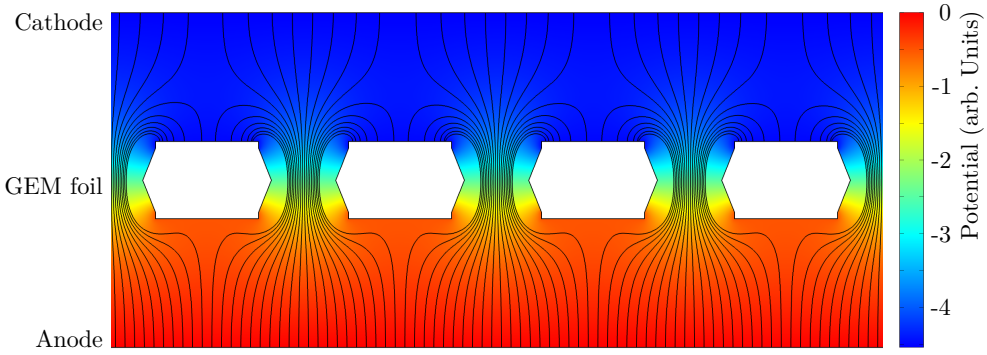

Figure 3.3: Exemplary potential configuration of a GEM foil. The field lines are depicted in black, the cross section of the GEM foil is white and the potential is colored [23]

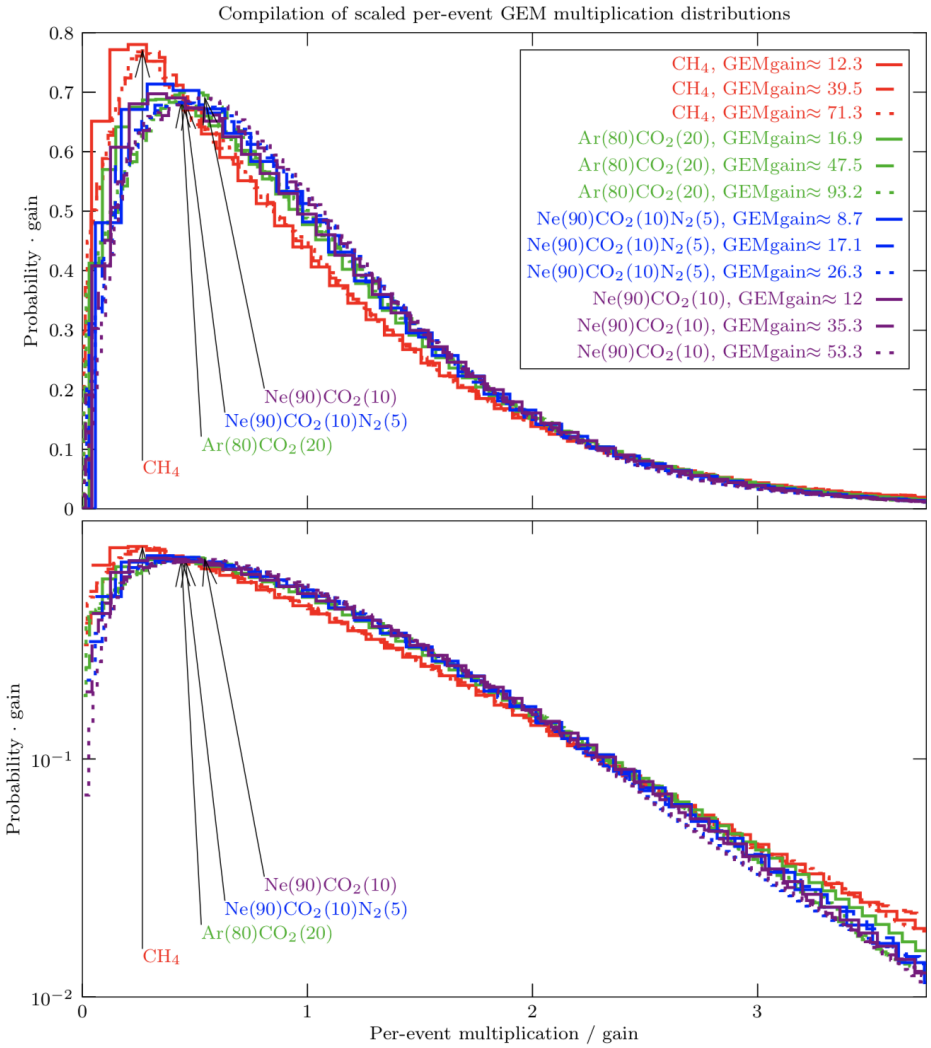

Figure 3.4: Distribution of the electron multiplication in a GEM for a single incoming electron for various effective gains and gas mixtures in a logarithmic (bottom) and non-logarithmic scale (top) [43].

3.1.2 Characterization

One of the main characteristics of a GEM is the effective gain G_{eff}. It is defined as

$$G_{\text{eff}} = \frac{I_{\text{A}}}{I_{\text{P}}}, \tag{3.1}$$

where I_{A} is the current measured at the anode, which is directly related to the number of electrons extracted from the GEM, and I_{P} is the primary current, corresponding to the number of ionization electrons. Overall, the effective gain shows how many electrons are recorded at the anode for a single electron in the drift volume. Exemplary curves of the effective gain for the three OROC stacks of a pre-production chamber are shown in Fig. 3.5.

The curves show the typical exponential behaviour reaching a gain over 10^4. The absolute gain G_{abs} of a GEM is the number of electrons created for a single electron entering a GEM hole. The difference in effective and absolute gain arises from the collection efficiency ε_C and extraction efficiency ε_E. Due to the electric field configuration at a GEM, arriving electrons may be neutralized on the top side without entering a hole, which reduces ε_C. Also it is possible that electrons that were created inside the GEM hole drift towards the bottom GEM surface, reducing ε_E. Therefore, the effective gain can also be defined as

$$G_{\text{eff}} = \varepsilon_C \varepsilon_E G_{\text{abs}}. \tag{3.2}$$

An important issue in the operation with GEMs are electrical discharges. A discharge occurs when the number of charges in a GEM hole exceeds a critical limit, which is $(5-9)\cdot 10^6$ [45], depending on the gas mixture. During an electrical discharge a spark forms inside a GEM foil creating an electrical connection between the top and bottom side of the GEM. With its parallel copper areas the GEM acts as a capacitor. This means that the stored energy

$$W = \frac{1}{2}\varepsilon_0 \varepsilon_{\text{r}} E^2 A d \tag{3.3}$$

is released during a discharge. ε_{r} is the relative permittivity of the insulator material, ε_0 the dielectric constant, E the electric field between the copper surfaces, and d the distance between the copper surfaces. The energy W is released in a spark that potentially can create a permanent connection between the GEM electrodes and therefore render the detector effectively blind. Therefore, discharge mitigation is an important R & D topic to ensure safe operation [35] (see Sec. 3.2).

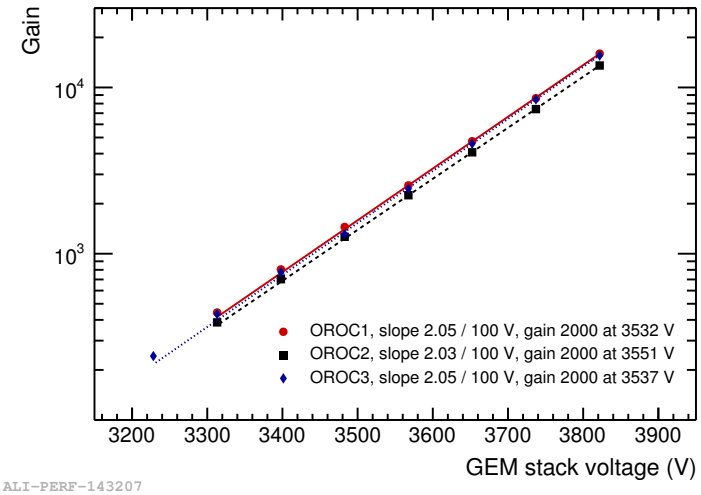

Figure 3.5: Gain curves for the OROC stacks [46]. The gain is measured as a function of the GEM stack voltage.

3.2 Technical implementation

The new readout chambers are assembled from an Aluminum body (Alubody), a pad plane, and a GEM stack with four layers. An exploded view of the IROC and OROC are shown in Fig. 3.6. While the IROC area can be covered with one GEM foil, the large OROC area needs to be divided into three stacks (OROC 1, OROC 2, OROC 3), since the raw insulator material that is used for the GEM production is not available in a sufficient size to cover the full OROC. The GEM dimensions are listed in Tab. 3.1. Each GEM stack of IROC and OROC 1,2 and 3 contains four GEMs.

This results in a total of 4 and 12 foils in an IROC and OROC module, respectively. The four GEM types are displayed in the photography in Fig. 3.7.

Figure 3.8 shows a detailed view of the GEM foil design. The brown and yellow areas depict copper and polyimide material, respectively. The frame on which the GEM foil is glued during the production process hosts 25 - 35 mounting holes depending on the GEM type, used to fix the GEM foils to the Alubody. Cutouts in the sides of the GEM frame are used as cable guides and two flaps on the foil serve as connectors for the HV powering. From there, a HV distribution circuit powers all GEM segments. For safety purposes, a loading resistor is mounted in between the power supply and every single GEM segment. In case

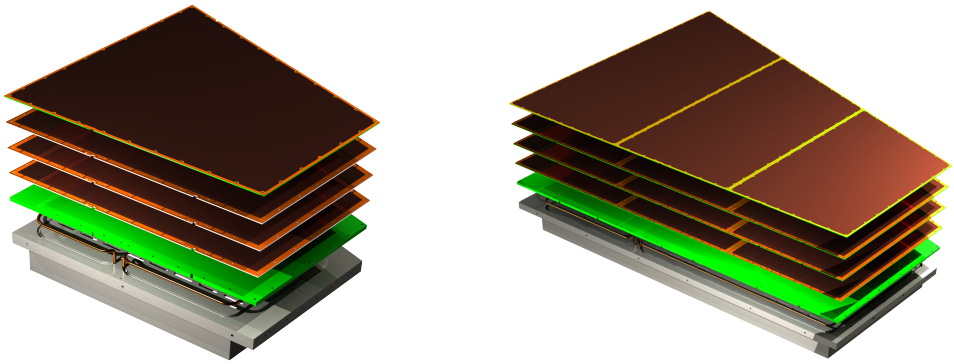

Figure 3.6: Exploded view of an IROC (left panel) and OROC (right panel) modules [**?**].

GEM type	Size (cm^2)	Active area (cm^2)	Sectors	Mean sector area (cm^2)
IROC	53.54×53.54	1665	18	92.5
OROC1	68.74×53.54	1738	20	86.9
OROC2	84.04×53.54	2299	22	104.5
OROC3	104.34×53.54	2932.8	24	122.2

Table 3.1: Dimensions of GEM foils in the ALICE TPC [46].

of an electric discharge, the resistor limits the current from the power supply to prevent further damages to the GEM. The active area of the GEM is divided into 18 segments for the IROC and 20, 22, and 24 for OROC1, OROC2 and OROC3, respectively. The segments become apparent in the picture, where an IROC foil with 18 segments is shown. This division into segments of ~ 100 cm^2 is implemented to ensure safe operation. First of all, as Eq. 3.3 indicates, the energy stored in the GEM is proportional to the segment area. Therefore, keeping the segments small reduces the released energy in case of a discharge and thus the probability of a fatal discharge. Secondly, in case a discharge does lead to a permanent electric connection between the top and bottom of a GEM, only one segment and not the whole GEM is rendered blind.

The pad plane is a 3 mm thick printed circuit board (PCB) and is divided into a total number of 5504 and 9856 pads for IROC and OROC, respectively. The pad size varies with increasing radius and is optimized to achieve the best possible $\mathrm{d}E/\mathrm{d}x$ resolution with the ALICE TPC. Also the shape of the pads varies from rectangular to trapezoidal shape from the center outwards (see Fig. 3.9). The pad dimensions are listed in Tab. 3.2. Via a routing scheme to the back side of the pad plane and flexible connectors the pads are connected to the readout electronics.

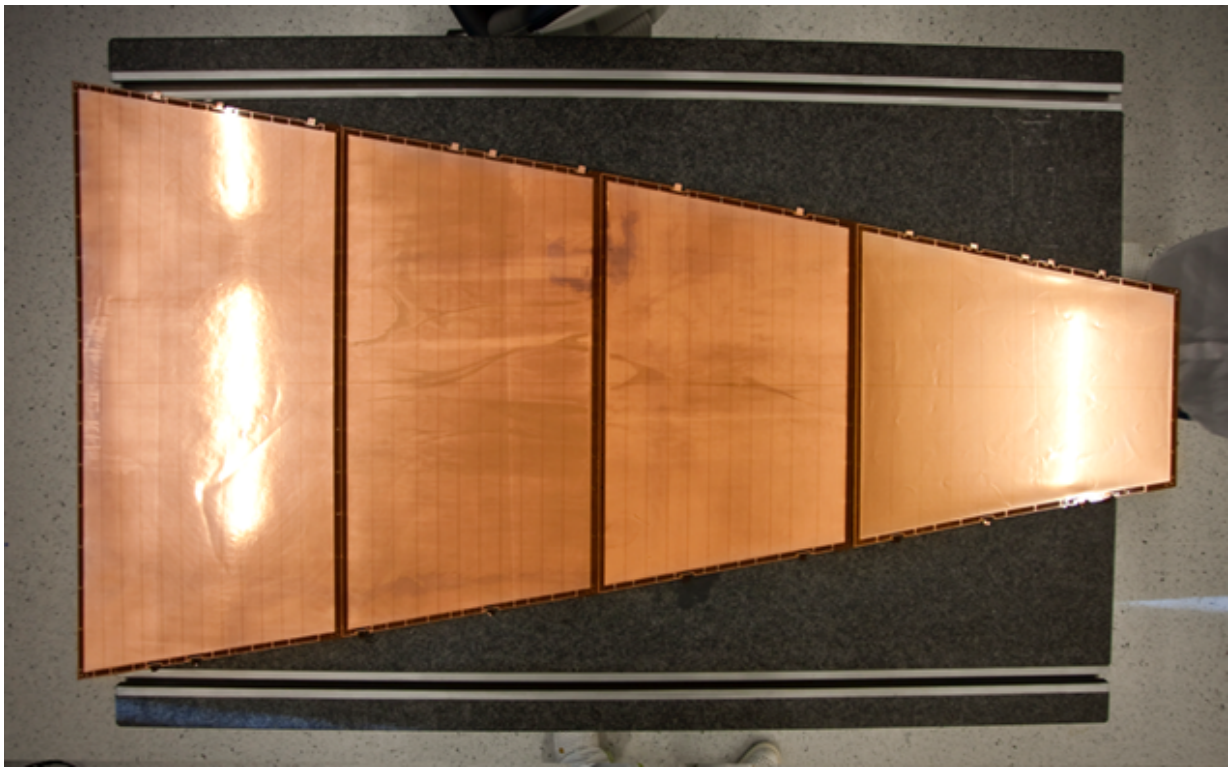

Figure 3.7: Photography of all GEM sizes. From left to right: OROC 3, OROC 2, OROC 1, IROC [47].

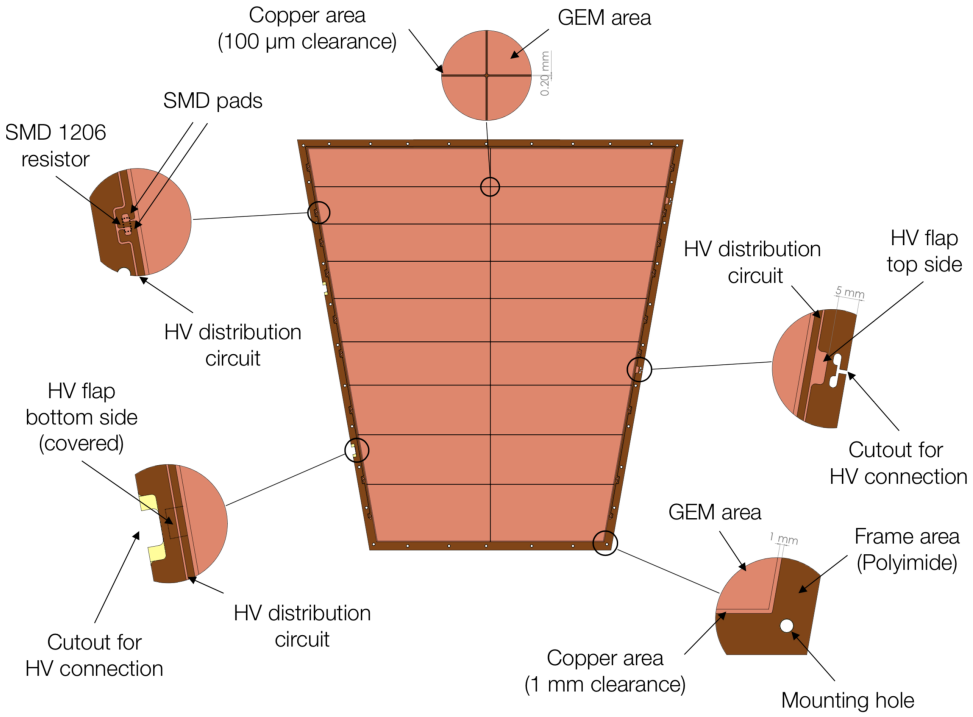

Figure 3.8: Detailed scheme of the GEM design showing the copper area (bright) and the frame material (dark) [46].

		Pad size (mm^2)	Number of rows	Number of pads
IROC	($841 < r < 1321$ mm)	4×7.5	63	5504
OROC1	($1346 < r < 1696$ mm)	6×10	35	2944
OROC2	($1716 < r < 2066$ mm)	6×10	35	3712
OROC3	($2086 < r < 2461$ mm)	6×15	25	3200
TPC total	(2×18 sectors)		158	552,960

Table 3.2: Dimensions and parameters of readout planes and pads [33].

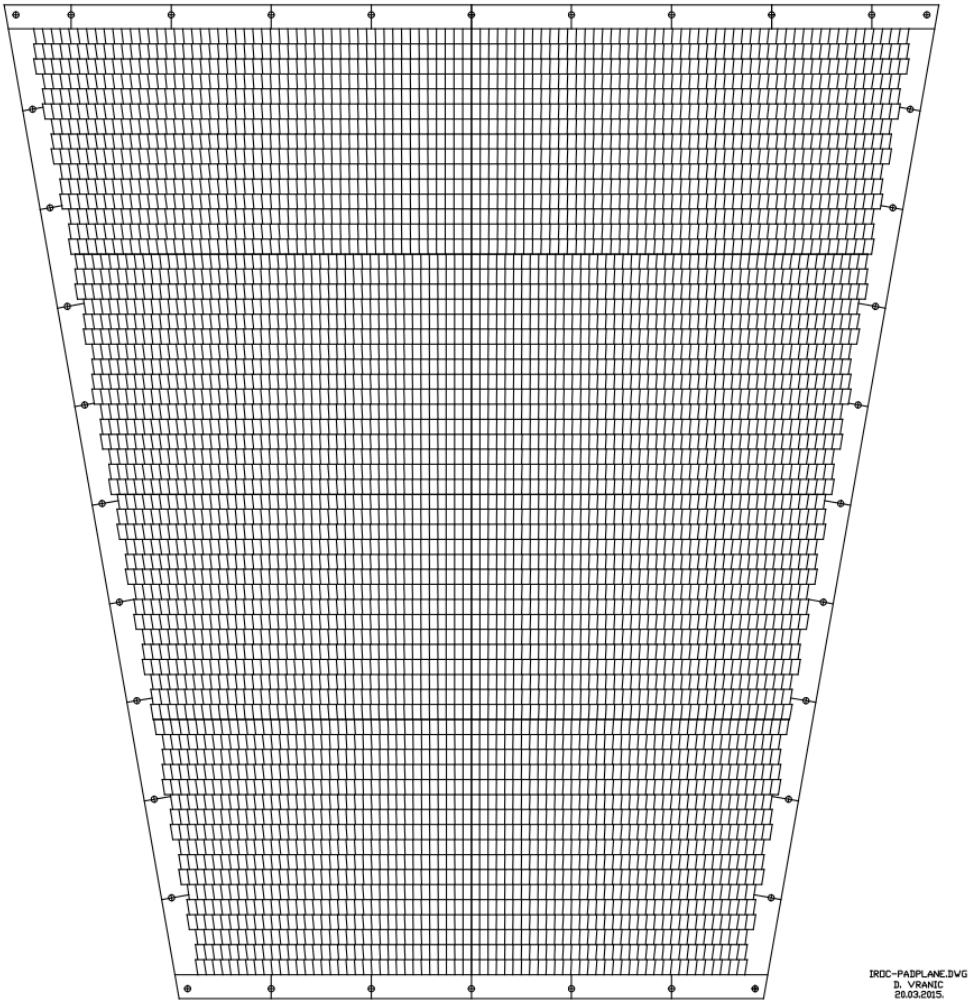

Figure 3.9: IROC pad plane scheme.

A schematic cross section of a GEM stack is shown in Fig. 3.10. The GEM foils are stacked at a 2 mm distance provided by the thickness of the GEM frames. Also the distance between the GEM 4 and the pad plane is 2 mm. The drift field E_{drift}, enabling the electron drift towards the GEM stack, is defined by the values of the voltage on the top side of the first GEM foil facing the drift volume $U_{\text{GEM 1,top}}$ and cathode voltage, located at 2.5 m from the read-out plane in the centre of the ALICE TPC, U_{cat}. The gaps between the GEMs are called transfer gaps and the gap between GEM 4 and the pad plane is the induction gap. GEM 1 through 4 are ordered in a specific configuration. While GEM 1 and 4 are standard pitch foils, GEM 2 and 3 are large pitch foils, where the hole pitch is twice as large. This creates a misalignment of the holes throughout the stack and increases the probability that

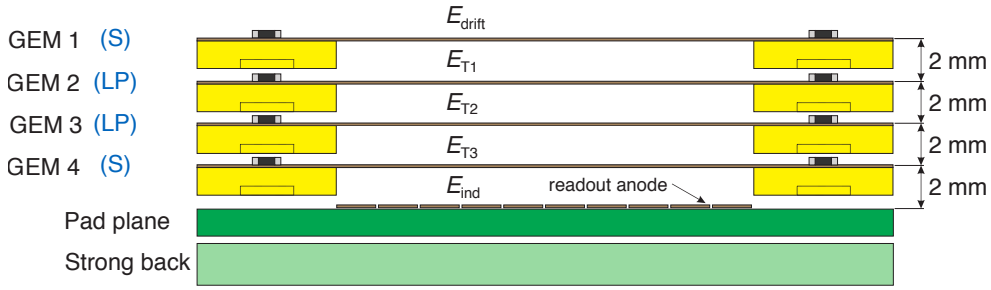

Figure 3.10: Scheme of a GEM stack indicating the distances between GEMs and relevant electrical fields.

a back drifting ion is neutralized on the bottom side of a GEM since the path from lower GEMs in the stack towards the drift volume is more convoluted [33, 48].

Electrons arriving at GEM 1 get collected into a GEM hole with the collection efficiency $\varepsilon_{C,1}$. After amplification, the electrons are extracted with the extraction efficiency $\varepsilon_{E,1}$ and transferred to the next GEM by E_{T1}, where the process is repeated until the electrons reach the induction gap where they induce the signal on the readout anode. Depending on the HV settings, the gain in the individual GEMs can be different. Also the ion back flow and the energy resolution depend on the gain distribution across the stack. Figure 3.13 shows the energy resolution measured with ^{55}Fe as a function of the ion back flow obtained for a variety of HV settings. The differently colored lines show ΔU_{GEM2} and the opened and closed squares indicate different $\Delta U_{\mathrm{GEM3}}/\Delta U_{\mathrm{GEM4}}$ ratios. The main influence arises from ΔU_{GEM1} which is increased from left to right. Therefore, mainly depending on ΔU_{GEM1} one has to find a compromise between ion back flow and energy resolution. To obtain less ion back flow the majority of the amplification shall happen in GEM 4 since the probability of the ions getting neutralized is much higher if they have to go through the whole GEM stack. Therefore, ΔU_{GEM1} has to be kept rather low compared to ΔU_{GEM4}. By increasing the gain in GEM 1, the energy resolution improves, due to a smaller dependency on gain fluctuations in single electron amplification. Figure 3.11 shows the simulation of a single electron amplification throughout the GEM stack for an IBF reduction setting. One can see the majority of the gain in the last GEM and also the very small amount of back drifting ions (red) from the first GEM upwards. Typical HV settings are shown in Tab. 3.3 for $IB < 1\,\%$ with an effective gain of $2 \cdot 10^3$. Note the highest ΔU_{GEM} in GEM 4 for reduced ion back flow. The low transfer field E_{T3} results in a field configuration that leads to a high ion capturing on the top side of GEM 4 where the majority of ions are created.

The discharge probability as a function of the gain measured with a quadruple GEM stack for different HV configurations is shown in Fig. 3.12. A mixed alpha source is used for irradiation. The discharge probability is defined as the probability of one alpha particle creating a discharge. It increases exponentially with the gain. For the low IB setting (red) the discharge probability rises much steeper than for higher IB. As mentioned above, the majority of the amplification is achieved in GEM 4 in the low IB setting. The higher discharge probability results from much more localized electrons approaching GEM 4 from the above GEM compared to the rather spread drifting electrons approaching GEM 1 in

the settings for higher IB. Therefore, the number of electrons in single holes in GEM 4 is higher for low IB than in GEM 1 for high IB. In combination with the high gain this leads to an increased discharge probability. Another measurement was done at the CERN SPS with a quadruple GEM stack. A discharge probability of $(6.4 \pm 3.7) \times 10^{-12}$ was obtained. This translates to about 600 expected discharges in the TPC in one month of Pb–Pb collisions at 50 kHz. With this number of discharges no damage to the GEMs and safe operation of the TPC is expected in RUN 3 and beyond [35].

In order to maintain the excellent PID capabilities of the MWPC-based TPC, the IB needs to be smaller than 1 % and the energy resolution measured with an ^{55}Fe source better than 12 %. In RUN 3 even an IB as small as 1 % will lead to distortions as large as 19 cm in r and 7 cm in $r\varphi$ close to the central electrode [35]. In 50 kHz Pb–Pb collisions, ions from 8000 events on average accumulate inside the drift volume. This implies that space charge corrections have to be applied to the data to restore the reconstruction efficiency and the final momentum resolution [33].

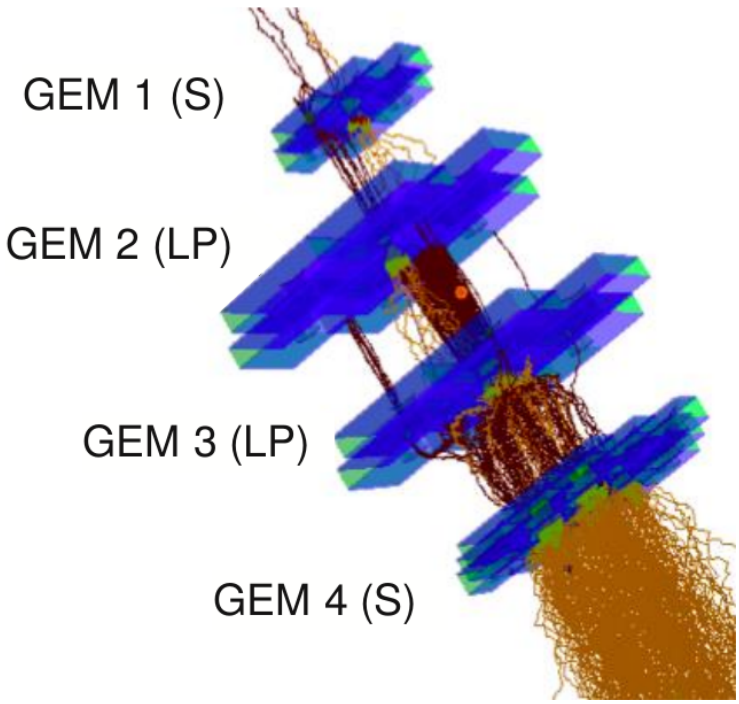

Figure 3.11: Simulation of one electron amplification throughout a quadruple GEM stack in an IBF reduction HV setting [33]. Ions and electrons are shown in red and yellow. The GEMs are indicated in blue.

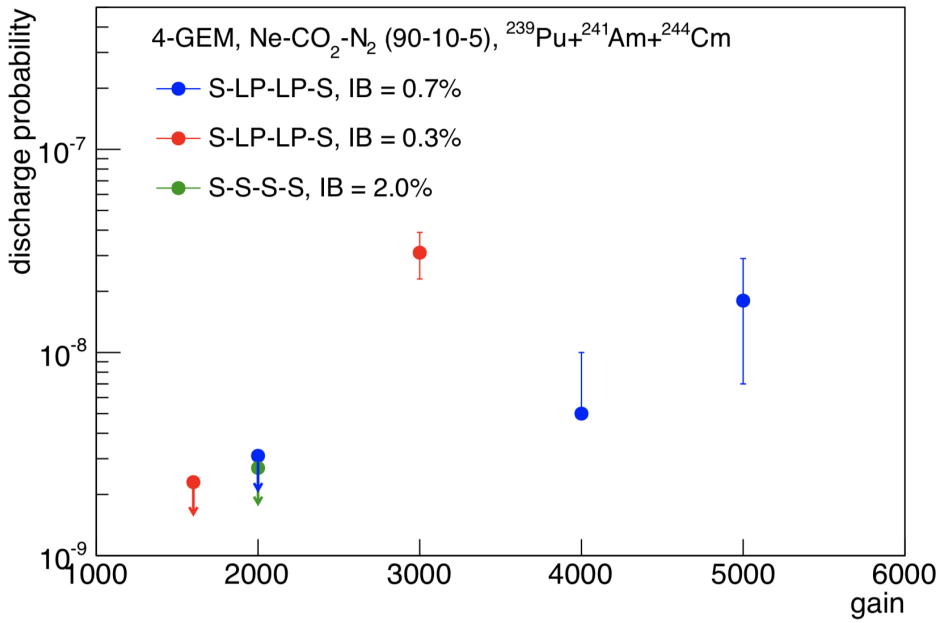

Figure 3.12: Discharge probability of a quadruple GEM prototype measured for different stack and HV configurations [49]. Upper limits for discharge probability are indicated with arrows.

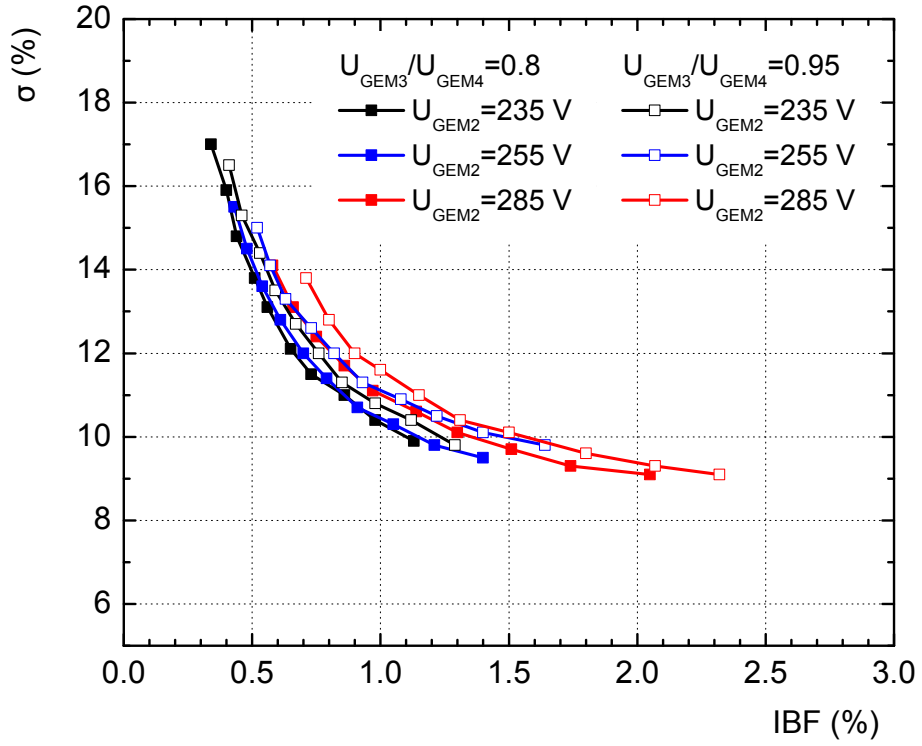

Figure 3.13: ^{55}Fe resolution as a function of the ion back flow for a variety of HV settings [33].

Drift Field				$0.4\,\mathrm{kV\,cm^{-1}}$
$U_{\mathrm{GEM\ 1,top}}$			$=3150\,\mathrm{V}$	
$\Delta U_{\mathrm{GEM\ 1}}$	$= U_{1,\mathrm{top}} - U_{1,\mathrm{bot}}$	$= 270\,\mathrm{V}$		
Transfer Field 1 (E_{T1})	$= (U_{1,\ \mathrm{bot}} - U_{2,\ \mathrm{top}})\,/0.2\mathrm{cm}$			$=4.0\,\mathrm{kV\,cm^{-1}}$
$U_{\mathrm{GEM\ 2,top}}$			$=2080\,\mathrm{V}$	
$\Delta U_{\mathrm{GEM\ 2}}$	$= U_{2,\mathrm{top}} - U_{2,\mathrm{bot}}$	$= 250\,\mathrm{V}$		
Transfer Field 2 (E_{T2})	$= (U_{2,\ \mathrm{bot}} - U_{3,\ \mathrm{top}})\,/0.2\mathrm{cm}$			$=2.0\,\mathrm{kV\,cm^{-1}}$
$U_{\mathrm{GEM\ 3,top}}$			$=1430\,\mathrm{V}$	
$\Delta U_{\mathrm{GEM\ 3}}$	$= U_{3,\mathrm{top}} - U_{3,\mathrm{bot}}$	$= 270\,\mathrm{V}$		
Transfer Field 3 (E_{T3})	$= (U_{3,\ \mathrm{bot}} - U_{4,\ \mathrm{top}})\,/0.2\mathrm{cm}$			$=0.1\,\mathrm{kV\,cm^{-1}}$
$U_{\mathrm{GEM\ 4,top}}$			$=1140\,\mathrm{V}$	
$\Delta U_{\mathrm{GEM\ 4}}$	$= U_{4,\mathrm{top}} - U_{4,\mathrm{bot}}$	$= 340\,\mathrm{V}$		
Induction Field (E_{ind})	$= U_{4,\mathrm{bot}}/0.2\mathrm{cm}$			$=4.0\,\mathrm{kV\,cm^{-1}}$

Table 3.3: Typical high voltage settings for $IB < 1\%$ in a quadrupole GEM in Ne-CO_2-N_2 (90-10-5) at an effective gain of $2 \cdot 10^3$ [33]. Note the high transfer field in the 1st and 2nd gap, whereas E_{T3} is very low. The potentials at the top of the 4 GEM foils are given as well.

3.2.1 GEM production

The production of the GEM foils takes place at CERN. The raw material is copper-clad polyimide. Following a photo-lithographic process, a mask with a hexagonal hole pattern is applied to one side of the GEM [50]. The other side is completely covered. The layer protects the copper surface in the following electro-chemical etching process. This single mask production results in slightly non-symmetric double-conical GEM holes. The foils are produced in the four desired sizes and distributed among the QA centers (Helsinki and Bukarest). Quality assurance including the measurement of leakage current, hole size distribution, and gain uniformity is conducted before forwarding the foils to the framing sites in Munich (TUM), Bonn (Universität Bonn), and GSI. Figure 3.14 shows typical GEM defects. The first GEM has a row of holes with increased diameter. This leads to local gain variations and does not necessarily lead to the rejection of the foil. As long as the QA criterion of gain uniformity is met, the foil can be used. However, the second GEM is destroyed. The over-etched hole leads to significant non-uniformities in the of the electric field resulting in a high discharge probability. Additionally, the loose piece of copper is very likely to create a short between the GEM electrodes.

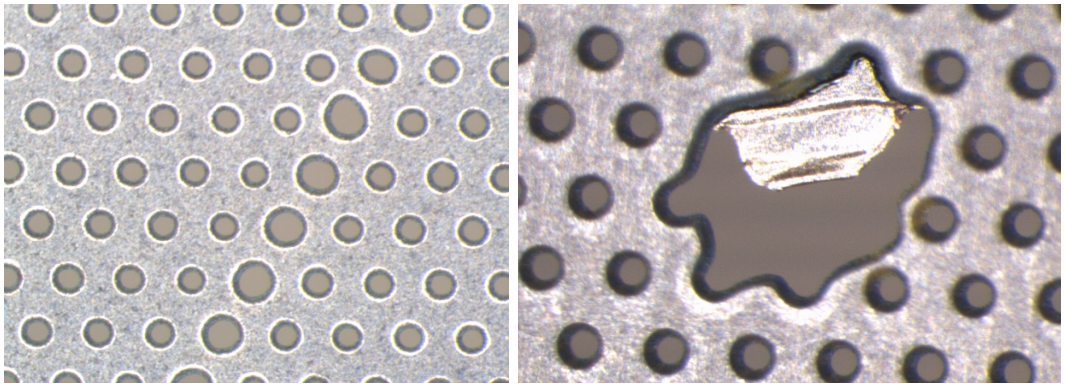

Figure 3.14: Microscope photographs of GEM defects. A row of holes has an increased diameter (left) and the GEM has been over-etched (right) [47].

At the framing sites the GEM foils undergo a leakage current test in a dry nitrogen environment. Instabilities due to residual water content or dust are thus avoided. A voltage is applied between the bottom side and every HV segment on the top side of the GEM individually. The voltage is ramped up to 500 V and kept in this state for 5 h. The leakage current is observed on every segment simultaneously. If the mean value of the leakage current during the second half of the measurement is below 167 pA in every segment, it is considered as good and will be further processed. All these actions have to be conducted in a clean room to keep the foils from collecting dust particles. Such particles could potentially lead to discharges ultimately harming the GEM. Additionally the GEMs have to be handled with great care due to their fragility. The thin foil can easily rip upon mechanical stress. After gluing, the foils are sent to the assembly centers where the ROCs are assembled.

3.2.2 Read Out Chamber assembly

Before assembling the chamber, the GEMs are again checked for leakage current. Then the GEM stack is put together, cables are soldered to the HV connections and together with the pad plane it is screwed to the Alubody via the mounting holes. The soldering requires great accuracy because the soldering material can introduce field distortions when not uniformly applied. To further shield the junction and assure the connection it is covered with glue.

4 Test beam at the CERN Proton Synchrotron

The performance of the GEM-based readout chambers and the new front-end electronics needs to be validated prior to operation in RUN 3. Therefore, a dedicated test beam is conducted at the CERN Proton Synchrotron (PS) [51]. One of the IROCs of the pre-production stage is mounted in a gas-tight test box. The box contains a cathode and a field cage to provide a homogeneous drift field. Ne-CO_2-N_2 in a mixture of 90-10-5 is used as gas medium since it will also be employed in the ALICE TPC. The distance between the cathode and the uppermost GEM is roughly 10 cm, which defines the maximum drift length. It should be noted that this is very short compared to the 2.5 m in the ALICE TPC. The box is shown in Fig. 4.1. On the upper side of the box the front-end cards (FEC) (green) and grounding cards (yellow) are mounted. The latter serve to define the potential on the unused parts of the pad plane. On the front the entry window of the chamber allows for measurements with beams and radioactive sources.

This test box is transferred to the East Hall of the Proton Synchrotron at CERN. The PS accelerates protons and is one of the pre-accelerators of the LHC. Additionally, secondary beams are provided for e.g. detector development. These beams are created by inelastic collisions of the primary beam on a fixed target. In these collisions mainly pions and electrons are created, where the exact admixture depends on the target material. These secondary particles can then be used to test the particle identification performance of the IROC. Additionally to the target material, the beam content also depends on the beam momentum, which can be selected via bending magnets within a range from 1 to 7 GeV c^{-1}. The measurements with the IROC are performed at 1, 2, 3, 4, and 5 GeV c^{-1}. The electron fraction in the secondary beam ranges from 60 % at 1 GeV c^{-1}, 7 % at 2 GeV c^{-1} to 0.5 % at 5 GeV c^{-1}. Due to the lack of electrons at momenta above 2 GeV c^{-1} beam only the 1 and 2 GeV c^{-1} data are considered in this work.

The goal of the test beam is to

1. validate the performance of the pre-production readout chamber,
2. perform first real data taking with the new front-end electronics,
3. perform first data analysis with the new software framework O^2,
4. and test the performance of two different powering schemes for the GEM stack with different HV settings.

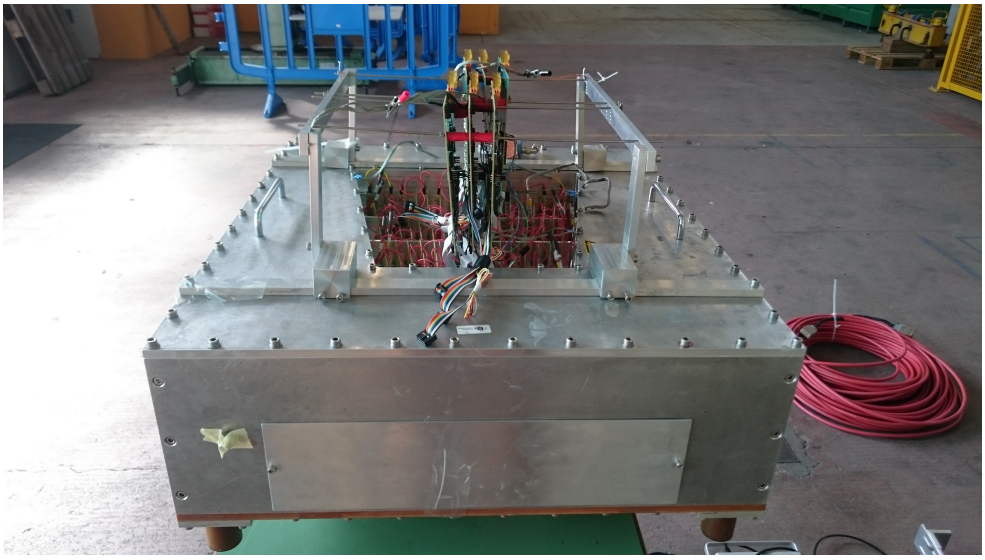

Figure 4.1: Photography of the test box with fully mounted front-end electronics in the East Hall of the Proton Synchrotron at CERN.

Figure 4.2: Close view of the connections to the readout anode. The front-end cards (green) with SAMPA chips are connected to a sub-set of the pad plane of the IROC. Grounding cards (yellow) define the potential of the remaining part of the pad plane.

4.1 Experimental setup

The detector is placed at the end of the T10 beam line together with a threshold Cherenkov Counter and two scintillators and arranged as shown in Fig. 4.3. The Cherenkov Counter is filled with N_2 at atmospheric pressure and detects Cherenkov light of traversing particles with a UV-sensitive photo-multiplier tube. The pressure of the gas can be adjusted such that Cherenkov photons are only produced for a specific particle type. Therefore, the signal of this detector can be used as a reference PID. The scintillators mounted in front of the entrance window of the IROC are used as a trigger requiring a coincident signal in both of them. The test box is positioned in a way that the beam traverses the IROC parallel to the pad plane with an average drift length of $\approx 5\,\text{cm}$. Figure 4.4 is a photo of the experimental setup.

The IROC is equipped with six front-end cards. The negative signal polarity and the requirements of the continuous operation demanded for a complete re-design of the electronics. The main part of the new FECs is the SAMPA chip [52], which is responsible for amplification, shaping, sampling, and digitization of the raw signal. For the test beam campaign only six FECs were available allowing for the equipment of 960 pads. This corresponds to about 20 % of the total pad plane of the IROC. The significantly enhanced data rates in RUN 3 require that the sampling frequency is reduced from 20 MHz to 5 MHz. The chips applied on the FECs can be seen on the upper part in Fig. 4.2.

A stable and reliable power supply is crucial for safe GEM operation since fluctuations in the individual GEM voltages can lead to harmful discharges. In addition, a stable powering of the GEM stack is fundamental for stable gain. By powering the GEMs with individual channels one would introduce a risk. In case of a single channel trip, which shuts down the channel, there is a time delay on the order of μs before all other channels trip. During this time the fields within the GEM stack can lead to further discharges and harm the GEM. To avoid this two types of power supplies powering the GEM stack via a single channel are tested. A resistor chain and a cascaded power supply which was developed specifically for powering GEM-based detectors. In case of a discharge and an ensuing trip of the channel, all voltages across the GEM stack go down simultaneously. The main difference between the two power supplies is their flexibility. In a resistor chain, the voltages applied to the GEMs are defined by the resistors in the chain. A voltage is applied to the chain, which degrades sequentially throughout the resistors, providing the powering for the GEMs. This fixes the ratios of the voltages applied to the GEM, which can only be changed by exchanging resistors in the chain. In a cascaded power supply the voltages can be set individually.

During the test beam campaign two different areas of the pad plane are equipped with the FECs as shown in Fig. 4.5. First, configuration 1 is used, where a segment in GEM 3 is not properly connected to the HV. This results in lower gain in row 57 - 63. For later runs configuration 2 is used to test the tracking (see Sec. 4.3) performance. Therefore, it is tilted by 5° with respect to the beam axis.

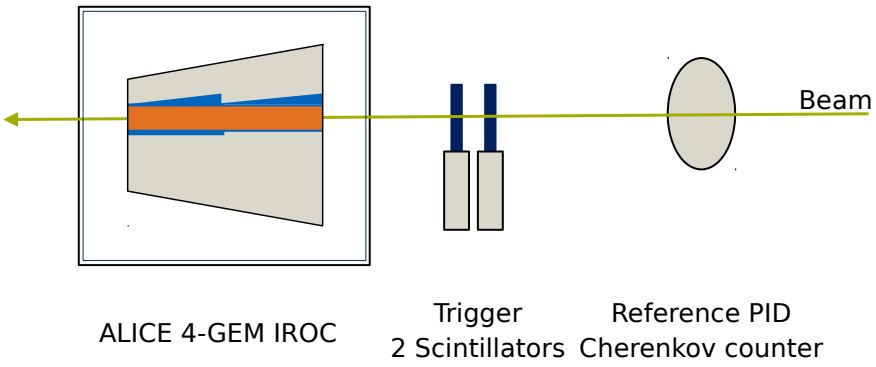

Figure 4.3: Sketch of the experimental setup, including the IROC, scintillators, and Cherenkov counter. The beam traverses the experiment from right to left.

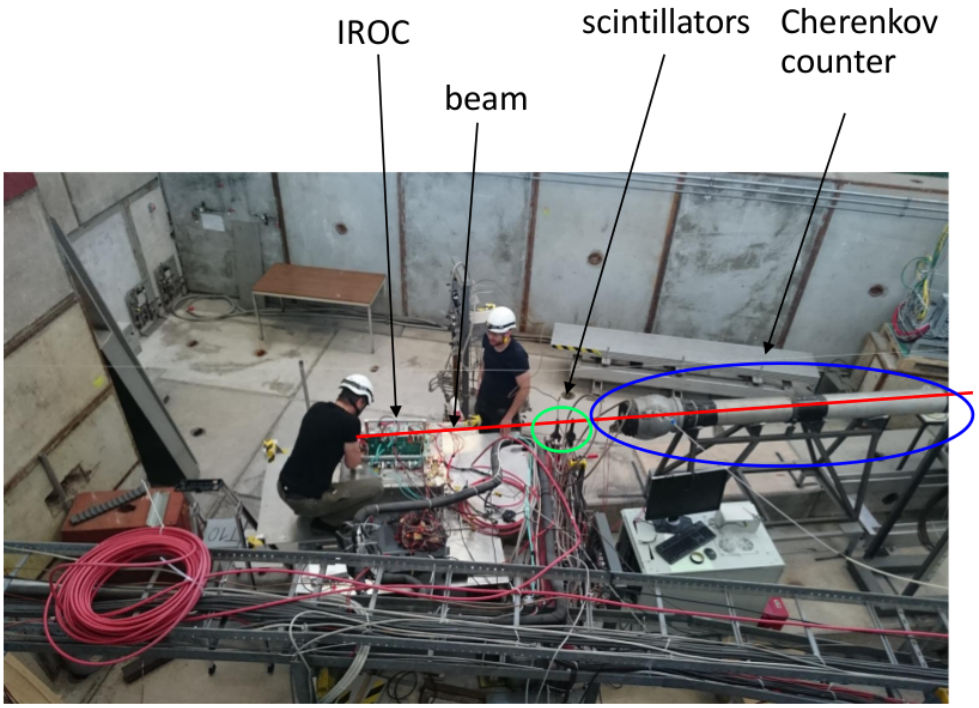

Figure 4.4: Photography of the experimental setup. The Cherenkov Counter is on the right side, the scintillators in the middle, and the test box with the IROC on the left.

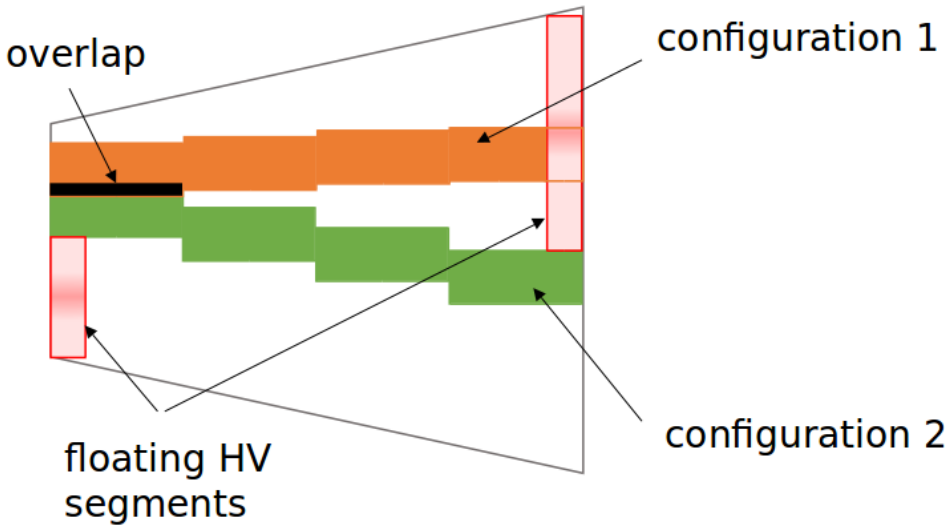

Figure 4.5: Schematic view of the two FEC configurations used during the test beam campaign.

4.2 Data acquisition

The electrons transferred from the amplification stage to the readout stage induce a signal on the pad plane. The shaper contained in the SAMPA chip folds the signal with the transfer function of the FECs (see Fig. 4.6) spreading the signal in time direction. The function is characterized by the peaking time of the shaper, which is 160 ns. The resulting signal is then sampled by the SAMPA.

In the newly designed readout scheme the Common Readout Unit (CRU) [53] is the junction between on-detector systems and the computing system. At the time of the test beam no CRU prototype was available. Instead, a triggered readout receiver card is used. Therefore, the readout is done semi-continuously where the data is recorded in time slices of ≈5 µs upon a trigger signal from the scintillators. With a 5 MHz readout rate this makes for 25 time bins per trigger which have a width of 200 ns each. The data is stored in a specific order. Pad for pad the signals are ordered chronologically, i.e. all signals on the first pad then all signals on the second pad etc.

The raw data is then further processed to convert the signals to so called digits. From the deliberate ordering of the raw signals, information on the position on the pad plane and the time bin can be extracted. In addition, also the measured signal, which is proportional to the deposited charge, is assigned to digits.

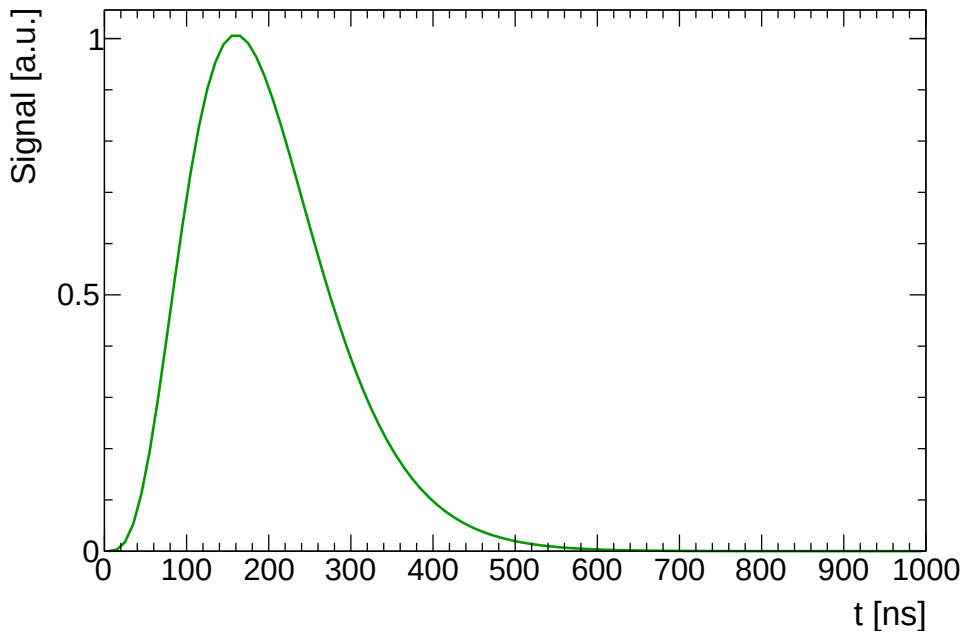

Figure 4.6: Transfer function of the SAMPA.

Dedicated pedestal runs are conducted without the presence of a beam to correct for noise and a constant offset due to capacitive coupling between the pads and bias from the low voltage supply of the FEE in the individual electronic channels. Figure 4.7 shows the pedestal and noise distributions for an exemplary run in FEC configuration 2. The pedestal value is obtained by fitting a Gaussian distribution to the measured signal for every individual channel. The mean value of the fit is identified to be the pedestal value, which is a constant offset that is subtracted from the signals before data analysis. The width of the fit is the noise, which is distributed around one ADC channel. This fits well within the specifications [33].

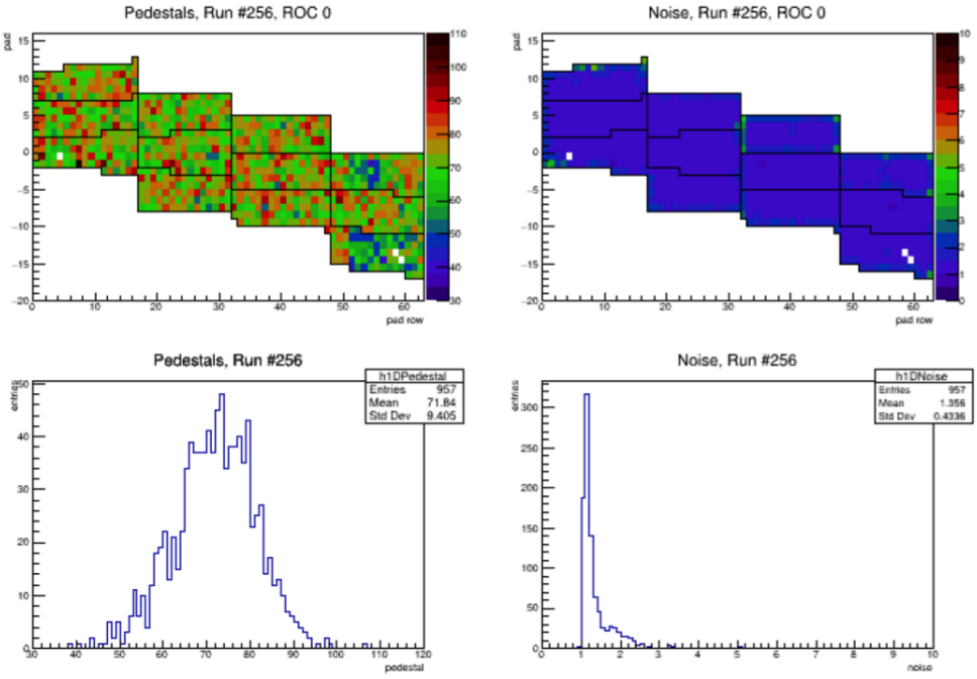

Figure 4.7: Pedestal (left) and noise distribution (right) for an exemplary run in FEC configuration 2 [54]. The top panel shows the values for every pad individually and the bottom panel shows the distributions.

4.3 Track reconstruction

The next step in data processing is the clustering of the digits. By combining digits to clusters, the computing time in the tracking process is significantly decreased. At the beginning of the clustering process, the signals are filled into in matrix in the pad-time plane. For every consecutive row on the pad plane the cluster finder looks for maxima in this matrix. Around these maxima, all signals A in a 5×5 matrix in time and pad direction are investigated. Q_{tot} is first calculated by

$$Q_{\mathrm{tot}} = \sum_{i=-1}^{i=1} \sum_{j=-1}^{j=1} A_{i,j}, \tag{4.1}$$

where the maximum cluster charge $Q_{\mathrm{max}} = A_{0,0}$. To reduce the influence of electronic noise, the charges at $|i| = 2$ and $|j| = 2$ are only added to Q_{tot} if the charge in the corresponding neighboring row is above threshold, which is 4 ADC counts. The position of the cluster is determined via a weighted mean weighting the position of the signals with their amplitude.

In general, the knowledge of the particle track is crucial for the determination of the momentum. Therefore, a precise tracking is essential. For tracking the ALICE HLT algorithm is used [55]. The tracking starts in the center row of the IROC looking for clusters in the neighboring rows. A first fit to those clusters is called track seed. Track seeds include only three clusters at the start of the tracking process. Then the seed is extended with trying to find a best fit to the clusters closest to the tails of the track seed. When the best fit is found the clusters are added to the track and the procedure is repeated until the edge of the readout area is reached.

5 TPC simulation in O^2

The enhanced interaction rate of RUN 3 and the continuous readout require a re-design of the computing framework of ALICE [18]. Therefore, the subdivision into online part, dealing with the data taking, and the offline part, responsible for the calibration and reconstruction will be dissolved and only one framework will take care of both parts - the O^2 framework [19].

The large occupancy of heavy-ion collision is a challenge for the detector design, operation, but also for the reconstruction and simulation algorithms. In particular, while the readout can be upgraded to cope with a two orders of magnitude larger interaction rate, the amount of available CPUs for reconstruction and simulation is not expected to be increased accordingly. Hence, the performance of the corresponding algorithms is of utmost priority.

A typical Monte Carlo (MC) simulation in high energy physics consists of multiple steps. First, the initial state of the collision is simulated using so-called event generators, such as Pythia [56, 57], EPOS [58], or Hijing [59]. The resulting particles are then transported through the detector medium, simulating multiple scattering and energy loss. This step is typically conducted with GEANT 3/4 [60, 61]. Then, the signal formation in the respective detectors is conducted. For the ALICE TPC, this step includes the simulation of the particle drift and diffusion. The ionization electrons are then amplified in the GEM stack and the resulting avalanche is folded with the response of the readout electronics.

The simulation of the energy loss is based on a modified version of GEANT 3 and 4, respectively, and described e.g. in [62]. In order to minimize the computing effort, the distance between two successive ionizing collisions of the incident particle with the detector medium is sampled around $2 \pm 0.5\,\mathrm{mm}$, which is a compromise between the resulting precision, and efficiency. At each step, a random energy loss according to a power law is assigned [25]. For energy transfers larger than $10\,\mathrm{keV}$, a δ-electron is produced.

When the primary electron has sufficient kinetic energy, it can further ionize the detector gas. The total number of electrons is then given by

$$N_{\mathrm{electrons}} = \frac{E_{\mathrm{prim}} - I_0}{W_i} + 1, \tag{5.1}$$

where E_{prim} is the energy of the primary electron, W_i is the effective ionization potential and I_0 is the first ionization potential. The distribution of the total number of ionization electrons per cm released by a $2\,\mathrm{GeV}\,c^{-1}$ pion is shown in Fig. 5.1. As expected, the distribution approaches a straggling function.

During the particle drift towards the ROCs, the charge cloud spreads due do diffusion, which is simulated by smearing the point-like electron cluster with a Gaussian distribution with a width given by

$$\sigma_{\mathrm{T,\,L}} = D_{\mathrm{T,\,L}} \cdot \sqrt{L_{\mathrm{drift}}}, \tag{5.2}$$

where D_{T} and D_{L} are the the corresponding diffusion coefficients and L_{drift} the drift length. Residual electronegative gases, such as Oxygen, as impurities in the active detector medium can lead to the absorption of electrons. This is considered by randomly removing electrons based on the corresponding drift time and absorption probabilities.

At the amplification stage, each electron is multiplied by the applied gain. The resulting avalanche is a convolution of single-electron avalanches. Random fluctuations of the gain are considered by sampling from a Polya distribution, which describes the single-electron amplification in GEM-based detectors [43]. The pad response is assumed to be purely projective, i.e. the signal is induced only on the pad directly under the arrival position of the electron cloud. The time signal is obtained by folding the electron avalanche with a so-called Gamma4 function,

$$S(t) = \mathcal{N} \cdot Q \cdot e^{-4\frac{t-t_0}{t_{\mathrm{peak}}}} \cdot \left(\frac{t-t_0}{t_{\mathrm{peak}}}\right)^4, \tag{5.3}$$

where $\mathcal{N}$ is employed to normalize the function and equal to 55. Q corresponds to the avalanche charge, t_0 to the arrival time of the electrons and t_{peak} to the peaking time of the shaper. The resulting signal is then digitized employing the given dynamic range of the electronics. Noise and pedestal are taken into account using results based on measurements with fully equipped ROCs.

The parameters used to steer the simulation are summarized in Tab. 5.1. The simulated events are then reconstructed in the same manner as described in Sec. 4.3.

Table 5.1: Gas properties, readout and electronics parameters used in the simulation.

Parameter	**Unit**	**Value**
First Ionization potential I_0	[eV]	20.77
Effective ionization potential W_i	[eV]	37.3
Drift velocity at 400 V/cm	[cm/µs]	2.58
Longitudinal diffusion constant D_{L}	[µm/$\sqrt{\mathrm{cm}}$]	221
Transverse diffusion constant D_{T}	[µm/$\sqrt{\mathrm{cm}}$]	209
Oxygen content	[ppm]	5
Shaper peaking time t_{peak}	[ns]	160
Dynamic range	[V]	2.2
Conversion gain	[mV/fC]	20
Sampling frequency	[MHz]	5

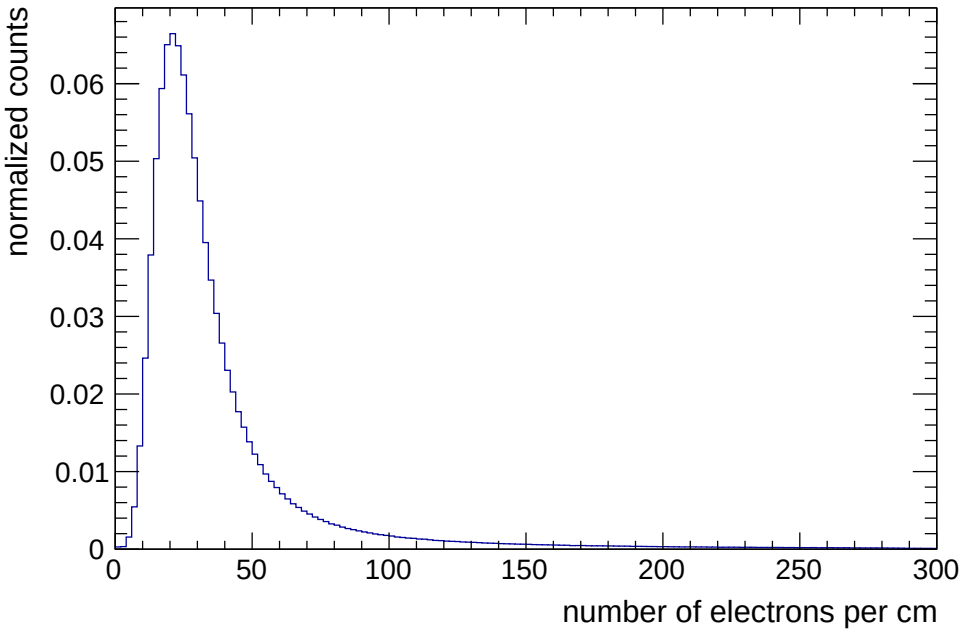

Figure 5.1: Distribution of the total number of electrons per cm track of a 2 GeV c^{-1} pion.

6 Results

6.1 Test beam data analysis

The goal of the test beam campaign is to validate the performance of a GEM-based readout chamber from the pre-production phase of the ALICE TPC Upgrade.

As mentioned in Sec. 4.1, a Cherenkov counter is used for reference PID. In Fig. 6.1 the data for the exemplary run is shown. If the signal is below 0.009 the particle is identified as a pion and if the signal is above 0.011 it is identified as an electron. Between those two values there is a small overlap region. Events with a Cherenkov signal in this region are not used for the analysis to maintain a reliable reference PID.

The first step of the data analysis is the assurance of the integrity of the data. Therefore, a few quality checks of the recorded tracks and events are conducted. Figure 6.2 shows the number of clusters assigned to the tracks of an exemplary run in the second FEC configuration. With the IROC having 63 pad rows, one expects 63 clusters at maximum. This is the ideal scenario in which a cluster is found in every row. Due to distortions of the drift field due to edge effects in the first and last pad row, a fraction of the cluster charge is lost. Therefore, the total charge is reduced and correspondingly is the efficiency to find clusters in these regions. In addition, the spacer grid between the GEMs leads to lower gain in pads in the affected pad rows. Accordingly, the obtained distribution is asymmetric with a peak around 60 and not more than 63 clusters per track, as expected. The distributions of the maximum and total cluster charge for an exemplary run is shown in Fig. 6.3. As expected, both approach a straggling function.

Figure 6.4 shows the cluster occupancy for all runs. In configuration 1 the floating GEM segment at the rightmost pad rows can be identified due to a lower occupancy. Less clusters can be found because of the low gain in this area.

The number of tracks that were found per event is shown in Fig. 6.5. Almost 60 % of the recorded events contain only one track as is intended with this setup. This is an important criterion since only in these cases the Cherenkov PID can be used reliably.

The selection criteria for the events and tracks are summarized in the following. First of all, all events with not exactly one track are removed to ensure that we can rely on the reference PID from the Cherenkov counter. More than one track per event would result

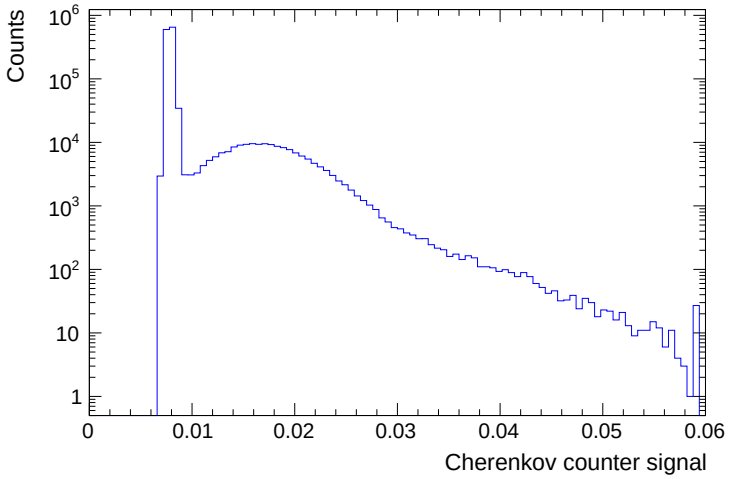

Figure 6.1: Signal distribution from the Cherenkov counter used as reference PID.

in ambiguities in the recorded data by the Cherenkov counter and the trigger particle. Next, we cut on the number of clusters per track. If a track has less than 47 clusters it is removed because the resolution of the mean energy loss of the corresponding diminishes with decreasing statistics. A further cut is conducted on the time stamp of the clusters. To ensure that the track in the event originates from the beam, we set a lower cut at 6 and an upper cut at 13 time bins. These values correspond to a range from $\approx 3\,\mathrm{cm}$ to $\approx 7\,\mathrm{cm}$. Finally, we cut on the cluster location on the pad plane. Since Q_{tot} consists of charges from neighboring pads it will be biased if the cluster is located at the edge of the readout region. In this case a fraction of the recorded cluster charge missing and hence Q_{tot} will be biased towards lower values. Therefore, a track is dismissed if more than 30 % of its clusters are within 3 pads from the edge of the readout region.

In addition, the cluster charges must be corrected for the inclination angle α of the particle trajectory. Tracks that are tilted in the pad row-pad plane lose more energy while traversing the IROC since the traveled distance scales with $\frac{1}{\cos\alpha}$. Hence, the cluster charge is biased towards higher values. The corrected cluster charge is $Q/\cos\alpha$.

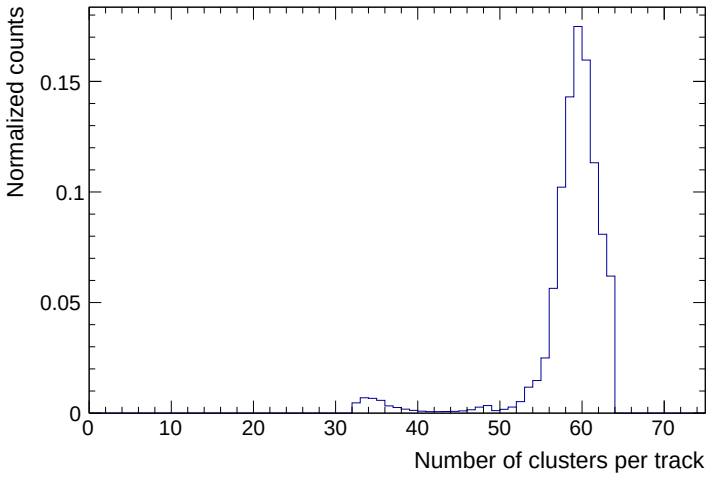

Figure 6.2: Normalized distribution of the number of clusters per track in all runs.

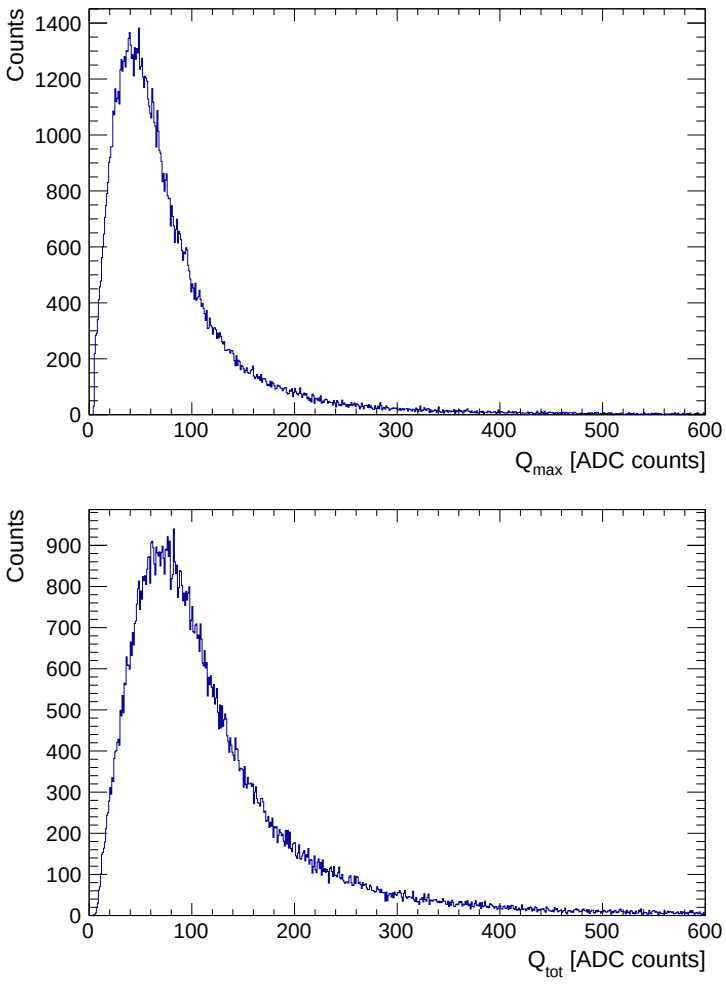

Figure 6.3: Distribution of the maximum (top) and total cluster charge (bottom) for an exemplary run.

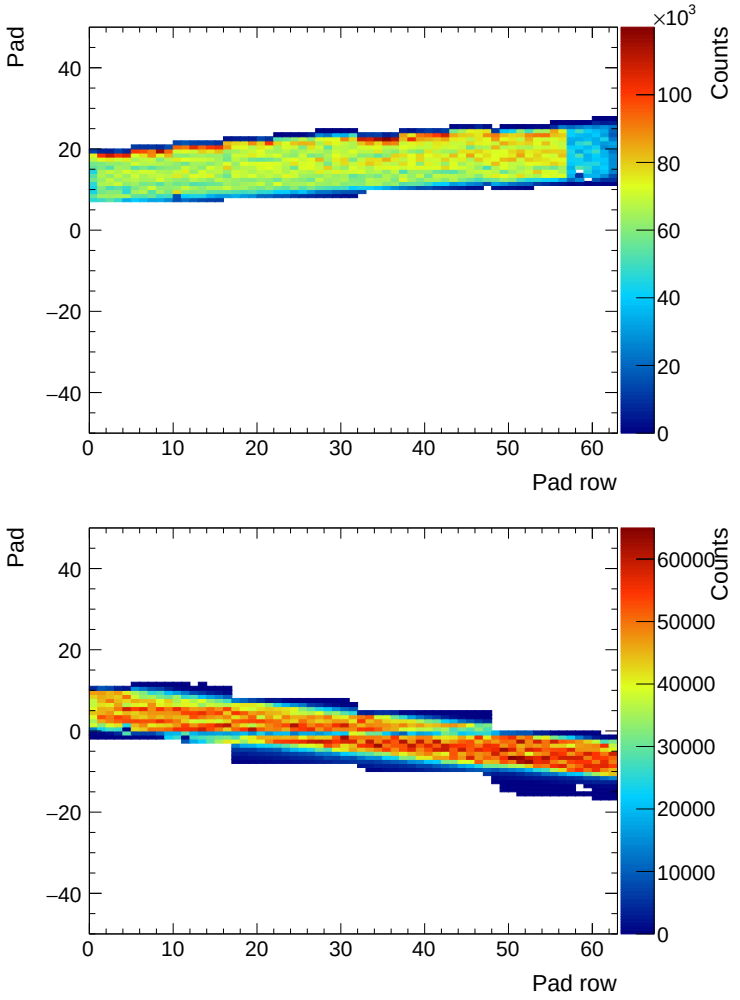

Figure 6.4: Occupancy of the readout area for all runs for FEC configuration 1 (top) and 2 (bottom).

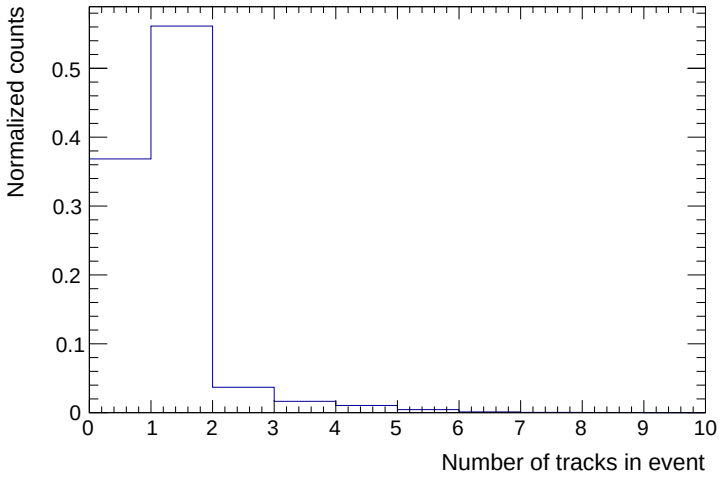

Figure 6.5: Normalized distribution of the number of tracks per event.

6.1.1 Gain uniformity studies

The gain uniformity is a crucial ingredient of the detector performance. In particular, local variations of the gain in the GEM-stack result in a reduced $\mathrm{d}E/\mathrm{d}x$ resolution and accordingly in a worsened PID performance. The requirement for the ALICE TPC with GEM readout are that these local variations need to be below 10 % to retain the current PID performance of the detector [33]. These gain variations originate from different phenomena. The main reason are local variations in hole size and density, both of which are related to non-uniformities in the production. Additionally, also the FECs have an influence on the gain uniformity. Channel-by-channel variations can for instance originate from a different noise performance related to the low voltage powering of the FECs. These variations need to be corrected for every channel, and every pad, individually.

To quantify and correct for this effect, these gain variations are evaluated on a pad-by-pad basis and stored in a so-called gain map. This map is obtained as follows. For every event, all cluster charges Q_{tot} are normalized by the mean energy loss of the corresponding track $\langle \mathrm{d}E/\mathrm{d}x \rangle$. This procedure assures that the resulting value is independent of the absolute gain and the particle species. The cumulative normalized cluster charge distribution for all events is then the straggling function of the energy loss, with a most probable value (MPV) at unity. The MPV of this distribution, extracted by truncation, is then used as the correction value. Figures 6.6 and 6.7 show the gain map for both FEC configurations. The two gain maps are shown separated due to the overlapping region between row 0 and 10. While the gain fluctuations in the GEM-stack are independent of the FEC configuration, the channel-by-channel variations in the FECs are not. During the testbeam, the channels connected to the affected region were not the same, and therefore the extraction of two different gain maps are required.

The horizontal region of low gain in Fig. 6.7 around pad column 0 is due to the horizontal part of the spacer grid of the GEM-stack. Accordingly, the overlap of the vertical spacer with pad rows 31 and 32 leads to the vertical structure in both gain maps. Additionally, the boundaries of the individual GEM HV segments can be observed, indicated by the regularly appearing pad rows with slightly lower normalized gain. In the upper part of the GEM-stack, the rightmost HV-segment of GEM 3 was due to a malfunction not connected to the HV distribution circuit and therefore left floating, as discussed in Sec. 4.1. Correspondingly, the gain in that region is significantly reduced, and in fact off-scale. Additionally, edge effects can be observed in both configurations originating from loss of the total cluster charge $\mathrm{Q_{tot}}$ as discussed above.

Figure 6.8 shows the resulting distributions of the normalized gain for both FEC configurations. In order to obtain an unbiased estimate of the local variations of the amplification, pads affected by edge effects, GEM segment boundaries or the spacer grid are not taken into account. As expected, the normalized gain is distributed around 1. With a width of (5.5 ± 0.2) % in the first and (6.6 ± 0.3) % the gain uniformity is well within the specifications, which require a gain spread smaller than 10 % [33].

In order to obtain an unbiased measurement of the charge deposit, the measured cluster

charges are corrected for using the gain map. The influence of the this correction on the data is shown in Figs. 6.9 and 6.10. In these plots the distribution of Q_{max} as a function of the pad row before and after the correction is shown. The maximal cluster charge Q_{max} directly scales with the gain and therefore it is an adequate observable for gain uniformity studies. Figure 6.9 displays Q_{max} as a function of the pad row before the correction and clearly reflects the features of the gain map. The difference in gain uniformity becomes especially apparent in pad row 31 and 32, which are affected by the spacer grid, and the edge effects at the beginning and end of the chamber. After the gain correction, shown in Fig. 6.10, the distribution is much more uniform. These results show that the gain map is working as intended.

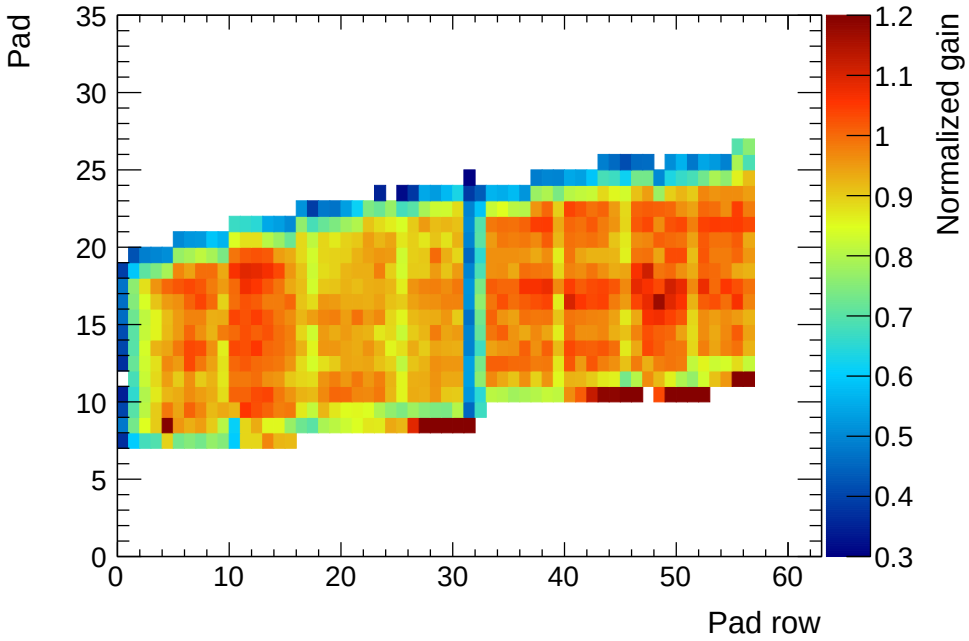

Figure 6.6: Two-dimensional gain map for FEC configuration 1. The region of low gain in the middle is due to the spacer grid of the GEM-stack, and the missing part on the right due to a malfunctioning, floating GEM HV segment.

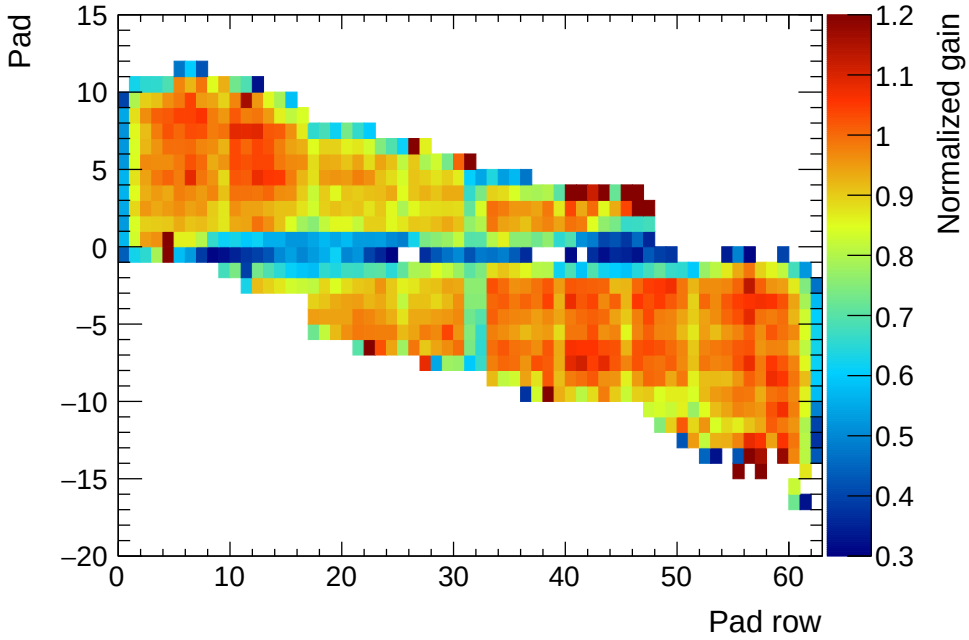

Figure 6.7: Two-dimensional gain map for the FEC configuration 2. The region of low gain in the middle is due to the spacer grid of the GEM-stack.

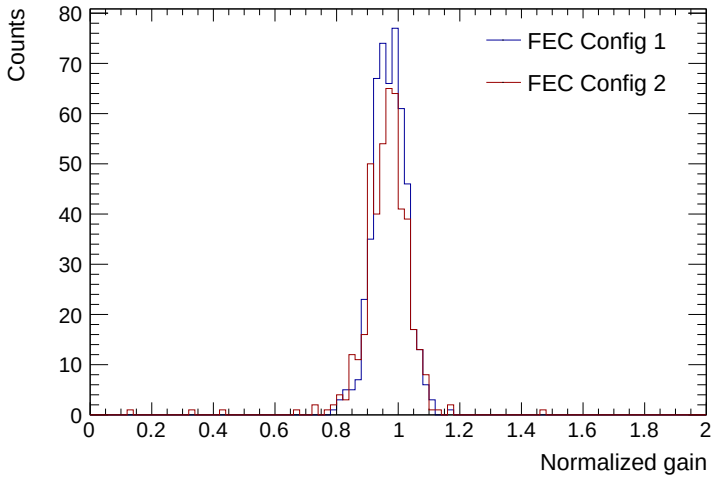

Figure 6.8: Normalized gain distributions for FEC configuration 1 (blue) and 2 (red). The edges, segment boundaries, and pads affected by the spacer grid are not taken into account.

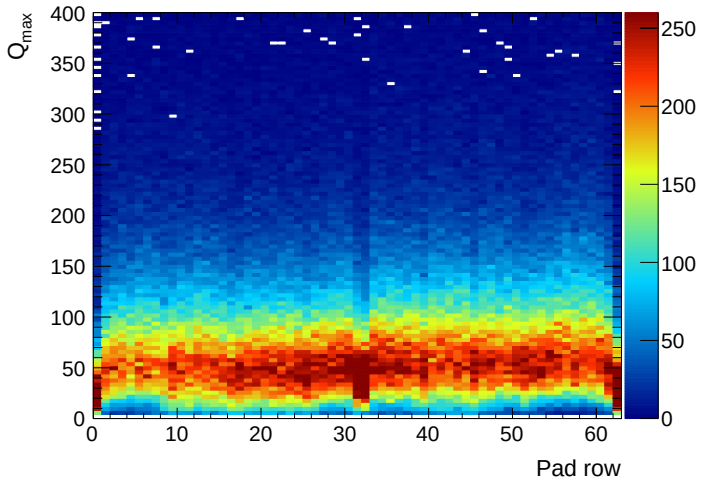

Figure 6.9: Q_{max} as a function of the pad row before applying the gain map correction. In particular large variations due to the spacer grid and edge effects are visible.

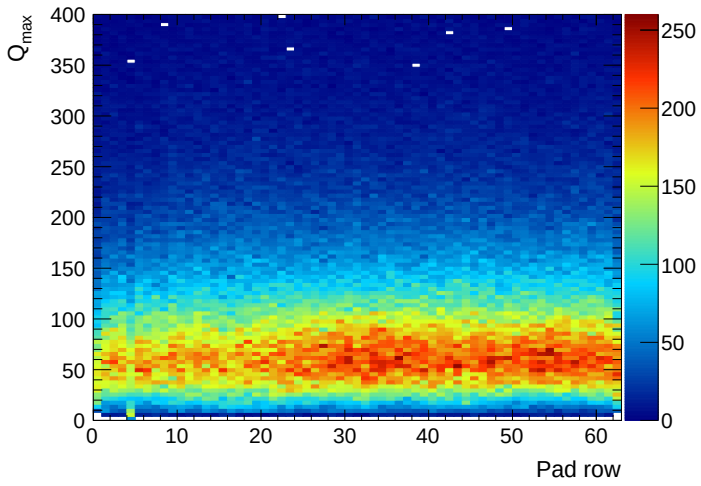

Figure 6.10: Q_{max} as a function of the pad row after applying the gain map correction. The gain is now uniform across the rows.

6.1.2 Separation power and dE/dx resolution

The resolution of the specific energy loss $\langle \mathrm{d}E/\mathrm{d}x \rangle$ is an indicator for the PID performance of the detector. Therefore, it is one of the figures of merit for this work.

Figure 6.11 shows the $\langle \mathrm{d}E/\mathrm{d}x \rangle_{\mathrm{trunc}}$ spectra obtained from the total cluster charges of pions (blue) and electrons (red) for an exemplary track. The resulting resolution is 11.9 % for pions and 10.7 % for electrons. The separation power is $3.65\,\sigma$, as introduced in Eq. 2.5.

These results indicate a worse PID performance than that obtained with an earlier prototype in 2014 [48, 63]. There, the resolutions for pions and electrons was measured to be 11.05 % and 9.99 % resulting in a separation power of $4.22\,\sigma$. The reason for the seemingly worse

results is the lower sampling rate. The measurements in 2014 were conducted with different readout electronics, which sampled the data with 20 MHz compared to the 5 MHz in the data under investigation. This effect will be further investigated in the following.

As mentioned earlier, ionization electrons undergo diffusion while drifting towards the GEM stack. This process spreads the electrons in time direction and leads to a spead over more time bins. The short drift in the test box does not allow for sufficient diffusion so that only narrow signals are sampled. Indeed from the diffusion during the 5 cm drift, a maximal spread in time direction of 19 ns is expected, which corresponds to 10 % of the width of a time bin. This results in the variations of Q_{max} as discussed in Sec. 6.2. It should be noted here, that the scenario of the test beam is not representative for the operation of the TPC. Then, particles are created in the interaction point region in the center of the detector, from which they traverse the TPC in all directions. Hence, it is highly unlikely to have a trajectory at such a small distance in parallel to the readout chamber.

Figure 6.12 displays the separation power as a function the beam momentum. As expected, the particles are better distinguishable at 1 GeV c^{-1} compared to 2 GeV c^{-1}. One can already see that in different Bethe-Bloch curves shown in Fig. 2.10.

The separation power as a function of ion back flow is shown in Fig. 6.13. The different values of the IBF correspond to different HV settings. The increasing IBF results from HV

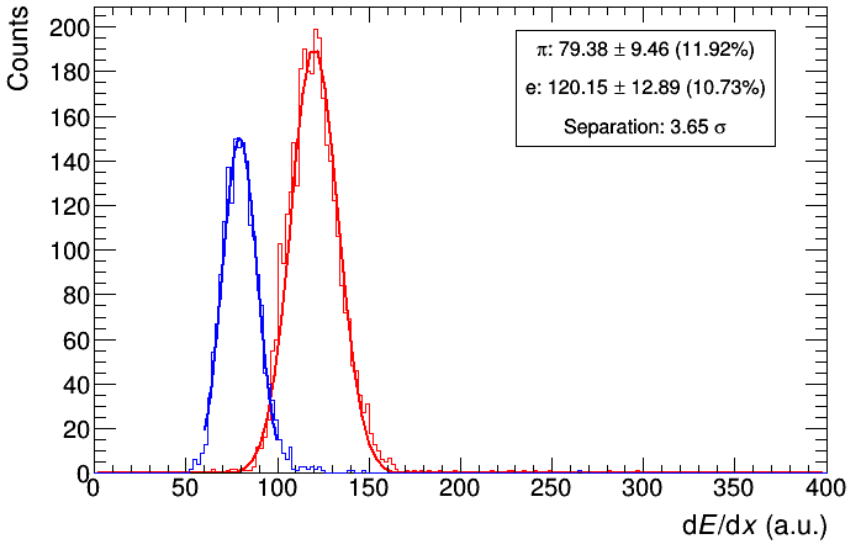

Figure 6.11: Mean energy loss distribution of an exemplary run at 1 GeV c^{-1}. Pions and electrons are shown in blue and red, respectively.

settings with more gain in GEM 1. With higher gain in the first GEM the influence of gain fluctuations reduces and a better $\mathrm{d}E/\mathrm{d}x$ resolution is obtained, resulting in a better separation. The same holds for the separation power as a function of the resolution obtained with an ^{55}Fe source. Higher gain in the first GEM results in a better ^{55}Fe resolution and also in a better separation power as can be observed in Fig. 6.14.

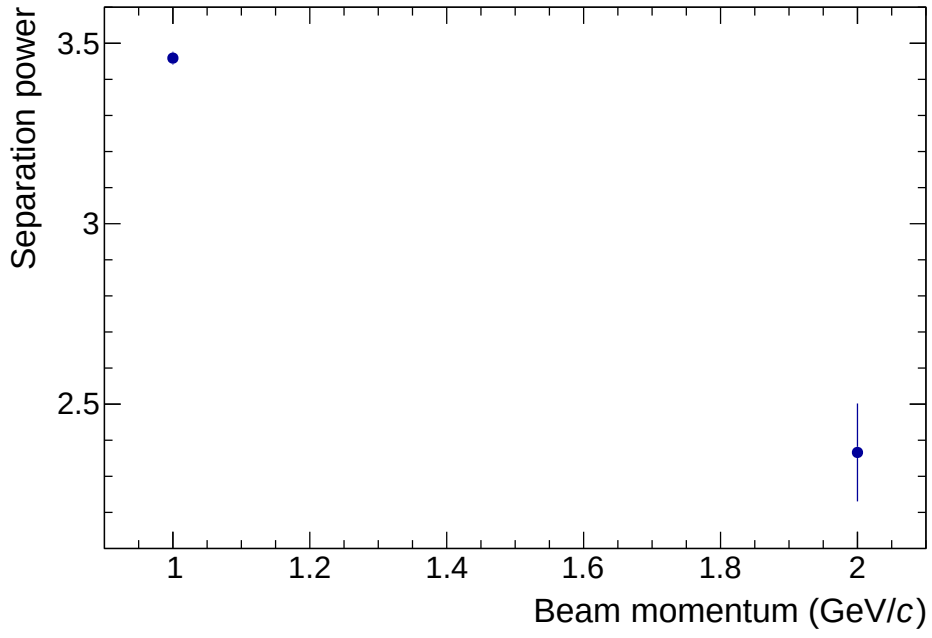

Figure 6.12: Separation power as a function of the beam momentum.

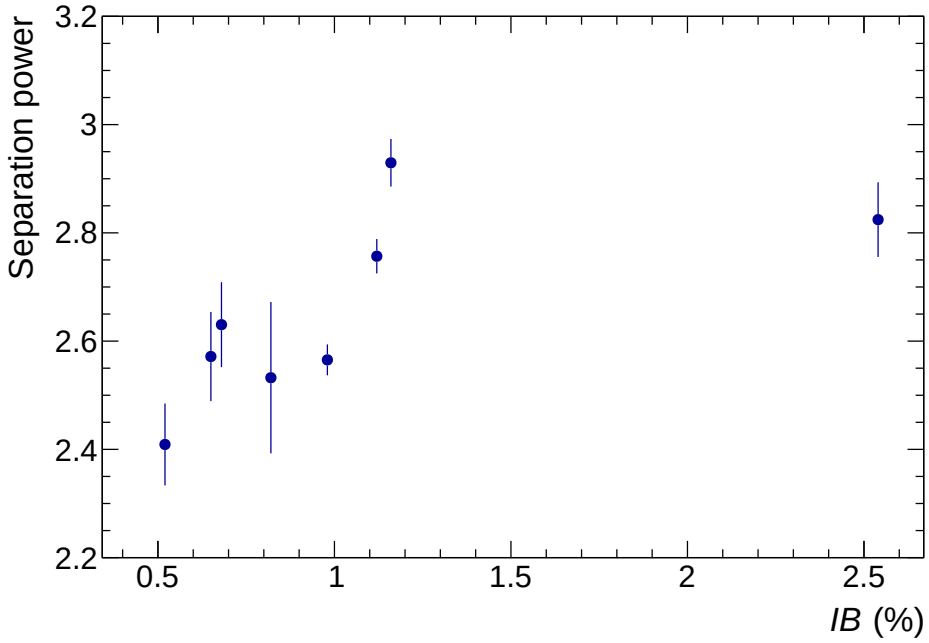

Figure 6.13: Separation power as a function of the ion back flow at 2 GeV c^{-1}.

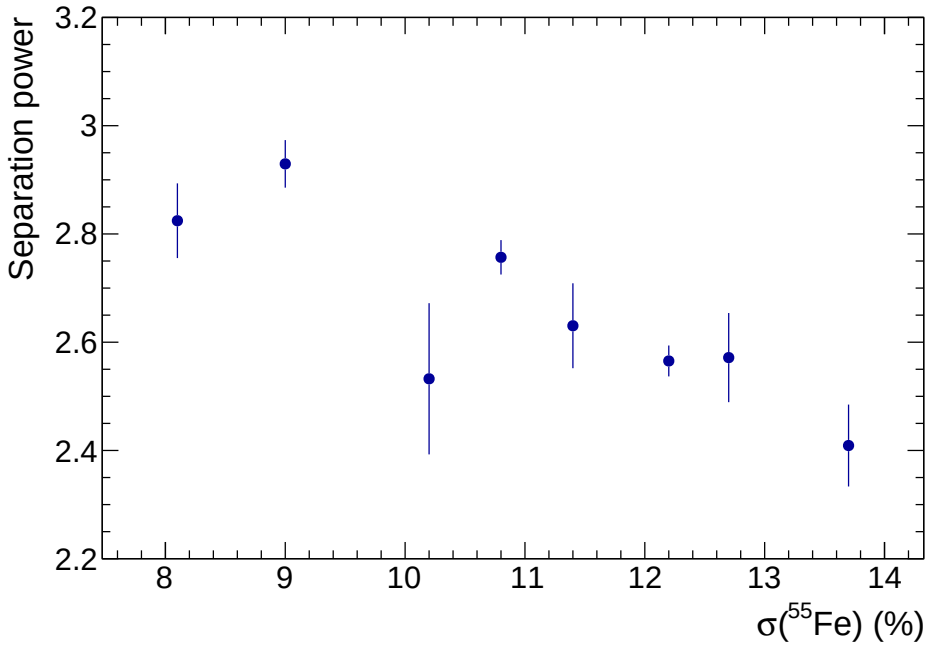

Figure 6.14: Separation power as a function of the ^{55}Fe resolution at 2 GeV c^{-1}.

6.2 Study of the influence of the sampling frequency on the detector response

The energy resolution results that were obtained from the test beam data are worse than the ones measured with an earlier prototype and different FECs [48, 63]. In particular, these FECs sampled the data with 20 MHz. To study the influence of the sampling frequency on the measured data, a toy Monte Carlo simulation is conducted folding the signal induced by an electron with the transfer function of the SAMPA (see Fig. 4.6). The input for the SAMPA response are the signal amplitude and the arrival time of the electron. In this test, the amplitude was sampled randomly from a Gaussian with a width of 10 % to mimic the energy resolution of a typical GEM-stack, and a flat distribution for the arrival time of the charge cloud with respect to the sampling clock. No spread of the charge cloud is chosen to simulate the short drift. The resulting signal is sampled at 8 points, to which the indices $N = 0,...,7$ are assigned, with 5 and 20 MHz.

Figures 6.15 and 6.16 show the distribution of the obtained signal Q as a function of the ADC sample for 1000000 electrons. Already here one can see a significant difference in the resulting distributions. With the slower sampling rate the signal is contained within only three samples while a smooth signal is obtained with the faster sampling leading to a much smaller spread in charge in each sample. The charge distributions Q of the maximum of the samples, which corresponds to Q_{max}, is shown in Figs. 6.17 and 6.18 for both sampling frequencies. Depending on the arrival time of the electron cloud with respect to the sampling clock, Q_{max} can occur in two different samples. Due to the coarse sampling of the transfer function at 5 MHz, there is a large spread in Q_{max}. This is not the case at 20 MHz because of the smoother evolution of the charges across neighboring samples. In the Q_{max} distributions in Fig. 6.19 and 6.20 the difference becomes apparent. At 5 MHz two overlapping Gaussian distributions arise. For the 20 MHz sampling this is not the case.

To obtain Q_{tot} a pseudo-clustering is conducted where

$$Q_{\mathrm{tot}} = \sum_{\mathrm{i}=N_{\mathrm{max}}-2}^{N_{\mathrm{max}}+2} Q_{\mathrm{i}}. \tag{6.1}$$

Figures 6.21 and 6.22 show the resulting Q_{tot} distributions. At 20 MHz the resulting distribution has a resolution of 10.5 % and reflects the resolution of the incoming charge cloud. At 5 MHz, however, a very broad distribution containing two Gaussian distributions is obtained. In the particle detector a broadening of the total cluster charge distribution leads to a decrease of the energy resolution. In conclusion, this test shows that that a short electron drift in combination with the 5 MHz sampling rate result in a significantly diminished energy resolution.

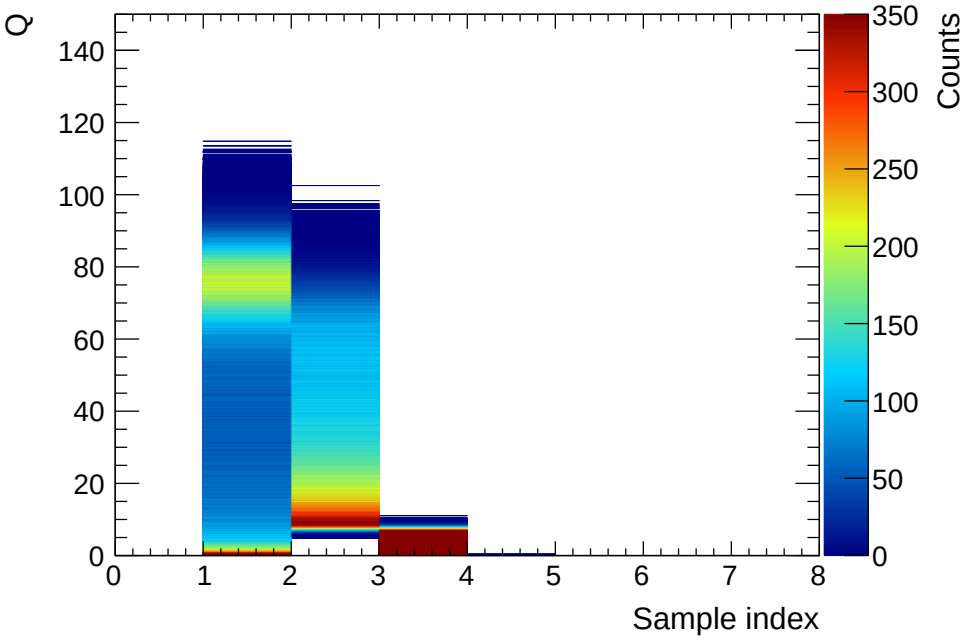

Figure 6.15: Signal distribution as a function of the sample index for the 5 MHz sampling. The transfer function is sampled at only three points.

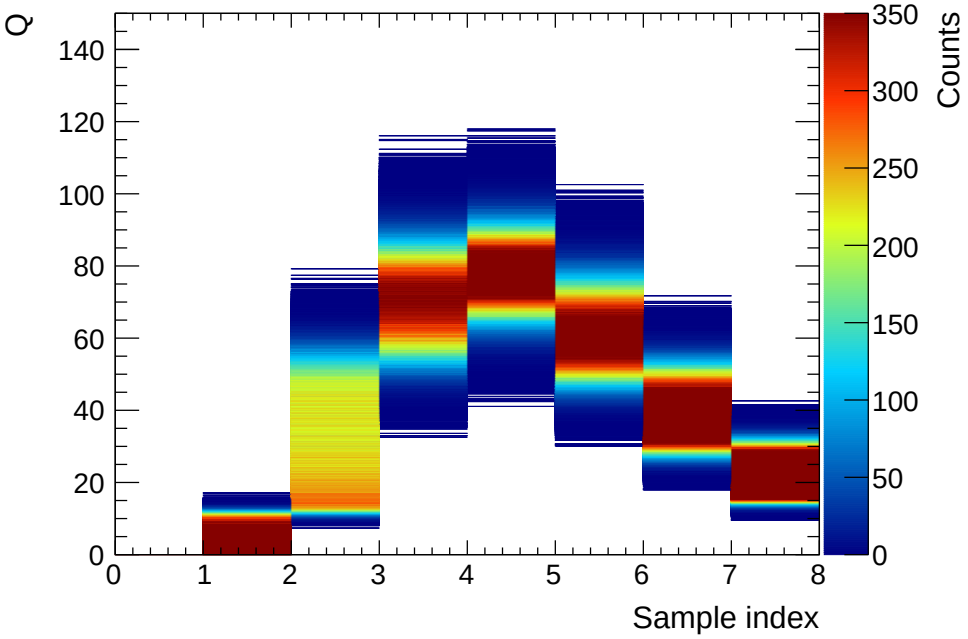

Figure 6.16: Signal distribution as a function of the sample index for the 20 MHz sampling. The transfer function is sampled smoothly.

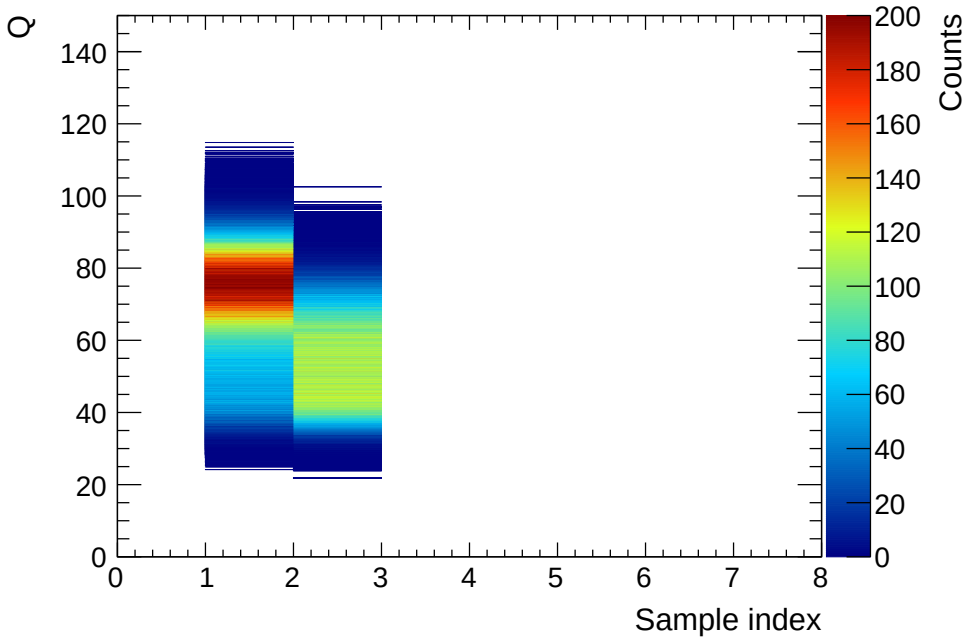

Figure 6.17: $Q_{\max}$ distribution as an function of the sample index with 5 MHz sampling. $Q_{\max}$ occurs at two sampling indices.

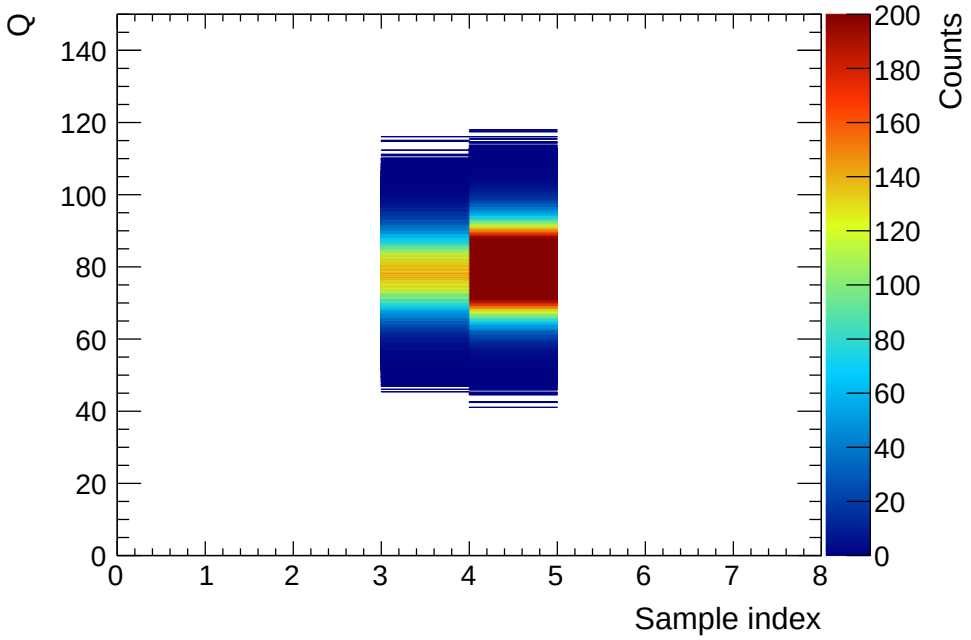

Figure 6.18: $Q_{\max}$ distribution as an function of the sample index with 20 MHz sampling. $Q_{\max}$ occurs at two sampling indices.

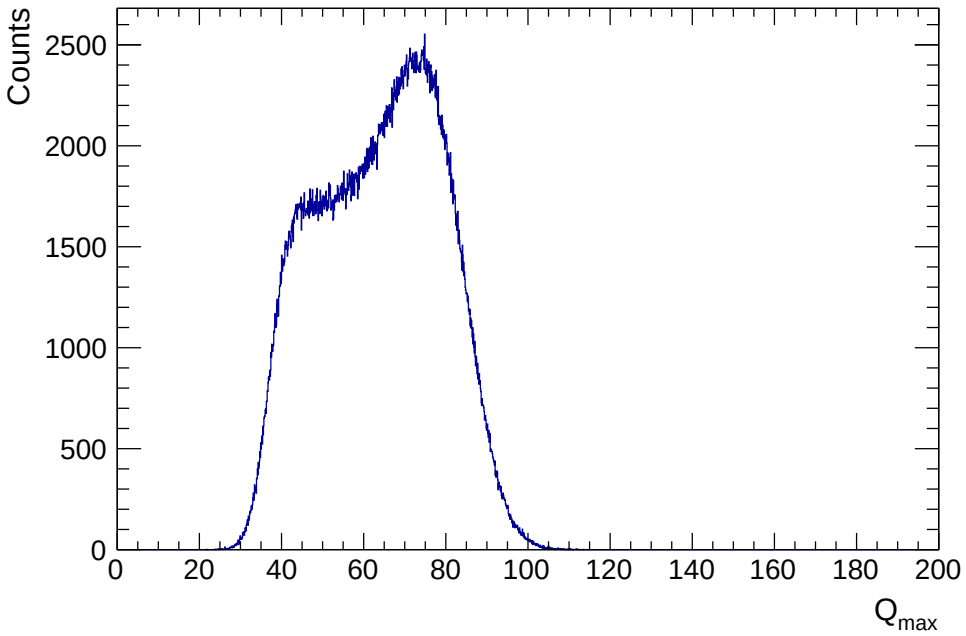

Figure 6.19: $Q_{\max}$ distribution with 5 MHz sampling. Two overlapping Gaussian distributions ensue.

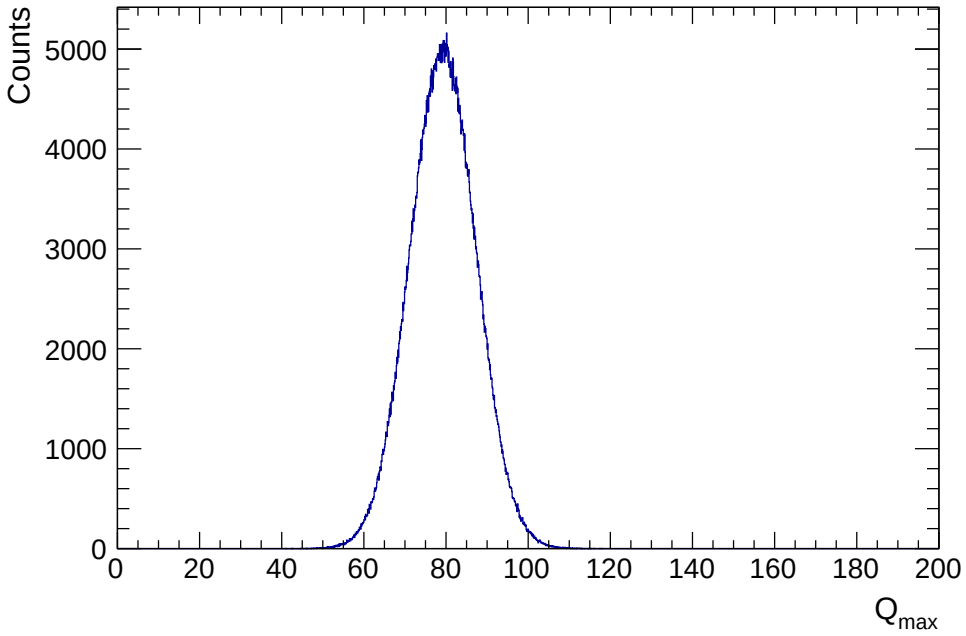

Figure 6.20: $Q_{\max}$ distribution with 20 MHz sampling. A Gaussian distribution ensues.

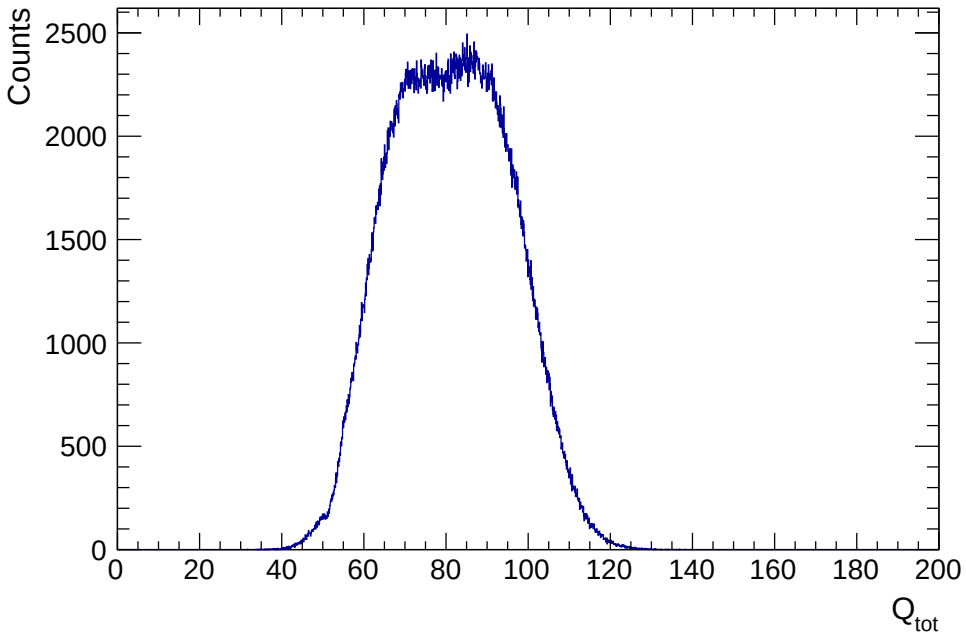

Figure 6.21: Q_{tot} distribution at 5 MHz sampling. Two overlapping Gaussian distributions ensue.

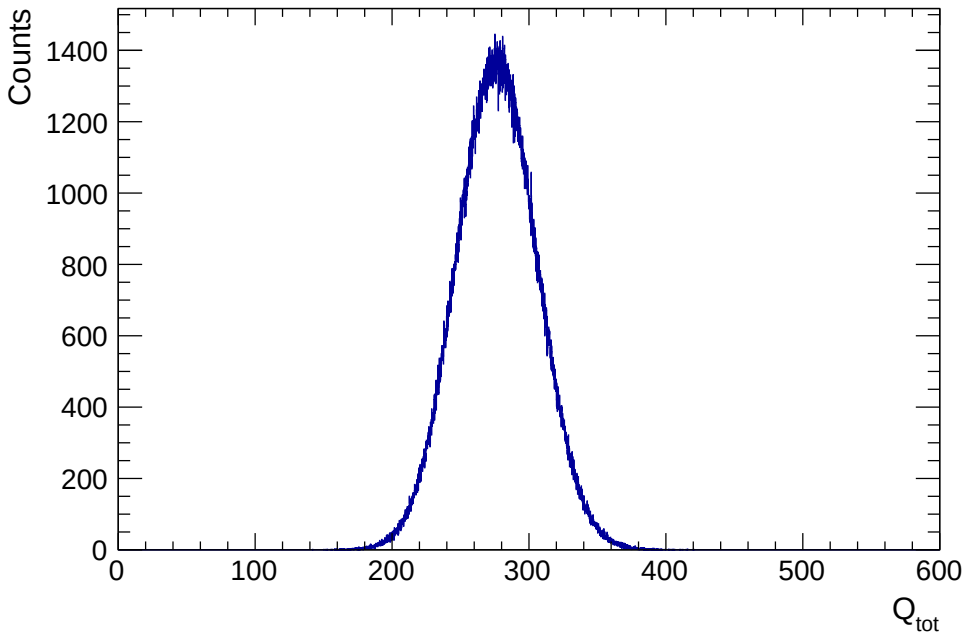

Figure 6.22: Q_{tot} distribution at 20 MHz sampling. A Gaussian distribution ensues

6.3 Simulation benchmarking

The test beam data is not only analyzed to test the performance of the new readout system but also to validate the TPC simulation implemented in O^2. By comparing the simulation output to the data, the full simulation chain from the energy loss of the incident particles, the signal creation and data reconstruction process in the simulation can be tuned and verified. A scenario similar to the test beam is simulated and representative observables are compared.

First of all, the cluster charge distributions are investigated. Figure 6.23 shows the $\mathrm{Q_{max}}$ distribution. The charge distributions give information on the core processes of the signal creation and track reconstruction, namely the diffusion, amplification, FEC response, clustering and tracking. Both distributions are well in agreement. The same holds for the $\mathrm{Q_{tot}}$ distribution in Fig. 6.24. However, for a final verification more observables have to be studied e.g. track residuals and cluster shape. The final figure of merit is the $\mathrm{d}E/\mathrm{d}x$ distribution, which defines the TPC performance. Figure 6.25 shows the comparison between the test beam data and the simulation for 2 GeV c^{-1} pions. The energy resolution in the test beam data is 11.4 % while a broader distribution with a resolution of 13.3 % is obtained from the simulation. To improve the results, more tuning and verification of the simulation has to be done. On one hand the GEM response needs fine tuning, and the reconstruction chain more verification. On the other hand, the FEC response possibly needs to be adjusted because the SAMPAs used in the test beam are from a pre-production series and it is therefore not clear if the peaking time of the transfer function is exactly 160 ns as in the recent models and the simulation. To obtain the peaking-time the time

structure of the digits in the test beam data can be investigated. A study involving more observables will allow to further verify and tune the simulations, based on the experimental results of this work.

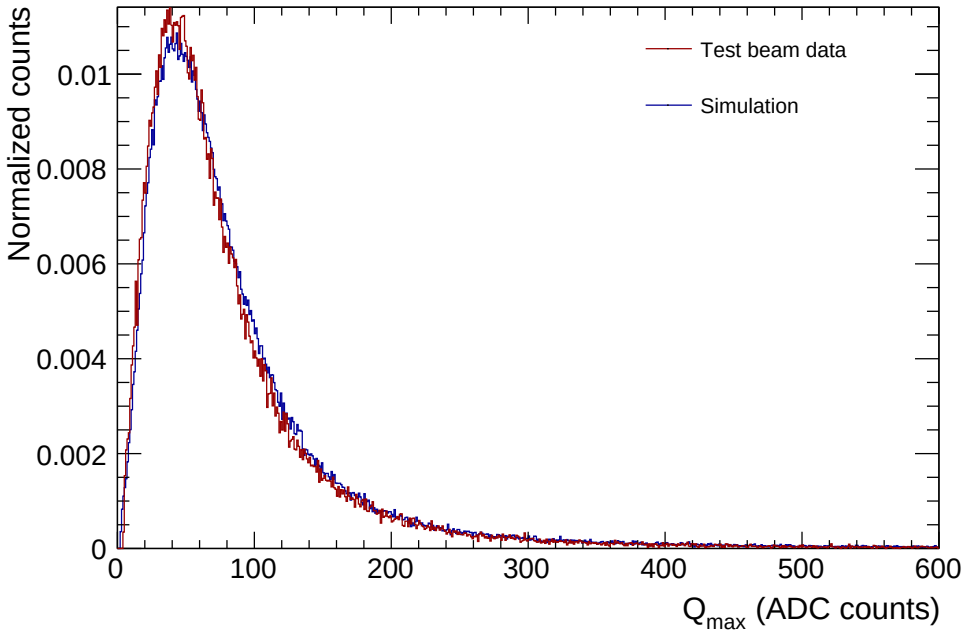

Figure 6.23: Q_{max} distribution for 2 GeV c^{-1}. Red: data, blue: simulation

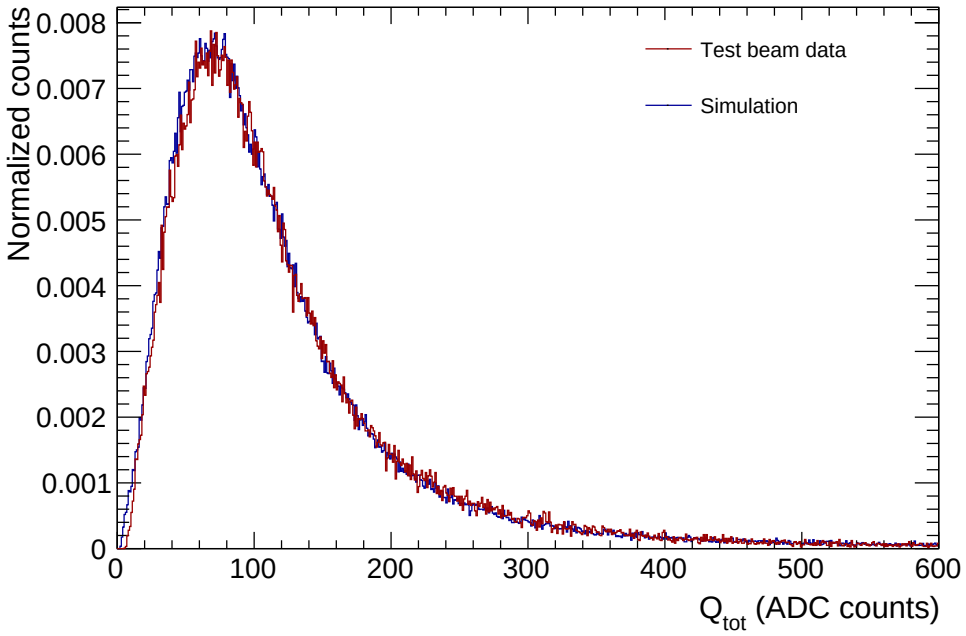

Figure 6.24: Q_{tot} distribution for 2 GeV c^{-1}. Red: data, blue: simulation

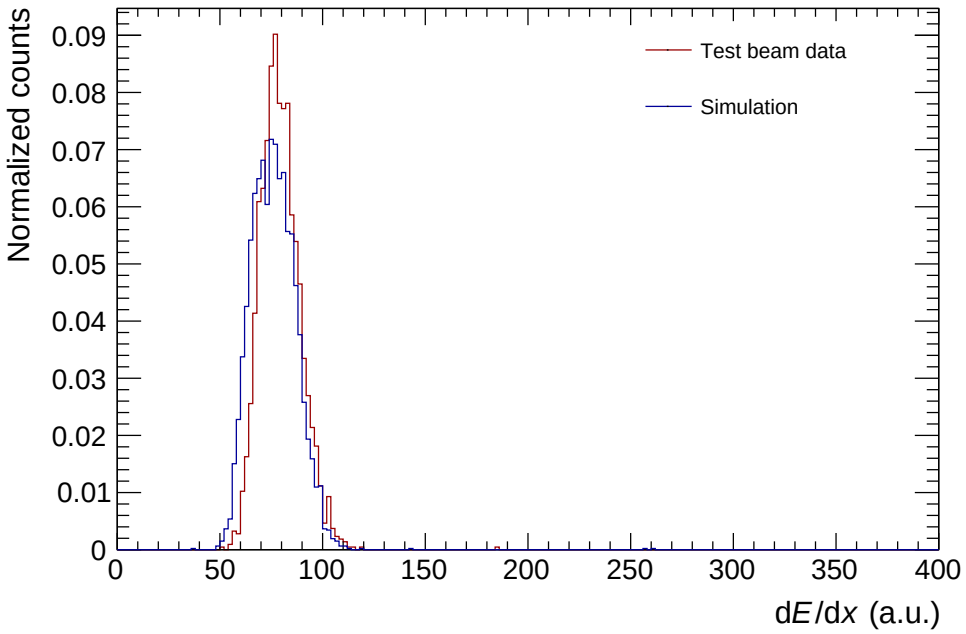

Figure 6.25: $\mathrm{d}E/\mathrm{d}x_{Q_{\mathrm{tot}}}$ distribution for 2 GeV c^{-1}. Red: data, blue: simulation

7 Summary and Conclusion

The LHC will increase its interaction rate to 50 kHz after the second long shutdown in 2019 - 2020. The readout of the ALICE TPC, the main particle identification and particle tracking device of the experiment, is based on gated MWPCs which limit the number of back drifting ions towards the TPC. Those ions distort the electric field inside the TPC diminishing its performance. The gated operation limit the readout rate to about 3.5 kHz. A pile-up of about 5 events on average in the TPC, resulting of the 100 µs electron drift time, demands for continuous readout. Therefore, the current readout is upgraded to GEM technology. GEMs provide intrinsic ion back flow reduction making them suitable for continuous readout. To maintain the excellent PID and tracking capabilities of the current TPC the ion back flow needs to be smaller than 1 %. To achieve this the readout chambers will be equipped with a stack of four GEMs. The large amount of data recorded during continuous operation also demands for a new computing system and software framework, O^2. O^2 will be used for online pre-processing and data compression and offline post-processing. In addition, it contains the simulation framework where the full detector response can be simulated.

To validate the performance of the new readout system, an Inner Readout Chamber of the pre-production phase of the ALICE TPC Upgrade project is equipped with the new front-end electronics. The front-end cards sample the signal at 5 MHz to reduce the amount of data recorded during continuous readout. At the CERN Proton Synchrotron the readout chamber is irradiated with a secondary beam that consists of pions and electrons.

In the course of this work, which is the first analysis done in O^2, the energy loss $\mathrm{d}E/\mathrm{d}x$ resolution is studied. First, a gain map is extracted to correct for local gain variations. The normalized gain distribution of less than 10 % across all readout channels fulfills the requirements for uniformity in order to maintain the current performance of the TPC. For a beam momentum of 1 GeV c^{-1} an energy resolution of 11.9 % and 10.7 % is obtained for pions and electrons, respectively. This results in a separation power of $3.65\,\sigma$. Compared to a previous test beam campaign the latest measurements show a decreased performance. This difference can be attributed to the different sampling frequencies, 5 MHz in the recent test and 20 MHz in the previous one.

To study the influence of the sampling frequency on the energy resolution, a toy Monte Carlo simulation is conducted where the transfer function of the front-end cards is folded with the signal induced by incoming electrons and sampled with 5 and 20 MHz. While the resulting charge distributions at 20 MHz properly reflect the energy resolution of the GEM system, the lower sampling frequency leads to a significant loss in information resulting in

a worsened energy resolution. This effect is confirmed in a qualitative study regarding the influence of the drift length in the TPC on the $\mathrm{d}E/\mathrm{d}x$ resolution.

Finally, the test beam data is used to validate the TPC simulation. Three representative observables are compared, namely the $\mathrm{d}E/\mathrm{d}x$ resolution and the maximum and total cluster charge distributions. They give information on the signal creation and data reconstruction processes. The simulation resembles the detector performance already very well, especially the charge distributions. To further improve the simulations a study involving more observables will be conducted. In addition, the full reconstruction chain will be validated. The individual components, such as the GEM response, will be fine-tuned based on the results of this work.

After the test beam campaign in 2014 this work is the second verification of the final readout system featuring readout chambers with quadruple GEM stacks. At the moment the TPC is on the surface and the readout chambers are being replaced. When the upgrade is finished, first tests with cosmics will be conducted, which give more input for the tuning of the simulation.

Bibliography

[1] L. Evans and P. Bryant, "LHC Machine," *Journal of Instrumentation* **3** no. 08, (Aug, 2008) S08001–S08001. https://doi.org/10.1088%2F1748-0221%2F3%2F08%2Fs08001.

[2] "The Large Hadron Collider." https://home.cern/science/accelerators/large-hadron-collider.

[3] **ATLAS** Collaboration, G. Aad *et al.*, "Observation of a new particle in the search for the Standard Model Higgs boson with the ATLAS detector at the LHC," *Phys. Lett.* **B716** (2012) 1–29, arXiv:1207.7214 [hep-ex].

[4] **CMS** Collaboration, S. Chatrchyan *et al.*, "Observation of a new boson at a mass of 125 GeV with the CMS experiment at the LHC," *Phys. Lett.* **B716** (2012) 30–61, arXiv:1207.7235 [hep-ex].

[5] P. Bechtle, T. Plehn, and C. Sander, "Supersymmetry," in *The Large Hadron Collider: Harvest of Run 1*, T. Schörner-Sadenius, ed., pp. 421–462. 2015. arXiv:1506.03091 [hep-ex].

[6] R. Pasechnik and M. Šumbera, "Phenomenological Review on Quark–Gluon Plasma: Concepts vs. Observations," *Universe* **3** no. 1, (2017) 7, arXiv:1611.01533 [hep-ph].

[7] G. Apollinari *et al. CERN Yellow Reports: Monographs, Vol. 4/2017, CERN-2017-007-M (CERN, Geneva, 2017)* .

[8] **ALICE** Collaboration, K. Aamodt *et al.*, "The ALICE experiment at the CERN LHC," *Journal of Instrumentation* **3** no. 08, (Aug, 2008) S08002–S08002. https://doi.org/10.1088%2F1748-0221%2F3%2F08%2Fs08002.

[9] J. C. Collins and M. J. Perry, "Superdense Matter: Neutrons or Asymptotically Free Quarks?," *Phys. Rev. Lett.* **34** (May, 1975) 1353–1356. https://link.aps.org/doi/10.1103/PhysRevLett.34.1353.

[10] N. Cabibbo and G. Parisi, "Exponential Hadronic Spectrum and Quark Liberation," *Phys. Lett.* **59B** (1975) 67–69.

[11] S. Bethke, "Experimental tests of asymptotic freedom," *Prog. Part. Nucl. Phys.* **58** (2007) 351–386, arXiv:hep-ex/0606035 [hep-ex].

[12] B. Adeva *et al.*, "The construction of the L3 experiment," *Nuclear Instruments and Methods in Physics Research Section A: Accelerators, Spectrometers, Detectors and Associated Equipment* **289** no. 1, (1990) 35 – 102. http://www.sciencedirect.com/science/article/pii/016890029090250A.

[13] C. Lippmann, "Particle identification," *Nuclear Instruments and Methods in Physics Research Section A: Accelerators, Spectrometers, Detectors and Associated Equipment* **666** (2012) 148 – 172. http://www.sciencedirect.com/science/article/pii/S0168900211005419. Advanced Instrumentation.

[14] "ALICE figure repository." http://alice-figure.web.cern.ch/.

[15] **ALICE** Collaboration, B. Abelev *et al.*, "Upgrade of the ALICE Experiment: Letter Of Intent," *J. Phys.* **G41** (2014) 087001.

[16] G. Charpak *et al.*, "The use of multiwire proportional counters to select and localize charged particles," *Nuclear Instruments and Methods* **62** no. 3, (1968) 262 – 268. http://www.sciencedirect.com/science/article/pii/0029554X68903716.

[17] **ALICE** Collaboration, S. Acharya *et al.*, "Real-time data processing in the ALICE High Level Trigger at the LHC," arXiv:1812.08036 [physics.ins-det].

[18] **ALICE** Collaboration, P. Buncic, M. Krzewicki, and P. Vande Vyvre, "Technical Design Report for the Upgrade of the Online-Offline Computing System," Tech. Rep. CERN-LHCC-2015-006. ALICE-TDR-019, Apr, 2015. https://cds.cern.ch/record/2011297.

[19] "ALICE O^2 Project." http://alice-o2.web.cern.ch.

[20] M. Krzewicki *et al.*, "The ALICE high level trigger: status and plans," *Journal of Physics: Conference Series* **664** no. 8, (Dec, 2015) 082023. https://doi.org/10.1088%2F1742-6596%2F664%2F8%2F082023.

[21] "AliRoot Documentation." http://alice-offline.web.cern.ch/AliRoot/Manual.html.

[22] D. Nygren *PEP Internal Report* (1975) 198.

[23] M. Berger, *Development, Commissioning and Spatial Resolution Studies of a new GEM based TPC*. PhD thesis, Technische Universität München, 26 nov., 2015.

[24] **Particle Data Group** Collaboration, M. Tanabashi *et al.*, "Review of particle physics," *Phys. Rev. D* **98** (Aug, 2018) 030001. https://link.aps.org/doi/10.1103/PhysRevD.98.030001.

[25] W. R. L. Rolandi and W. Blum, *Particle Detection with Drift Chambers*. Springer Berlin Heidelberg, 2 ed., 2008.

[26] H. Bethe, "Zur theorie des durchgangs schneller korpuskularstrahlen durch materie," *Annalen der Physik* **397** no. 3, (1930) 325–400. https://onlinelibrary.wiley.com/doi/abs/10.1002/andp.19303970303.

[27] E. Fermi, "The ionization loss of energy in gases and in condensed materials," *Phys. Rev.* **57** (Mar, 1940) 485–493. https://link.aps.org/doi/10.1103/PhysRev.57.485.

[28] H. Bichsel, "A method to improve tracking and particle identification in TPCs and silicon detectors," *Nucl. Instrum. Meth.* **A562** (2006) 154–197.

[29] S. Biagi, "Monte carlo simulation of electron drift and diffusion in counting gases under the influence of electric and magnetic fields," *Nuclear Instruments and Methods in Physics Research Section A: Accelerators, Spectrometers, Detectors and Associated Equipment* **421** no. 1, (1999) 234 – 240. http://www.sciencedirect.com/science/article/pii/S0168900298012339.

[30] C. Garabatos. Priv. Communication.

[31] A. Mathis. Priv. Communication.

[32] J. Alme *et al.*, "The ALICE TPC, a large 3-dimensional tracking device with fast readout for ultra-high multiplicity events," *Nuclear Instruments and Methods in Physics Research Section A: Accelerators, Spectrometers, Detectors and Associated Equipment* **622** no. 1, (2010) 316 – 367. http://www.sciencedirect.com/science/article/pii/S0168900210008910.

[33] **ALICE** Collaboration, "Upgrade of the ALICE Time Projection Chamber," Tech. Rep. CERN-LHCC-2013-020. ALICE-TDR-016, Oct, 2013. https://cds.cern.ch/record/1622286.

[34] E. Hellbär. Priv. Communication.

[35] **ALICE** Collaboration, "Addendum to the Technical Design Report for the Upgrade of the ALICE Time Projection Chamber," Tech. Rep. CERN-LHCC-2015-002. ALICE-TDR-016-ADD-1, Feb, 2015. https://cds.cern.ch/record/1984329.

[36] F. Sauli, "GEM: A new concept for electron amplification in gas detectors," *Nuclear Instruments and Methods in Physics Research Section A: Accelerators, Spectrometers, Detectors and Associated Equipment* **386** no. 2, (1997) 531 – 534. http://www.sciencedirect.com/science/article/pii/S0168900296011722.

[37] F. Sauli and A. Sharma, "MICROPATTERN GASEOUS DETECTORS," *Annual Review of Nuclear and Particle Science* **49** no. 1, (1999) 341–388.

[38] C. Altunbas *et al.*, "Construction, test and commissioning of the triple-GEM tracking detector for COMPASS," *Nuclear Instruments and Methods in Physics Research Section A: Accelerators, Spectrometers, Detectors and Associated Equipment* **490** no. 1, (2002) 177 – 203. http://www.sciencedirect.com/science/article/pii/S0168900202009105.

[39] Z. Fraenkel *et al.*, "A hadron blind detector for the PHENIX experiment at RHIC," *Nuclear Instruments and Methods in Physics Research Section A: Accelerators, Spectrometers, Detectors and Associated Equipment* **546** no. 3, (2005) 466 – 480. http://www.sciencedirect.com/science/article/pii/S016890020500848X.

[40] G. Bencivenni *et al.*, "A triple GEM detector with pad readout for high rate charged particle triggering," *Nuclear Instruments and Methods in Physics Research Section A: Accelerators, Spectrometers, Detectors and Associated Equipment* **488** no. 3, (2002) 493 – 502. http://www.sciencedirect.com/science/article/pii/S0168900202005156.

[41] M. Bagliesi *et al.*, "The TOTEM T2 telescope based on triple-GEM chambers," *Nuclear Instruments and Methods in Physics Research Section A: Accelerators, Spectrometers, Detectors and Associated Equipment* **617** no. 1, (2010) 134 – 137. http://www.sciencedirect.com/science/article/pii/S0168900209013850. 11th Pisa Meeting on Advanced Detectors.

[42] D. Abbaneo *et al.*, "The status of the GEM project for CMS high-η muon system," *Nuclear Instruments and Methods in Physics Research Section A: Accelerators, Spectrometers, Detectors and Associated Equipment* **732** (2013) 203 – 207. http://www.sciencedirect.com/science/article/pii/S0168900213011418. Vienna Conference on Instrumentation 2013.

[43] A. László, G. Hamar, G. Kiss, and D. Varga, "Single electron multiplication distribution in GEM avalanches," *Journal of Instrumentation* **11** no. 10, (Oct, 2016) P10017–P10017. https://doi.org/10.1088%2F1748-0221%2F11%2F10%2Fp10017.

[44] F. Böhmer *et al.*, ""Simulation of space-charge effects in an ungated GEM-based TPC," *Nuclear Instruments and Methods in Physics Research Section A: Accelerators, Spectrometers, Detectors and Associated Equipment* **719** (2013) 101 – 108. http://www.sciencedirect.com/science/article/pii/S0168900213004166.

[45] P. Gasik, A. Mathis, L. Fabbietti, and J. Margutti, "Charge density as a driving factor of discharge formation in GEM-based detectors," *Nuclear Instruments and Methods in Physics Research Section A: Accelerators, Spectrometers, Detectors and Associated Equipment* **870** (2017) 116 – 122. http://www.sciencedirect.com/science/article/pii/S0168900217307878.

[46] **ALICE** Collaboration, A. Mathis, "From gated to continuous readout: the GEM upgrade of the ALICE TPC," in *Proceedings of the 5th International Conference on Micro-Pattern Gas Detectors*. Sissa Medialab, May, 2017.

[47] P. Gasik. Priv. Communication.

[48] **ALICE TPC** Collaboration, M. M. Aggarwal *et al.*, "Particle identification studies with a full-size 4-GEM prototype for the ALICE TPC upgrade," *Nucl. Instrum. Meth.* **A903** (2018) 215–223, arXiv:1805.03234 [physics.ins-det].

[49] **ALICE TPC** Collaboration, P. Gasik, "Discharge probability studies with multi-GEM detectors for the ALICE TPC Upgrade," *Submitted to: PoS* (2018) , arXiv:1807.02979 [physics.ins-det].

[50] M. Villa *et al.*, "Progress on large area GEMs," *Nuclear Instruments and Methods in Physics Research Section A: Accelerators, Spectrometers, Detectors and Associated Equipment* **628** no. 1, (2011) 182 – 186. http://www.sciencedirect.com/science/article/pii/S0168900210015020. VCI 2010.

[51] D. J. Simon, L. Durieu, K. Bätzner, D. Dumollard, F. Cataneo, and M. Ferro-Luzzi, "Secondary beams for tests in the PS East experimental area," Tech. Rep. PS-PA-EP-Note-88-26, CERN, Geneva, Aug, 1988. http://cds.cern.ch/record/1665434.

[52] J. Adolfsson *et al.*, "SAMPA chip: the new 32 channels ASIC for the ALICE TPC and MCH upgrades," *Journal of Instrumentation* **12** no. 04, (Apr, 2017) C04008–C04008. https://doi.org/10.1088%2F1748-0221%2F12%2F04%2Fc04008.

[53] J. Mitra, S. A. Khan, S. Mukherjee, and R. Paul, "Common Readout Unit (CRU) - A new readout architecture for the ALICE experiment," *JINST* **11** no. 03, (2016) C03021.

[54] H. Schulte. Priv. Communication.

[55] **ALICE HLT** Collaboration, D. Rohr, S. Gorbunov, A. Szostak, M. Kretz, T. Kollegger, T. Breitner, and T. Alt, "ALICE HLT TPC tracking of Pb-Pb Events on GPUs," *J. Phys. Conf. Ser.* **396** (2012) 012044, arXiv:1712.09407 [physics.ins-det].

[56] T. Sjostrand, S. Mrenna, and P. Z. Skands, "A Brief Introduction to PYTHIA 8.1" *Comput. Phys. Commun.* **178** (2008) 852–867, arXiv:0710.3820 [hep-ph].

[57] T. Sjostrand, S. Mrenna, and P. Z. Skands, "PYTHIA 6.4 Physics and Manual," *JHEP* **05** (2006) 026, arXiv:hep-ph/0603175 [hep-ph].

[58] S. Porteboeuf, T. Pierog, and K. Werner, "Producing Hard Processes Regarding the Complete Event: The EPOS Event Generator," in *Proceedings, 45th Rencontres de Moriond on QCD and High Energy Interactions: La Thuile, Italy, March 13-20, 2010*, pp. 135–140, Gioi Publishers. Gioi Publishers, 2010. arXiv:1006.2967 [hep-ph].

[59] M. Gyulassy and X.-N. Wang, "HIJING 1.0: A Monte Carlo program for parton and particle production in high-energy hadronic and nuclear collisions," *Comput. Phys. Commun.* **83** (1994) 307, arXiv:nucl-th/9502021 [nucl-th].

[60] R. Brun, F. Bruyant, M. Maire, A. C. McPherson, and P. Zanarini, "GEANT3,".

[61] S. Agostinelli *et al.*, "Geant4—a simulation toolkit," *Nuclear Instruments and Methods in Physics Research Section A: Accelerators, Spectrometers, Detectors and Associated Equipment* **506** no. 3, (2003) 250 – 303. http://www.sciencedirect.com/science/article/pii/S0168900203013688.

[62] **ALICE Collaboration** Collaboration, Dellacasa *et al.*, *ALICE time projection chamber: Technical Design Report*. Technical Design Report ALICE. CERN, Geneva, 2000. https://cds.cern.ch/record/451098.

[63] A. Mathis, "Performance studies with a full-size GEM-based prototype for the ALICE TPC." https://www.das.ktas.ph.tum.de/DasDocs/Public/Master_Theses/Thesis_Mathis.pdf, 2016.

Danksagung

Zuerst möchte ich meiner Themenstellerin Prof. Laura Fabbietti für die Gelegenheit danken, diese Arbeit zu schreiben. Zudem vielen Dank für die Unterstützung auf dem langen Weg bis zur Abgabe.

Als nächstes geht mein besonderer Dank an meinen Betreuer Andi Mathis. Du warst mir stets mit Rat und Tat bei all meinen Fragen und Anliegen behilflich und ich habe sehr viel gelernt.

Of course I also want to thank our former office mate Dr. Piotr Gasik. Your expertise in gaseous detectors is exceptional and I hope your new colleagues appreciate you as much as we do.

Ein weiterer Dank geht an Bernie und Lukas, die Bürokollegen, mit denen sich der Büroalltag ein wenig lustiger gestaltet, sowie an den ganzen Rest der Gruppe, die stets dabei helfen, die Motivation oben zu halten. Jeden einzelnen aufzuzählen wäre hier ein bisschen zu lang...

... deshalb vielen Dank auch an alle nicht E62 Mitglieder, die ihren teils nicht unerheblichen Teil zum Gelingen der Arbeit beigetragen haben.

Zu guter Letzt möchte ich mich bei meiner Freundin Maria bedanken, die mir vor allem in der Zeit vor der Abgabe den Rücken frei- und mich ausgehalten hat.